Title
Radio Frequency Enhanced Plasma Potential and Flows in the Scrape-Off Layer of an Active Antenna

Author
Martin, Michael John

Publication Date
2017

Peer reviewed|Thesis/dissertation

UNIVERSITY OF CALIFORNIA

Los Angeles

Radio Frequency Enhanced Plasma Potential and Flows in the Scrap-Off Layer of an Active Antenna

A dissertation submitted in partial satisfaction of the requirements for the degree Doctor of Philosophy in Physics

by

Michael John Martin

2017

ABSTRACT OF THE DISSERTATION

Radio Frequency Enhanced Plasma Potential and Flows in the

Scrape-Off Layer of an Active Antenna

by

Michael John Martin

Doctor of Philosophy in Physics

University of California, Los Angeles, 2017

Professor Walter N. Gekelman, Chair

Ion cyclotron resonance heating (ICRH) systems are critical components of current and future tokamak experiments aimed at producing nuclear fusion energy. During ICRH a host of deleterious effects occur, including increased heat flux to plasma facing components and modification of launched wave power. A suspected root cause of these effects is the radio frequency (RF) rectification of the plasma potential. Interest in the antenna scrape-off layer (SOL) region has drawn increasing interest, as it is recognized that mitigating these effects is necessary to achieving fusion power. This dissertation investigates the RF rectification of the plasma potential and the resulting cross-field flows that form due to an active RF antenna. The experiment is performed in the Large Plasma Device (LAPD) utilizing a fast wave antenna and RF amplifier system developed for these studies. The RF system is capable of 150 kW output power for a 1 ms pulse that is repeated at the 1 Hz repetition rate of the LAPD plasma discharge.

Upon application of the RF pulse to the antenna, the DC plasma potential, measured with an emissive probe, dramatically increases in certain spatial locations by a factor greater than 10

T_e. The largest plasma potentials are observed at locations magnetically connected to the top and bottom of the antenna, and they exist only in the private SOL created between the antenna and a limiter placed 3.6 m away along the LAPD axis. The DC rectified potentials scale linearly with the antenna current over a factor of 12x in the applied current. These DC potentials increase plasma materials interactions (PMI), resulting in the sputtering of antenna materials whose presence is detected in the bulk plasma by the coatings that develop on probe diagnostics. The DC rectified potentials persist in the plasma long after the RF current in the antenna has rung down on the same time scales as the change in the density.

At the top and bottom of the antenna are circular flows, often called convective cells. These $\boldsymbol{E}\times\boldsymbol{B_0}$ flows arise due to the spatial variation of the RF rectified potentials across the background magnetic field. The maximum strength of the electric field causing these flows was found to scale quadratically with antenna current, giving rise to drift velocities that are a substantial fraction of the local sound speed, $\frac{v_{drift}}{c_s} \approx 0.8$. These flows have a dramatic effect on the density, which increases in the SOL and develops poloidal asymmetries in the plasma region magnetically connected to the front face of the antenna. The convective cells cause a density depletion at the antenna midplane that increases with antenna current until a threshold current. The 2-D density modification is physically consistent with the calculated $\boldsymbol{E}\times\boldsymbol{B_0}$ flows.

These results show a plethora of problems that must be solved for successful ICRH operation, even at low antenna powers. These deleterious effects may be mitigated by antenna designs that reduce rectified potentials and utilize PMI-resilient materials. The saturation in the density depletion at the antenna midplane suggests methods for targeted density injection may be successful in improving antenna wave coupling.

The dissertation of Michael John Martin is approved.

Richard Wirz

George Morales

Troy Carter

Walter N. Gekelman, Committee Chair

University of California, Los Angeles

2017

To June Hu

TABLE OF CONTENTS

List of Figures

List of Tables

List of Symbols

Quantity	Meaning
A	Area
α	Angle between $\boldsymbol{B_0}$ and PFC tangent
b	Area calibration factor for Mach Probe analysis
$\boldsymbol{B}$	Time-varying magnetic field
$\boldsymbol{B_0}$	Background Magnetic Field
$\boldsymbol{c_s}$	Ion Sound Speed
d	Characteristic Probe Dimension
$\boldsymbol{d\hat{A}}$	Differential area normal vector
ΔV	Potential difference between plasma and PFC
e	Fundamental Unit of charge, $e = -q_e$
$\boldsymbol{E}$	Electric field vector
$\boldsymbol{E}_{\parallel}$	Electric Field Component Parallel to $\boldsymbol{B_0}$
$\boldsymbol{E}_{\perp}$	Electric Field component perpendicular to $\boldsymbol{B_0}$
$\boldsymbol{E_x}$	Electric field in the $\hat{x}$ direction
ϵ_0	Vacuum electric permittivity
$\boldsymbol{\epsilon_1}, \boldsymbol{\epsilon_2}, \boldsymbol{\epsilon_3}$	Stix parameters
$\boldsymbol{\epsilon}$	Magnetized plasma dielectric tensor
f_{ce}, f_{ci}	Electron and ion cyclotron frequency
f_{LH}	Lower Hybrid Frequency
f_{pe}, f_{pi}	Electron and Ion plasma frequency
f_{RF}	Launched RF frequency
$\boldsymbol{F_{pond,no\ B_0}}$	Ponderomotive force when no background magnetic field is present
I	Current
$I_{antenna}$	Current in the antenna
I_{emit}	Emitted Current from a probe tip
I_{esat}, I_{isat}	Electron and Ion saturation currents
I_{PFC}	Current drawn by a PFC
J_{esat}, J_{isat}	Electron and Ion saturation current densities
K	Mach Probe calibration constant
k_B	Boltzman's Constant
$\boldsymbol{k}_{\perp,\pm}$	Perpendicular wave number
$\boldsymbol{k_x}$	Exponential decay rate
$\boldsymbol{k_z}$	Parallel wave number
L	System size
$l_{E_\perp}$	Perpendicular electric field scale length
$\lambda_{De}, \lambda_{Di}$	Electron and Ion Debye Length
λ_i	Ion mean free path
M	Mach number
m	Cylindrical mode number

m_e, m_i	Electron and Ion Mass
n_e, n_i	Electron and ion density
q_e, q_i	Electron and ion charge
ρ_e, ρ_i	Electron and Ion gyro-radius
ρ_{T_i}	Ion Thermal gyroradius
$\bar{s}$	Time-averaged sheath thickness
s	Sheath thickness
σ	particle species
T_e, T_i	Electron and Ion temperatures
t_{RF}	RF period
t_{sh}	The time it takes an ion to traverse the sheath
V	Voltage, Probe Bias
V_{BaO}, V_{LaB_6}	Potential of the BaO and LaB_6 Limiters, respectively
V_e	Space-charge limited Emissive probe floating potential
V_f	Floating Potential
$V_{f,e}$	The floating potential of an emissive probe that is not space-charge limited in its emission
V_0	Sheath potential drop
$\overline{V_0}$	Time-averaged sheath potential drop
V_p	Plasma potential
V_{PFC}	Bias voltage of the PFC
$V_{p,DC}$	DC component of the plasma potential
$V_{p,RF}$	RF component of the plasma potential
V_{RF}	RF potential oscillations
ν_{ee}	Electron-electron collision frequency
$\boldsymbol{v_{E\times B_0}}$	**E** cross $\boldsymbol{B_0}$ drift velocity
$\boldsymbol{v_{Te}, v_{Ti}}$	Electron and Ion Thermal velocities
ν_{in}	Ion-neutral collision frequency
ω	Angular Frequency
ω_{sh}	Sheath transit time angular frequency
Z	Effective ion charge

[1] Bold quantities are vector quantities.

Frequently Used Acronyms

Quantity	Meaning
Alcator C-Mod	Alto Campo Toro C-Mod, tokamak located at MIT in Cambridge, Massachusetts
ASDEX(-U)	Axially Symmetric Divertor Experiment (Upgrade), Tokamak located at the Max Planck Institute in Garching, Germany
BAPSF	Basic Plasma Science Facility
DIII-D	Doublet III-D, Tokamak located at General Atomics in San Diego
EAST	Experimental Advanced Superconducting Tokamak, located at the Hefei Institutes of Physical Science in Hefei, China
GPI	Gas puff imaging
ICRF	Ion Cyclotron Range of Frequencies
ICRH	Ion Cyclotron Resonance Heating
IED(F)	Ion Energy Distribution (Functions)
ITER	International Thermonuclear Experimental Reactor
JET	Joint European Torus, tokamak located at the Culham Centre for Fusion Energy in Oxfordshire, U.K.
KSTAR	Korea Superconducting Tokamak Advanced Research, located in Daejeon, South Korea
LAPD	LArge Plasma Device
LH	Lower Hybrid
NSTX(-U)	National Spherical Torus Experiment (Upgra de), Spherical tokamak located at Princeton Plasma Physics Lab in Princeton, NJ
PFC	Plasma Facing Component
PIC	Particle in Cell
PS	Power Supply
RF	Radio Frequency
RFA	Retarding Field energy Analyzer
RMS	Root Mean Square
SOL	Scrape-Off Layer
STRB	Science and Technology Research Building
Tokamak	Toroidal'naya Kamera S Magnitnymi Katushkami
Tore Supra	Tore Supraconducteur (French), tokamak located at the CEA in Cadarache, France; the facility has since been named WEST

Glossary of Selected Terms

Current Strap	A current carrying copper conductor within an ICRF antenna. It is the main radiating element of the antenna.
Limiter	A material object designed to be impacted by plasma in order to shape the plasma profile. In this dissertation, the limiters refer to two 12”x12” stainless steel plates inserted into the plasma on either side of the antenna.
Plasma Facing Component (PFC)	Any material object that is directly exposed to plasma and may therefore experience high heat fluxes or be impacted by energetic particles.
Scrape-off layer (SOL)	The scrape-off layer refers to the plasma regions in which background magnetic field lines terminate in materials surfaces. In this thesis, it refers to the plasma region between the antenna and the limiters.

Acknowledgements

I would first like to thank my advisor, Professor Walter Gekelman, for giving me three ML-8618 high power triodes to experiment with. I am sincerely grateful for the time and effort he invested in my education and for his patience throughout the process. I also appreciate the atmosphere he fosters at the lab, in which graduate students can solve problems in their own way and make their own mistakes. For me, this is the most effective way to learn. Finally, I appreciate his willingness to share stories about his bizarre experiences in teaching, traveling, and life.

I would also like to thank Pat Pribyl for all of his guidance during the design and construction of the RF amplifier. His vigilance and experience are undoubtedly why I am still alive despite all of the high voltage engineering involved in my project. In addition, I am grateful for the enthusiasm he expressed when I shared results with him, even when I thought they were mundane.

I am grateful to my committee members, Professors George Morales, Troy Carter, and Richard Wirz for providing helpful comments and suggestions and for actually reading this thesis. In addition, I appreciate the Phys 222 courses taught by Professors George Morales and Troy Carter.

The research scientists at the BAPSF have been very helpful throughout my time there. Many thanks to Bart Van Compernolle for happily discussing IDL issues and physics with me, and of course for introducing me to Paraview, even though he still has not "liked" my YouTube video. Steve Vincena assisted me with computers countless times and was always willing to appreciate or offer a Simpsons reference. Shreekrishna Tripathi's optimism, sense of humor, and general advice helped lift my spirits countless times. Seth Dorfman's donated Matzo crackers and stories of misguided students, which have helped energize me and entertain me throughout the dissertation-writing process.

The technical staff at the STRB is very helpful and patient. They possess the remarkable ability to translate graduate student gibberish into actual hardware development. I am deeply grateful to Zoltan Lucky, Marvin Drandell, and Tai Le for the expert technical assistance they offered throughout my time here. In addition, they always offered it with a smile! I appreciate Zoltan Lucky letting me raid the snack stash and for finding exactly the piece of hardware I wanted in some obscure cabinet in the lab. Thanks to Marvin Drandell for introducing me to

1980s era romantic comedies and for giving me that goose egg, which continues to be one of my all-time favorite gifts I've ever received. And thanks to Tai Le for somehow making exactly what I want on a CNC lathe when I gave him a hastily drawn figure on a napkin.

I have been fortunate to have had several interactions with researchers concerned with ICRF physics in tokamak plasmas. I am especially grateful to Rory Perkins at PPPL for informative discussions and for always being interested in my results, even when my reasoning or analysis was not yet fully formed. I wish him the best of luck leading the ICRF campaign at LAPD.

My fellow graduate students have been a source of inspiration and support throughout my time here. My graduate student experience was greatly enhanced by Chris Cooper, Yuhou Wang, Nathaniel Moore, Jeffrey Bonde, Tim DeHaas, and Giovanni Rossi. I'd like to thank all of them for the joy their presence has given me over the years. Chris Cooper has always been hilarious and encouraging around me. Yuhou Wang for some reason I'll never know has always been unreasonably generous with me. She gave me her microwave and went the extra mile in helping me find post-graduation employment at Lam Research Corporation. I am thrilled to be working alongside her in the future, and I hope we one day find those ice cream moon cakes. Nathaniel Moore, a.k.a. "l'homme à gauche," is unrivalled in his ability to give late-night board game recaps and display Battlestar Galactica enthusiasm. To him I say, "Gaius Baltar?!" Jeffrey Bonde has always shared his broad knowledge of all things plasma and other. And boy does he mix a mean Long Island ice tea. His absence in the autumn of my graduate school is acutely felt. Tim DeHaas brightens up my days be being so curmudgeonly. His various verbal expositions and pontifications have inspired me to think about the deeper meanings of the scientific process. I hope this is the year he takes control of his thyroid. Giovanni Rossi is a beautiful male specimen. I will miss the smiles he always brings to my face.

I'd like to thank AIP Publishing and Elsevier for formally granting me permission to reprint figures included in Chapters 1 and 3.

Finally, I'd like to thank my family and friends who have always been cheerful and supportive. I'd especially like to thank my "roommate," June Hu, for providing me endless hugs, encouragement, and about two-sevenths of our weekly dinners.

Vita

2004-2008	B.A. Physics Cornell University Ithaca, NY
2008-2009	Junior Staff Scientist Innovative Dynamics, Inc. Ithaca, NY
2009-2013	Teaching Assistant Department of Physics University of California, Los Angeles
2009 - 2010	M.S. in physics Department of Physics University of California, Los Angeles
2013-2017	Graduate Student Researcher Department of Physics University of California, Los Angeles

Publications

Martin, M.J., Bonde, J., Pribyl, P., and Gekelman, W. "A Resistively Heated CeB_6 Emissive Probe" *Rev. Sci. Instrum.* **86**, 053507 (2015).

Martin, M.J., Pribyl, P., Gekelman, W., and Lucky, Z. "An RF Amplifier for ICRF Studies in the LAPD" *AIP Conf. Proc.* **1689**, 070010 (2015).

Conference Presentations

Martin, M.J., Gekelman, W., Pribyl, P., Van Compernolle, B., Carter, T., Van Eester, D., and Crombé, K. "Experimental Study of Convective Cells and RF Sheaths Excited by a Fast Wave

Antenna in the LAPD" Presented at 58th Annual Meeting of the APS Division of Plasma Physics, San Jose, CA 2016

Martin, M.J., Gekelman, W., Pribyl, P., Van Compernolle, B., and Carter T., "Experimental Study of RF Sheath Formation on a Fast Wave Antenna and Limiter in the LAPD" Presented at 57th Annual Meeting of the APS Division of Plasma Physics, Savannah, GA 2015

Martin, M.J., Gekelman, W., Van Comprenolle, B., and Pribyl, P., "RF Sheaths due to Shear Alfvén Waves in the LAPD" Presented at 21 Topical Conference on Radiofrequency Power in Plasmas, Lake Arrowhead, CA 2015

Martin, M.J., Van Compernolle, B., Gekelman, W., Pribyl, P., Carter, T., D'Ippolito, D.A, and Myra, J.R., "Far-field RF Sheaths due to Shear Alfvén Waves in the LAPD" Presented at 55th Annual Meeting of the APS Division of Plasma Physics, Denver, CO 2013

Chapter 1

Introduction

1.1 Thesis Motivation

Nuclear fusion power tantalizes mankind with, effectively, an unlimited supply of energy with relatively harmless nuclear byproducts. In order to create conditions conducive to nuclear fusion reactions, the fusion reaction cross section must be substantial. For D-T fusion, the lowest hanging fruit of all known fusion reactions, this occurs for $T_i > 10$ keV [1]. Ion-cyclotron resonance heating (ICRH) is a demonstrated method for heating magnetically confined plasma ion species to such conditions [2], and will be relied upon in ITER, whose first plasma is currently scheduled for December 2025, to couple up to 40 MW of power to the plasma, 20 MW from each of two antennas [3].

ICRH has been demonstrated on early stage tokamaks, and is used on most major tokamak experiments today, including JET, Asdex-U, Alcator C-Mod, Tore Supra/WEST [2], EAST [4], and KSTAR [5] with radio-frequency generators in the 1 - 10 MW range. Though ICRH successfully heats the ions, it also has its drawbacks. Increases in the impurity content, often consisting of the plasma facing component (PFC) material, are observed during ICRH in many tokamaks [6, 7]. This is troublesome for nuclear fusion energy production, as a low fractional content of high-Z impurities [10^{-5} for W, 10^{-4} for Mo, 10^{-1} for C] may radiatively cool the plasma, limiting its fusion performance [8].

The suspected cause of the increased impurity content is related to the RF rectification of DC plasma potential, often termed RF sheaths [9]. RF sheath potentials of several hundred volts are believed to accelerate plasma ions into PFCs, causing materials sputtering. RF sheaths in tokamaks are broadly distinguished in two categories, the so-called near-field and far-field sheaths. Though these terms are ubiquitous in ICRH literature, the literature is inconsistent on the distinction between the two categories. For the purpose of this thesis, near-field sheaths will refer to the sheaths that form on PFCs that are connected along background magnetic field lines, $\mathbf{B_0}$, to the antenna, including the antenna itself. Whereas far-field sheaths refer to sheaths that form on other PFCs in the vessel.

The exact cause of the RF sheaths that form during ICRH is debated. One expected cause of RF sheaths is the presence of an oscillating RF potential between the plasma and PFCs that drives the RF sheath [10, 11]. Another explanation is that RF sheaths are caused by parasitic launch of a slow wave or mode conversion of a fast wave to a slow wave [12 - 14]. The reasoning behind this theory is that slow waves have an electric field parallel to the background magnetic field, $\mathbf{E}_{||}$, which causes the formation of the RF sheath [15]. Wave-induced RF sheath theories are currently limited by using a plane wave approximation, which doesn't fully account for realistic wave structures. A third candidate for driving the RF sheaths is the direct excitation of $\mathbf{E}_{||}$ in the antenna launch structure. The distinction between $\mathbf{E}_{||}$ from the antenna structure and from the slow wave is only occasionally mentioned in the literature, with most authors implicating the slow wave. At first these suspected causes of driving RF sheaths appear to be the same thing, namely an $\mathbf{E}_{||}$ to

$\mathbf{B_0}$ at PFCs. However, the nature of the electric field can be either electrostatic (antenna) or inductive (wave). The distinction is also important because methods of controlling or minimizing, for example, slow wave $\mathbf{E}_{||}$ vs. antenna launcher $\mathbf{E}_{||}$ may be different.

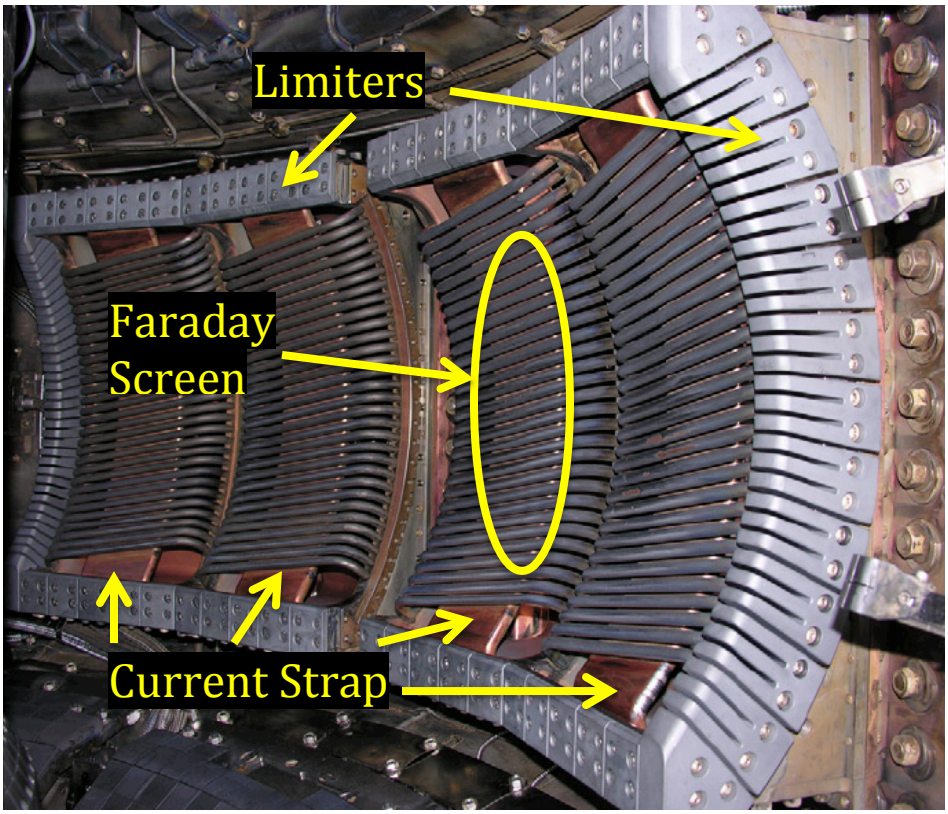

Figure 1.1: Antenna installed in Alcator C-Mod tokamak. The limiter, current strap, and Faraday screen components are labeled. Arrows indicating current straps are pointing at the bottom of them. The Faraday screen consists of numerous conducting rods positioned in front of the current straps. Reprinted with permission from ref. [7].

ICRH antennas across most tokamaks contain similar design elements. One of the ICRH antennas in the Alcator C-mod tokamak is picutured in figure 1.1. The current straps in the antenna are the RF current carrying conductor designed to be the radiating element for the desired wave. Antennas often contain both poloidal and radial limiters to prevent plasma seeping into the antenna enclosure. Limiters in general are structures in tokamaks that background magnetic field lines intersect. Most antennas also contain Faraday screens in order to prevent the launching of undesirable wave polarizations. These elements are shown and labeled in figure 1.1.

Diagnosis of RF sheaths in tokamaks, regardless of their cause, is difficult because tokamak plasmas are harsh environments that are not amenable to direct diagnostic probing. However, a number of tokamaks have been successful in directly or indirectly measuring behavior consistent with RF sheaths in a limited fashion. In Alcator C-mod, emissive probes and gas puff imaging (GPI) were used to measure one-dimensional profiles of plasma potential [7]. Emissive probes make this measurement directly, whereas when using GPI, the assumption that poloidal velocities are caused only by $\mathbf{E}_{\mathbf{radial}}\mathrm{x}\mathbf{B}_{\mathbf{toroidal}}$ flows is made. $\mathbf{E}_{\mathbf{radial}}$ can be integrated to give the plasma potential (this of course requires a known or assumed boundary condition). In Alcator C-mod, measurements of RF-rectified potentials in both the near-field [7] and far-field [16] have been made, where plasma potentials increase up to 700 V and 100 V, respectively. In the Tore Supra tokamak, reciprocating Langmuir probes have measured the floating potential and ion saturation current in the SOL of an active ICRF antenna, where the floating potential increased 140 V [17]. This measurement was repeated during several tokamak discharges with varying

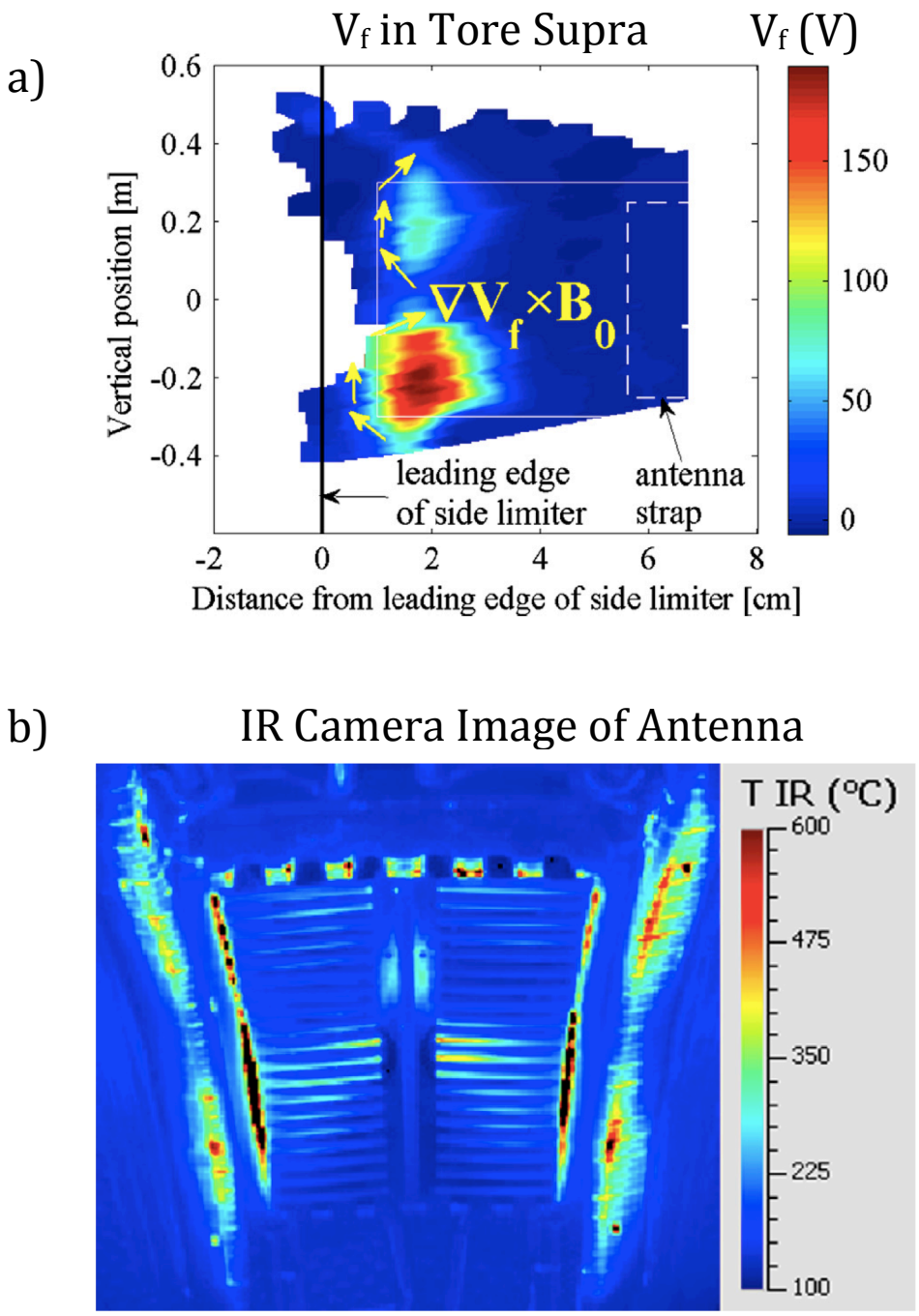

Figure 1.2: Floating potential and IR camera measurements during ICRF experiments in Tore Supra. a) V_f profile in the scrape-off layer during a 1 MW RF discharge. Maximum V_f reaches 170 V. Antenna components are shown for location reference. Flow stream lines are also shown. b) IR camera view of the same antenna. Maximum temperatures occur at the top and bottom of the antenna. Reprinted with permission from ref. [18].

$\mathbf{B_0}$ pitch angle to map out magnetic connections to the entire height of the ICRH antenna in the SOL. The floating potential map obtained from one of these experiments [18] is shown in figure 1.2, and it shows that the most significant enhancements to the floating potential occur when the probe tip is at a location magnetically connected near the top and bottom corners of the antenna structure. In addition, retarding field energy analyzers (RFA) have successfully been deployed in both ASDEX-Upgrade and Tore Supra to obtain average ion impact energies derived from ion energy distributions [19, 20]. These measurements involve many tokamak discharges with a sweep over magnetic pitch angle. Changing magnetic pitch angle adjusts where a magnetic field line through a poloidally stationary probe intersects the antenna structure and thus provides poloidally resolved measurements using poloidally stationary probes. Changing magnetic pitch angle also changes the plasma discharge by adjusting the plasma density and temperature and is not an ideal way to diagnose RF-enhanced potentials. In addition, floating potential and RFAs do not provide direct measurements of the plasma potential, and thus must be interpreted carefully.

The problem of RF sheaths is by no means unique to ICRF experiments in tokamaks. RF sheaths have been visually observed in plasma discharge tubes where active RF electrodes resulted in the, “constriction of the luminous portion of the plasma away from the inner walls of the glass tube” [21]. This phenomenon is pictured in figure 1.3. In addition, RF sheaths are essential to fabrication of microelectronics, especially during the etch portion of the process [22]. During the microelectronics manufacturing process a silicon waver is placed on an RF-biased

substrate. The RF bias is used to control the ion energy distribution function (IED) of plasma ions accelerated in the RF sheath and impacting or reacting with the silicon wafer. Analytical models of the IEDs have limited applicability [23,24], and so often computer models are used to investigate the IEDs [25]. A thorough review is given in ref. [24]. These IEDs have been measured using Laser-Induced Florescence in 1-D [26] and 2-D [27] single-frequency bias cases and in 2-D dual frequency bias cases [28].

Significant differences exist between the RF sheaths that occur in tokamaks and plasma processing chambers. Firstly, for the most part RF sheath forming structures in plasma etch chambers are capacitively coupled, whereas ICRF antennas are inductively coupled. Secondly, plasma processing chambers are often unmagnetized with low ionization fraction, while PFCs in tokamaks can be oriented with arbitrary angle relative to $\mathbf{B_0}$. Even the approach to diagnosing the RF sheaths in the two fields is different. The main concern is the IED in plasma processing, whereas the DC rectified plasma potential is the main concern in tokamak RF sheath research. These two quantities may be very closely related for strongly capacitive sheaths, where $f_{RF} \gg f_{pi}$, with f_{RF} and f_{pi} the RF and ion plasma frequencies, respectively.

Shifting focus back to tokamak plasmas, $\mathbf{B_0}$ field lines in the SOL terminate on plasma boundaries. RF rectification may increase the plasma potential on one magnetic field line differently from the plasma potential on an adjacent field line. In this case, an electrostatic electric field is formed in the SOL across the magnetic field.

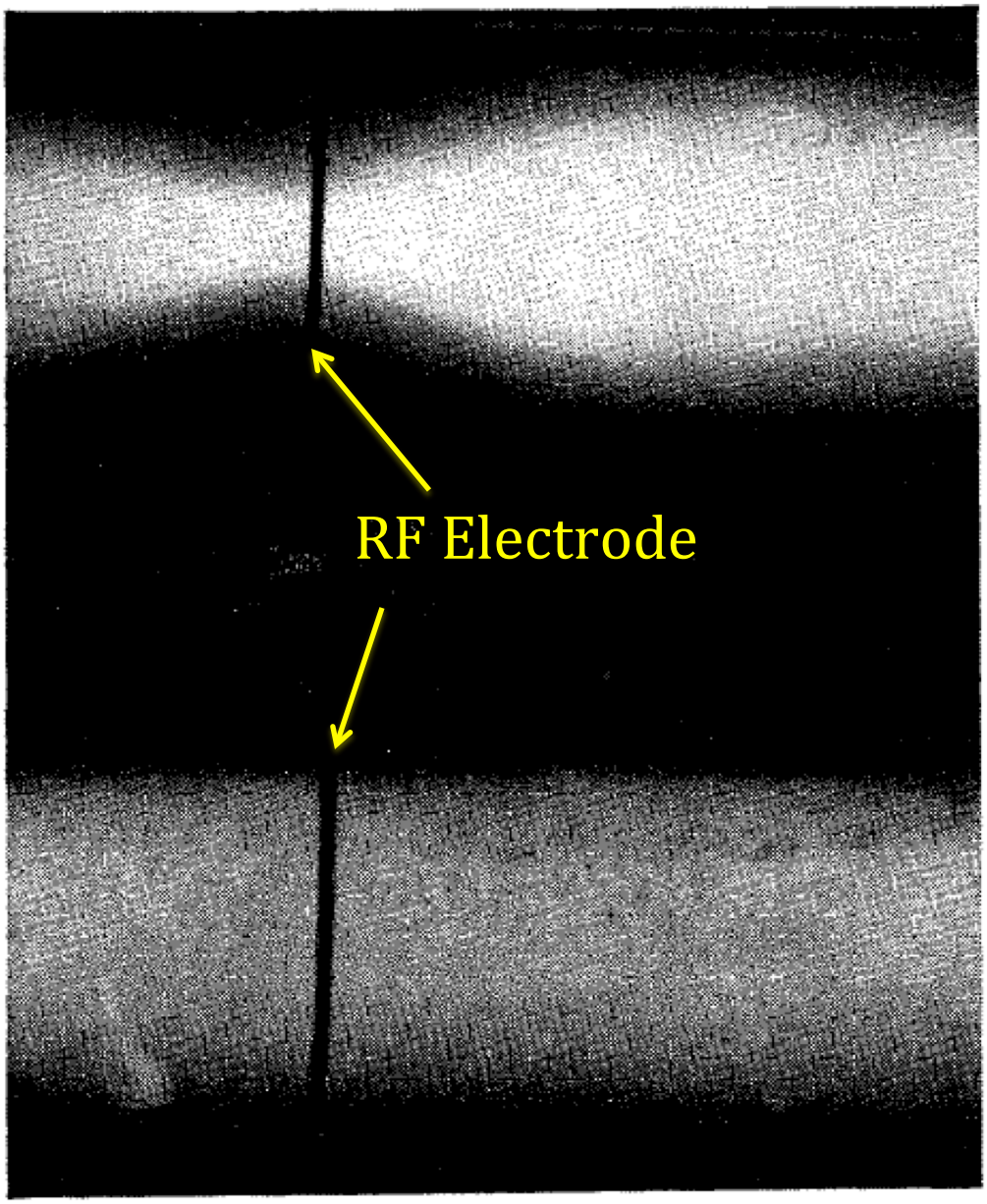

Figure 1.3: Constriction of the luminous portion of the plasma in a glass discharge tube thought to be due to the formation of an RF sheath. The top picture shows the plasma discharge with RF applied to an external electrode. The bottom picture shows the situation when no RF is applied to the electrode. Reprinted with permission from ref. [21].

This leads to $\boldsymbol{E}\times\boldsymbol{B_0}$ particle drifts, and may establish steady state convective cells [29]. The term "convective cells" has been used to describe roughly circular flow patterns that close on themselves and are established by $\boldsymbol{E}\times\boldsymbol{B_0}$ particle drifts. As far as this author is aware, three classes of convective cells are thought to exist. One class of convective cells involves the flows between adjacent Faraday screen elements, and a second class involves the flows along the entire front face of the ICRF antenna structure [29]. The third class of convective cells occurs closer to the outer wall of the tokamak and is produced at the upper and lower extremities of ICRF antennas [17, 30, 31]. It is this third class of convective cells that will be discussed in this thesis.

Direct experimental measurements of convective cells are difficult to obtain. The spatial profile of convective cells observed in ref. [18], seen in figure 1.2, though illuminating, relies on measurement of V_f, rather than V_p, and so is only qualitative at best. RFA measurements [19,20] of average parallel ion energy are also not necessarily indicative of cross-field $\boldsymbol{E}\times\boldsymbol{B_0}$ flows because they require knowledge of the plasma density in order to be rigorously interpreted. Optical measurements are less direct. Reflectometry gives one-dimensional density profiles. Convective cells are invoked to explain the change in reflectometry profiles after an ICRF antenna is activated [19, 32], as is the increased heat flux to ICRF antennas as measured by IR cameras [18].

The principal concern in tokamak operation with the formation of convective cells is the redistribution of the SOL density profile. ICRF coupling theory is sensitive to the density profile in front the antenna in both simulation [33, 34] and

experiment [35], and this profile is usually imposed in the calculation, rather than self-consistently calculated. In general, a decreased density in front of the ICRF antenna will lead to decreased loading resistance and coupled power [eg. 35]. Other deleterious effects may also occur, including the refraction of the launched wave or a mode conversion into an unwanted wave. Additionally, a broadening of the SOL density profile may increase the density in the far SOL, thus increasing the heat flux to thermally sensitive PFCs that may need to be actively cooled [35]. Furthermore, the SOL density modifications are nonlocal with respect to the ICRF antenna and impact the entire SOL where they are observed to alter Lower Hybrid (LH) launcher radiation resistance [17]. In some cases the LH radiation resistance actually increases, rather than decreases!

Ever more sophisticated computation is being performed to study these phenomena in a predictive capacity, with the current trend moving away from one-dimensional [13, 14, 36, 37] models to two- or three-dimensional modeling [38, 39] that take into account realistic antenna geometries. However, there is currently no diagnosable plasma physics experiment to validate the predictions of these computer simulations. A strong desire for more feedback between experimental and computational research in this discipline, especially with more detailed measurements is motivating the construction of dedicated plasma experiments for ICRF studies [40 - 42].

1.2 Thesis Outline

This thesis attempts to characterize the RF-enhanced potentials and resulting $\boldsymbol{E}\times\boldsymbol{B_0}$ flows in the SOL of an active ICRF antenna in the LAPD plasma. As

such, it provides a benchmarking case for comparison to future ICRF simulations. The LAPD is a highly diagnosable plasma experiment, which is ideal for performing detailed benchmarking experiments for simulation validation. Unfortunately, at the start of this thesis the facility was not equipped with a high-power ICRF source necessary for experiments exploring RF-rectification and convective cell phenomena. Fortunately, through the efforts of this thesis, that has changed. **Chapter 2** describes the design, construction, and performance of the RF source that was built for this experiment. Details about the LAPD plasma experiment and diagnostic methods are described in **Chapter 3**. Particular attention is given to the design and performance of the emissive probe used to measure the plasma potential in the LAPD, which uses a unique CeB_6 emitter. **Chapter 3** also describes the experimental setup. **Chapter 4** details the rectified potential measurements with comparisons to various RF-sheath models. RF sheath theory and concepts are introduced in this chapter as they become necessary. The parallel (to $\boldsymbol{B_0}$) physics in that rectified potentials are responsible for ion acceleration into PFCs during ICRH are presented. The perpendicular flows due to the $\boldsymbol{E}\times\boldsymbol{B_0}$ drift are detailed in **Chapter 5**. Finally, concluding statements made about the results and future work to continue this project comprise **Chapter 6.**

Chapter 2

Design of the High Power Fast Wave RF Amplifier

A high power RF amplifier system was designed and built to launch fast waves in the LAPD to study near- and far-field sheath generation. The design goal of the amplifier was to produce an RMS RF power output of 100 kW at operating frequencies in the ion cyclotron range of frequencies (ICRF) for Hydrogen in the LAPD (2 – 6 MHz). A brief schematic of the entire system is shown in figure 2.1 below. Pictures of the main components of the system are shown in figure 2.2. Prior to the construction of this system, the highest power RF driver at the lab that operated in the ICRF had a maximum power output of 5 kW.

The RF amplifier system consists of a high voltage DC charging power supply (PS), a capacitor bank, a pulse modulator, controls and power cables connecting components on the ground floor of the Science and Technology Research Building (STRB) with components in the LAPD basement lab, the RF amplifier, an impedance matching network, and a fast wave antenna. The basic operation is as follows: the DC supply charges the capacitor bank, which is the energy source of the amplifier. The capacitor bank voltage is switched to the RF amplifier through the pulse modulator, with a high voltage coax cable connecting the pulse modulator and amplifier. The amplifier output is impedance matched to the antenna with a matching network, and the antenna is immersed in the LAPD plasma. Brief descriptions of each component are given in the following sections.

.

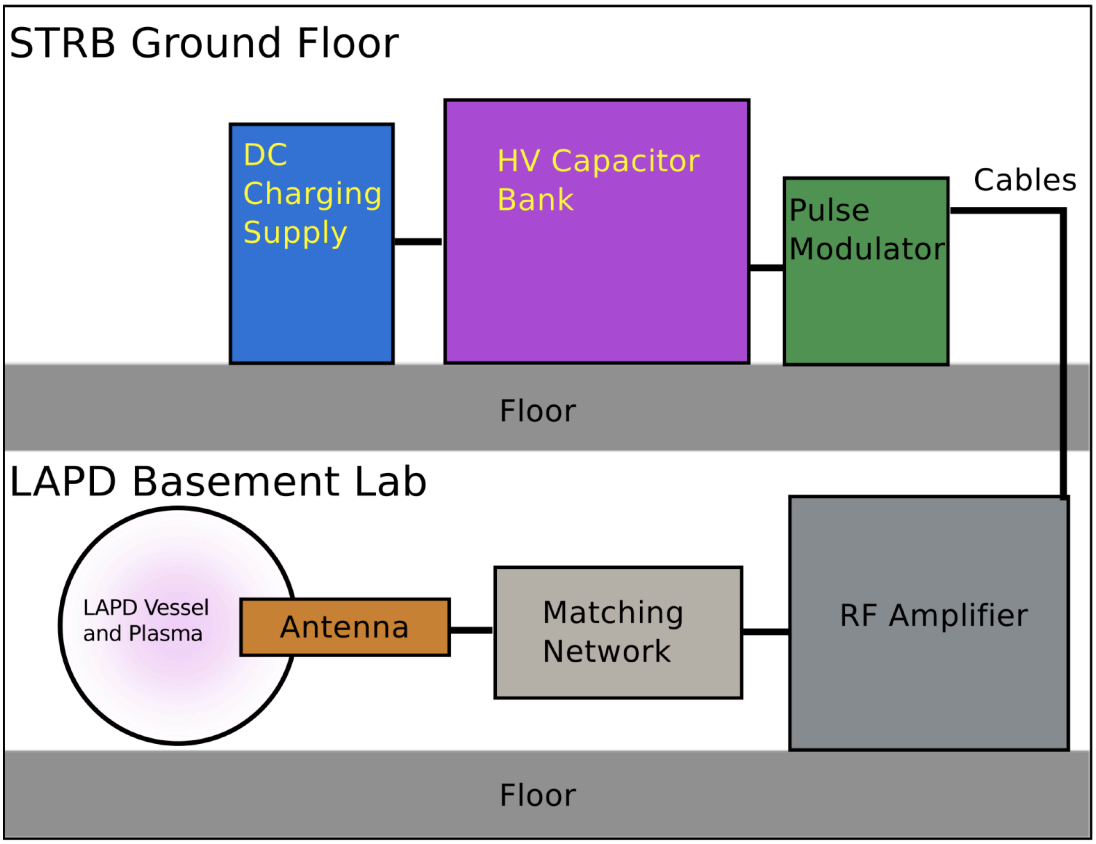

Figure 2.1: An overview of the RF amplifier system layout. The diagram shows the major components and how they are connected.

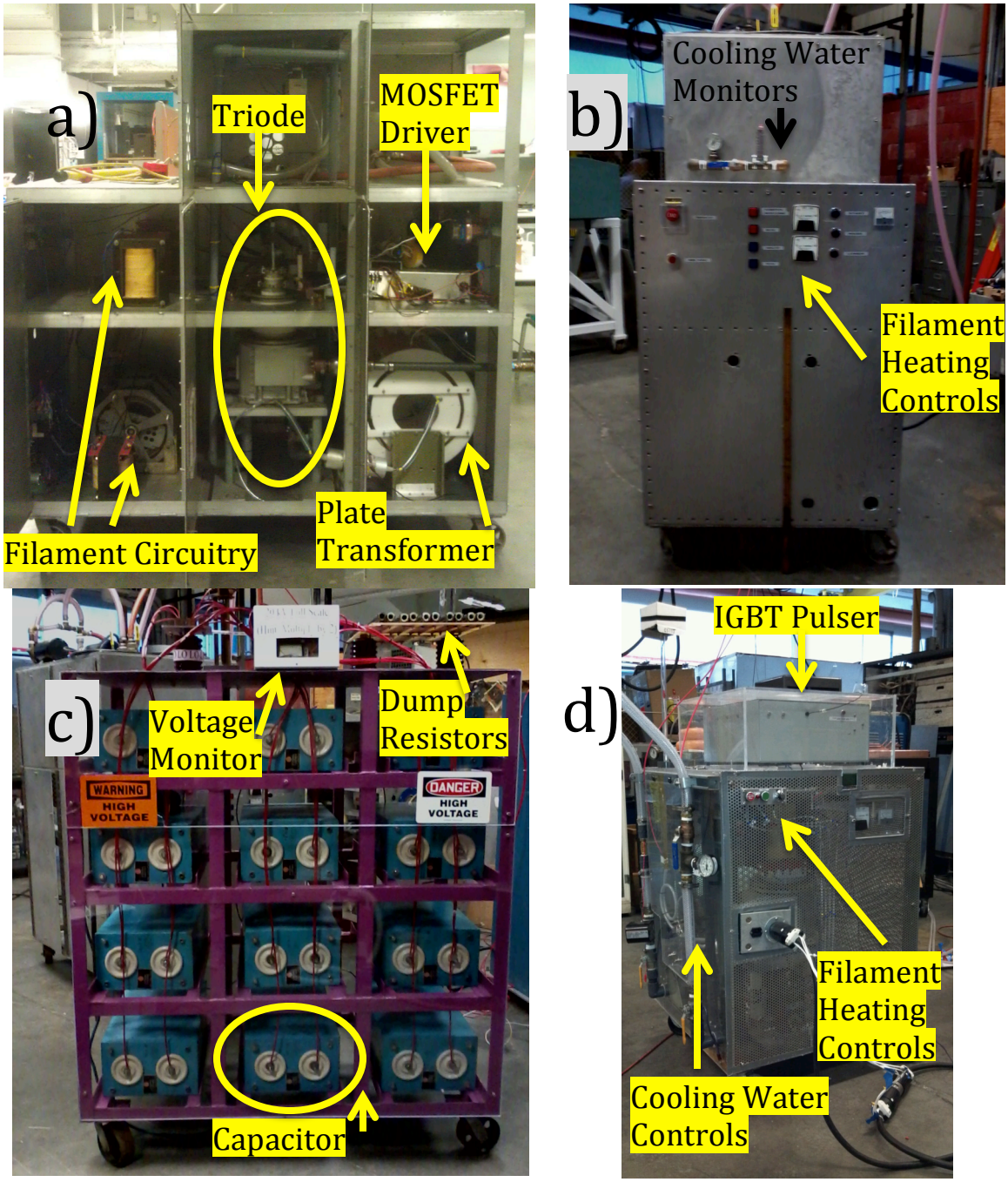

Figure 2.2: Pictures of the RF amplifier system main components. a) The RF amplifier chassis side-profile, b) the RF amplifier filament control and water monitoring panel, c) the HV capacitor bank, and d) the pulse modulator.

2.1 Power Supply and Capacitor Bank

The DC Power Supply (PS) charges the capacitor bank during operation of the RF amplifier. It is capable of providing a DC output power of up to 37.5 kW (1.5 A at 25 kV). The PS charges a 624 μF capacitor bank, which consists of twelve 52 uF capacitors in parallel with each other. When halting operation of the capacitor bank and PS, the capacitor bank is dumped through a 3 kΩ resistor network, with an RC time constant of 1.87 s. Safety relay circuits have been installed on the capacitor bank and PS to insure that the PS does not charge the capacitor bank when the dump switch is closed. 50 MΩ resistors have been installed across each 52 μF capacitor so that in the event of a catastrophic failure of the dump resistors each capacitor will slowly discharge through the bleeder resistor with a time constant of .72 hours. This allows the operator to leave the capacitor bank unattended overnight.

During routine operation of the amplifier the bank voltage is set to approximately 12 kV, with 45 kJ of stored energy in the bank. If the amplifier is operated at full power (200 kW RMS power) for a 10 ms LAPD discharge a bank voltage droop of 4.4% per pulse is expected. The charging supply can recharge the capacitor bank between LAPD discharges. The output voltage of the bank is connected to the plate of the pulse modulator triode, as shown in figure 2.3.

2.2 Pulse Modulator

The basic pulse modulator circuit diagram is shown in figure 2.3. It acts as a high voltage, current limited switch that delivers power from the capacitor bank to the RF amplifier during the active portion of its duty cycle. The pulse modulator outputs

a high voltage square pulse to the plates of the triodes in the RF amplifier and is current limited by thermionic emission of the triode filaments and its grid bias circuitry. It separates the high voltage side of the capacitor bank from the plate circuit in the RF amplifier, which prevents damage to these components in the event of a short to ground in the RF amplifier plate circuitry. The pulse modulator also adds a measure of convenience to operating the RF amplifier. During an experiment the RF amplifier is in the STRB basement, and the capacitor bank and charging supply are on the STRB 1st floor (see figure 2.1).

The pulse modulator consists of a single ML-8618 vacuum tube. The DC high voltage from the capacitor bank is connected to the plate of the tube, and the filament of the tube acts as the output, as in figure 2.3. An IGBT circuit pulses the grid to +240V with respect to the filament to make the triode conduct current, and otherwise holds it at -1.2 kV to largely prevent the tube from conducting. With 12 kV on the capacitor bank a -1.2 kV grid bias is below the recommended cutoff curve for the triode [43]. In practice, the pulse modulator allows some current to flow to the plate circuit during the inactive part of its duty cycle. According to ref. [43], this current is below 20 mA. A 20 mA electric shock is described as a, “painful shock, [with] loss of muscle control [for 50% of the population]” [44, 45]. This is below the threshold for ventricular fibrillation for most people, which occurs around 50 mA. At any rate, proper safety measures should always be taken while working with high voltage, and so the RF amplifier plate circuit is grounded during maintenance.

The pulse modulator output is connected to the plates in the RF amplifier circuit by a length of high voltage coax cable whose outer conductor is grounded at

both ends to provide shielding. The signal for pulsing the grid of the pulse modulator is supplied by a delay generator located in the LAPD lab and carried to the pulse modulator through a fiber optic cable. The pulse modulator includes safety relays that ensure the filaments are not heated unless there is cooling water flowing through the tube jacket of the ML-8618 triode. The water in the tube jacket is connected to both the plate of the triode and the high voltage side of the capacitor bank at all times. The water line is grounded to the pulse modulator chassis in both the supply and return lines, which are separated from the jacket by ~ 2 meters of 1" ID tubing. It is thus important that the water present a high impedance path to ground. This was achieved by using deionized water in a closed, recirculating system. Using non-deionized water in the tube jacket resulted in draining the capacitor bank at a rate the DC charging supply could not keep pace with. The downside of the using deionized water is that it erodes copper over time [46]. Given that the experiment is not being continuously run, the engineering compromise to use deionized water was made.

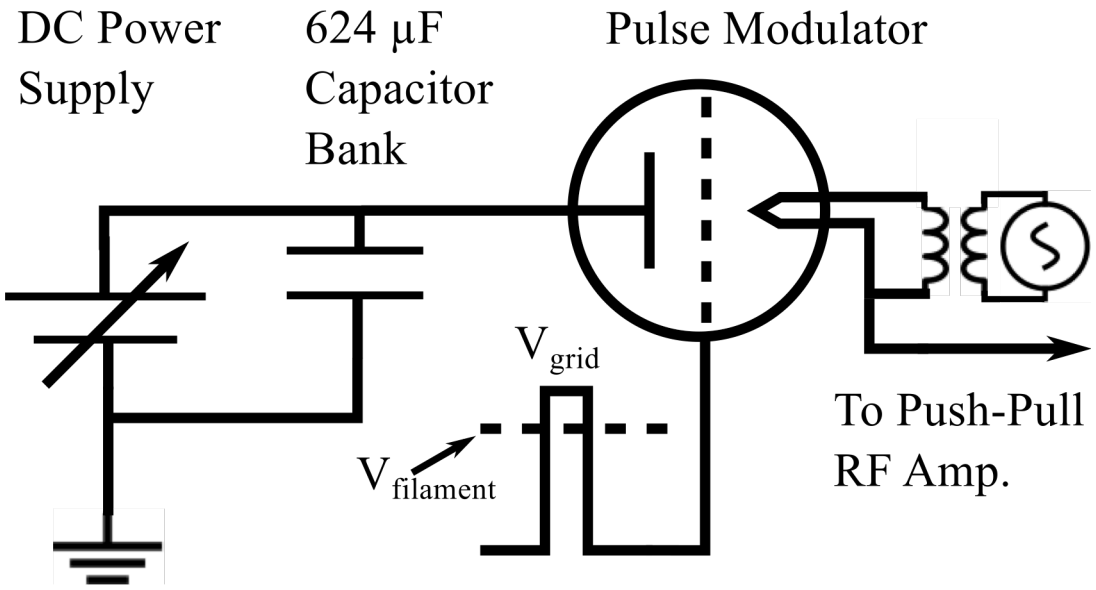

Figure 2.3. Circuit diagram of the DC power supply, the capacitor bank, and the pulse modulator circuit.

2.3 RF Amplifier

A circuit diagram of the RF amplifier is shown in figure 2.4, with values of important components in table 2.1. The amplifier works in a push-pull configuration operated anywhere from class AB to class C, depending on the DC plate voltage. The push-pull RF amplifier employs two ML-8618 vacuum tubes. One end of each tube filament is grounded. The grids of the triodes are driven by a MOSFET H-bridge RF driver that utilizes 32 transistors. Each MOSFET is capable of continuous operation with a drain-source voltage of 600 V and a drain current of 39 A. The RF driver output is transformed by an air core step up transformer. The grids of the tubes are attached to opposite ends of the secondary of the transformer to be driven 180 degrees out of phase. The grid driving circuit is tunable through two vacuum

variable capacitors, C_t, that form a tank circuit with the secondary inductance of the air core transformer. A DC bias is applied to the grids via a 600 V DC power supply.

The pulse modulator output voltage, taken at the filament of the pulse modulator triode, is connected to the plates of the RF amplifier triodes through the center-tapped primary of the output transformer. This point is also bypassed to ground through a 50 nF capacitor, $C_{p,b}$, to minimize RF voltages at the filament of the pulse modulator. The plates of the two vacuum tubes are connected to each other through the primary of the output transformer. The secondary of the transformer has variable inductance/turn number and is connected to the output leads, which connect to the load. The output transformer consists of two air-core, coaxial, solenoidal inductor windings, each consisting of 20 turns. The variable output transformer provides the benefits of DC isolation between the pulse modulator and the load as well as variable turn ratio for impedance matching. It also keeps the output broadband, in case the operator wants to change the operating frequency. Interelectrode capacitance between the grid and plate is inherent in triodes, which motivated the design of tetrode and pentode vacuum tubes that minimize this effect. The capacitance produces feedback between the input and output circuits and may drive the tubes unstable if the load is inductive, which could happen if it is slightly detuned [47]. In order to minimize this feedback, adjustable "neutralizing" capacitors, C_n, [47] were installed on each triode between the plate of one triode and the grid of the other. The neutralizing capacitors cancel out the effect of plate-grid capacitance in each triode. This addition of neutralizing capacitors requires increased grid driving power, but with the benefit of stable operation. Resistors, R_n,

are added in series with the neutralizing capacitors to provide damping to oscillating signals.

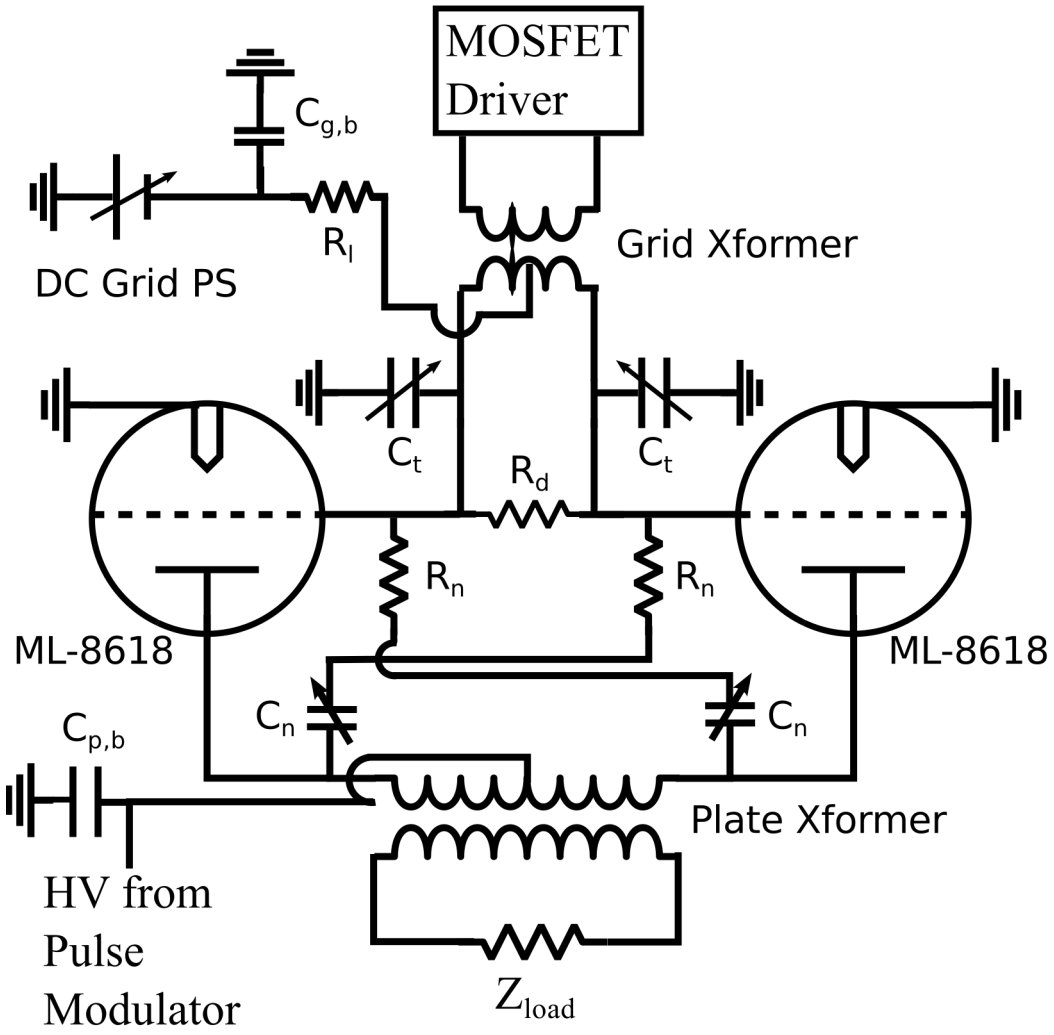

Figure 2.4: Circuit diagram of the RF amplifier. Several components in the amplifier are labeled. Their values are given in table 2.1.

Quantity	Value
Grid Bypass Capacitance, $C_{g,b}$	11 μF
Current Limiting Resistor, R_l	10 Ω
Grid Tuning Capacitors, C_t	10 – 2000 pF
Damping Resistor, R_d	6.8 kΩ
Input Transformer (calc.):	
Primary Inductance	.16 µH
Secondary Inductance	2.5 - 3 µH
Z_{load} (calc.)	~ 800–900 Ω
Neutralizing Capacitor, C_n	20-300 pF
"Neutralizing" Resistance, R_n	100 Ω
Plate Bypass Capacitance, $C_{p,b}$	50 nF
DC Grid Power Supply	0 to -600 V
Output Transformer:	
Primary Inductance	57 µH
Secondary Inductance	121 µH
Mutual Inductance	32-45 µH

Table 2.1: Values of labeled circuit quantities in figure 2.4. All values are measured unless they are labeled as calculated.

2.4 Matching Network

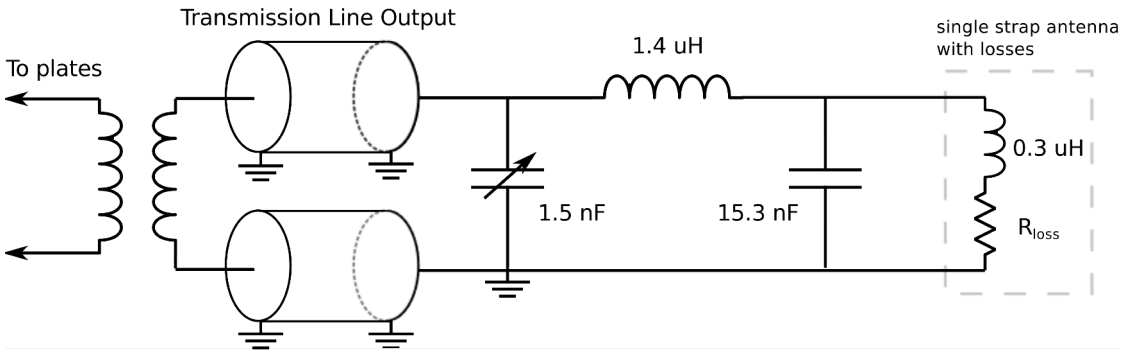

Figure 2.5: Circuit diagram of the matching network, including the antenna load, in the dashed gray box.

The matching network matches the impedance of the antenna with the output impedance of the triodes. Vacuum tubes typically have high output impedances [47], and are often needed to couple power to low impedance loads, such as antennas or audio speakers. The secondary of the transformer is connected to two 22' lengths of coaxial cable with capacitance of 26.7 pF/ft and inductance of .067 uH/ft. The outer conductor of each cable is grounded, and the inner conductor is connected as shown in figure 2.5. The wavelength of light in the cable at 2.4 MHz is 238', thus using 22' sections of the line should not require the inclusion of transmission line effects, and the line acts like lumped circuit elements.

Impedance matching was largely done with a network analyzer, SPICE simulation, and load impedance calculation. Calculations of the frequency response of the load show a double peaked response, with local maxima of the load impedance near 2.4 MHz and 3.5 MHz. Figure 2.6 displays a plot of the calculated

impedance characteristic of the load connected to the secondary coil of the output transformer, pictured in figure 2.5. This plot roughly agrees with the results obtained by the network analyzer measuring the current in the antenna strap while driving the primary of the output transformer. This indicates that the load tuning is well described by the elements in figure 2.5. It was found upon inspection that the maximum current circulating through the antenna occurred with a driving frequency of 2.4 MHz rather than 3.5 MHz, indicating better impedance matching through the output transformer at this frequency.

2.5 The Fast Wave Antenna

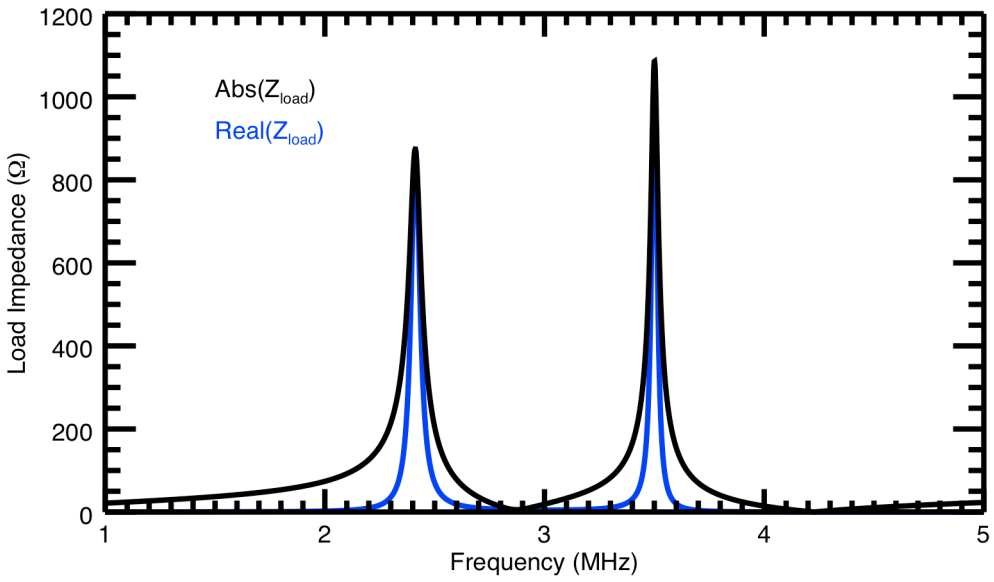

Figure 2.6: Calculated load impedance curve for components connected to the secondary of the output transformer. Network analyzer analysis shows two peaks at these frequencies, indicating the tuning is well described by the elements in figure 2.5.

The fast wave antenna used in this project consists of a single current strap that is enclosed in a slotted copper box. Design of these antennas occupies many talented RF engineers. Here, we opted for the simplest case for the initial RF experiments. A schematic and picture of the antenna are shown in figure 2.7. Two sides of the enclosure have slots machined into them, indicated in figure 2.7. Each slotted side has a machineable glass-ceramic (macor) insulating plate epoxied to its interior in order to avoid a direct connection between the antenna strap and the plasma for particles traveling along $\boldsymbol{B_0}$. The antenna design has elements common to many ICRH wave launchers in tokamaks: a current strap, a box enclosure, slotted sides, and a dielectric material [48 - 50]. During operation, the current strap is oriented such that the current is mainly in the $\hat{y}$-direction in the LAPD (see figure 3.2). This antenna design was the result of an LAPD experiment to determine the fast wave antenna with the highest loading for a launched fast wave coupled to simplicity in construction.

Three types of antenna enclosures were tested during the LAPD experiment. One of the antenna enclosures was the antenna in figure 2.7, henceforth referred to as the slotted-box antenna. A second type of enclosure was a copper box the same size as the slotted box but without slots and macor plates and with the current strap recessed an additional ½" from the box opening. This second enclosure will henceforth be referred to as the full box antenna. The final enclosure tested was a completely bare copper current strap, henceforth referred to as the bare strap antenna.

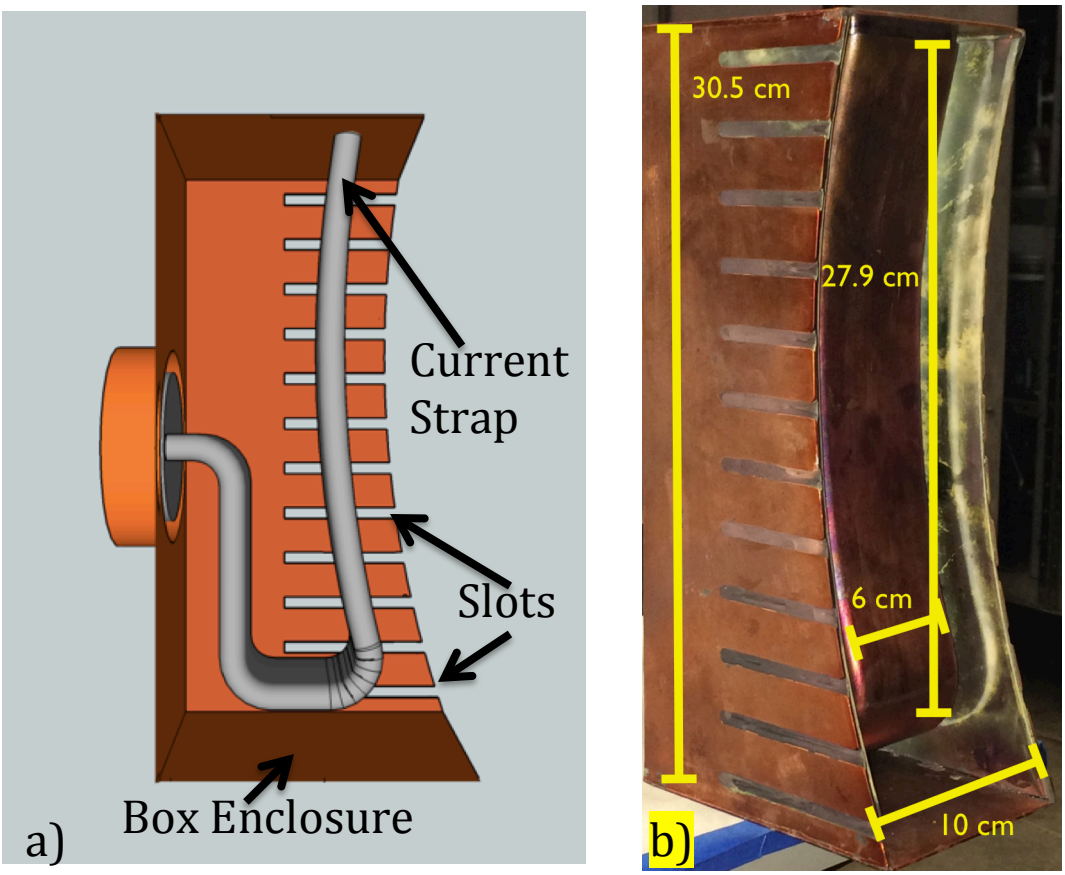

Figure 2.7: The fast wave antenna. a) a schematic without one of the slotted sides. The current strap, slots, and box enclosure are labeled. Missing from the schematic is the macor plate. and b) a picture of the antenna with dimensions.

The Q of all three types of antenna-enclosure combinations was measured both in vacuum and with a plasma load. Here, Q is defined as the ratio $f_r/\Delta f$, where f_r and Δf are the circuit resonance frequency and -3 dB amplitude bandwidth, respectively. This measurement was recorded over a 16 ms time interval in an LAPD discharge to study the variation with plasma temperature and density, which changed dramatically during this time interval. Each Q value represents an ensemble average measurement. During a single LAPD discharge an RF pulse at a

preset frequency was applied to the antenna and the antenna current was digitized.

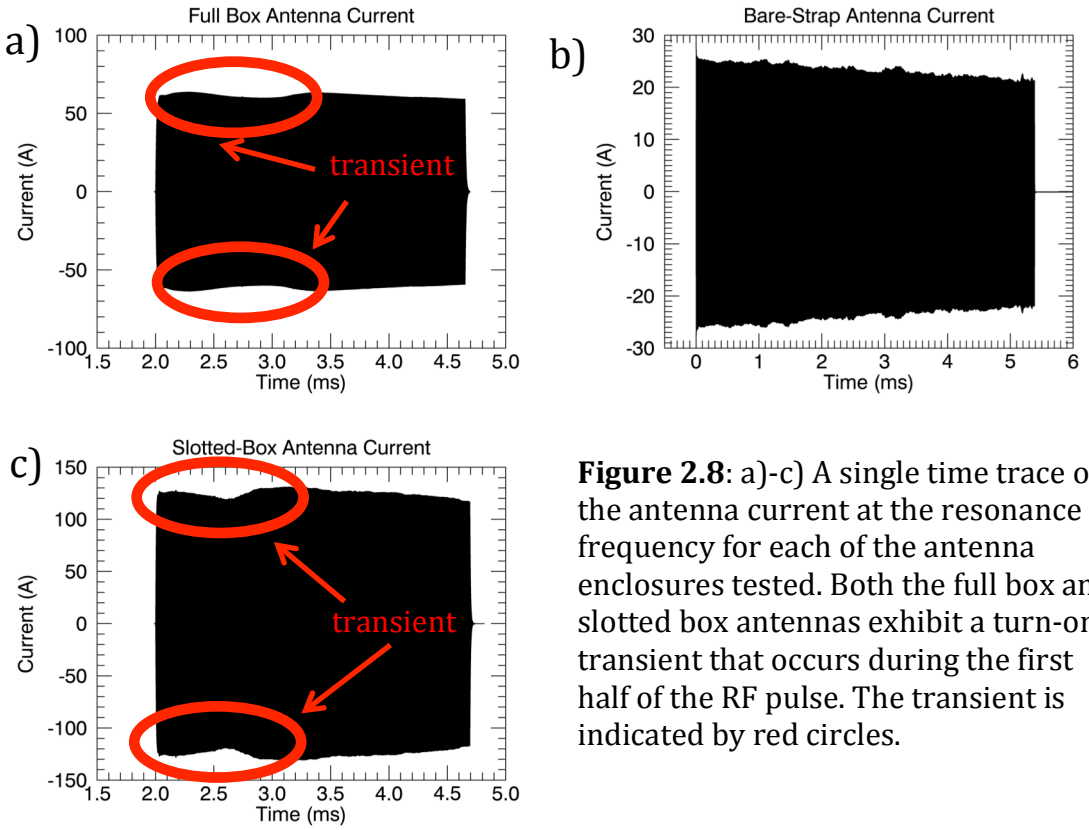

Figure 2.8: a)-c) A single time trace of the antenna current at the resonance frequency for each of the antenna enclosures tested. Both the full box and slotted box antennas exhibit a turn-on transient that occurs during the first half of the RF pulse. The transient is indicated by red circles.

Time traces of individual antenna current measurements are shown in figure 2.8. For a single preset frequency the antenna current was measured during 20 – 25 LAPD discharges. The preset frequency was then changed, and the antenna current measurements were repeated. The frequency was adjusted over 20 – 24 values centered about the antenna resonance frequency. The results of the ensemble averaged Q measurements are displayed in figure 2.9 a. The full box and slotted box curves are broken due to the fact that the antenna exhibits a turn-on transient

during the first half of the RF pulse. Q values calculated during the turn-on transient were discarded. Figure 2.9 a) shows that the slotted box antenna "experiences" a significant decrease in its Q during the LaB_6 portion of the discharge. In fact, its Q decreases by almost a factor of 2. The slotted box antenna has a vacuum Q = 57. By the end of the LaB_6 discharge the slotted box Q drops to Q = 30, indicating that the circuit resistance has increased by a factor of 2 in the high density plasma. Unlike the slotted-box antenna design, the full box antenna's Q changes insignificantly during the discharge. In vacuum, the full box antenna's Q = 73, and at the end of the LaB_6 discharge its value has decreased to Q = 56. Finally, figure 2.9 a) shows the Q profile of the bare strap antenna with a plasma load. In vacuum, the bare strap antenna's Q = 69, and during the LaB_6 discharge it decreases to Q = 8. This is almost an increase in the circuit resistance of a factor of 10! However, note that even in the afterglow plasma the bare strap's Q = 25, which is still a significant decrease from its vacuum value. It is suspected that the strap's direct contact with the plasma is responsible for most of its decrease in Q. The resonance frequency of the slotted-box and full box antenna designs remains the same with a vacuum and plasma load. Unlike the boxed antennas, however, the bare strap antenna circuit resonance frequency changes from 2.44 MHz in vacuum to 2.6 MHz with a plasma during the LaB_6 portion of the discharge, indicating the introduction of reactive circuit elements, probably capacitive coupling, due to the presence of the plasma. Figure 2.9b shows the time evolution of I_{isat} during the discharge at the center of the LAPD axis for reference. Maximum resistance values calculated from the Q values for the

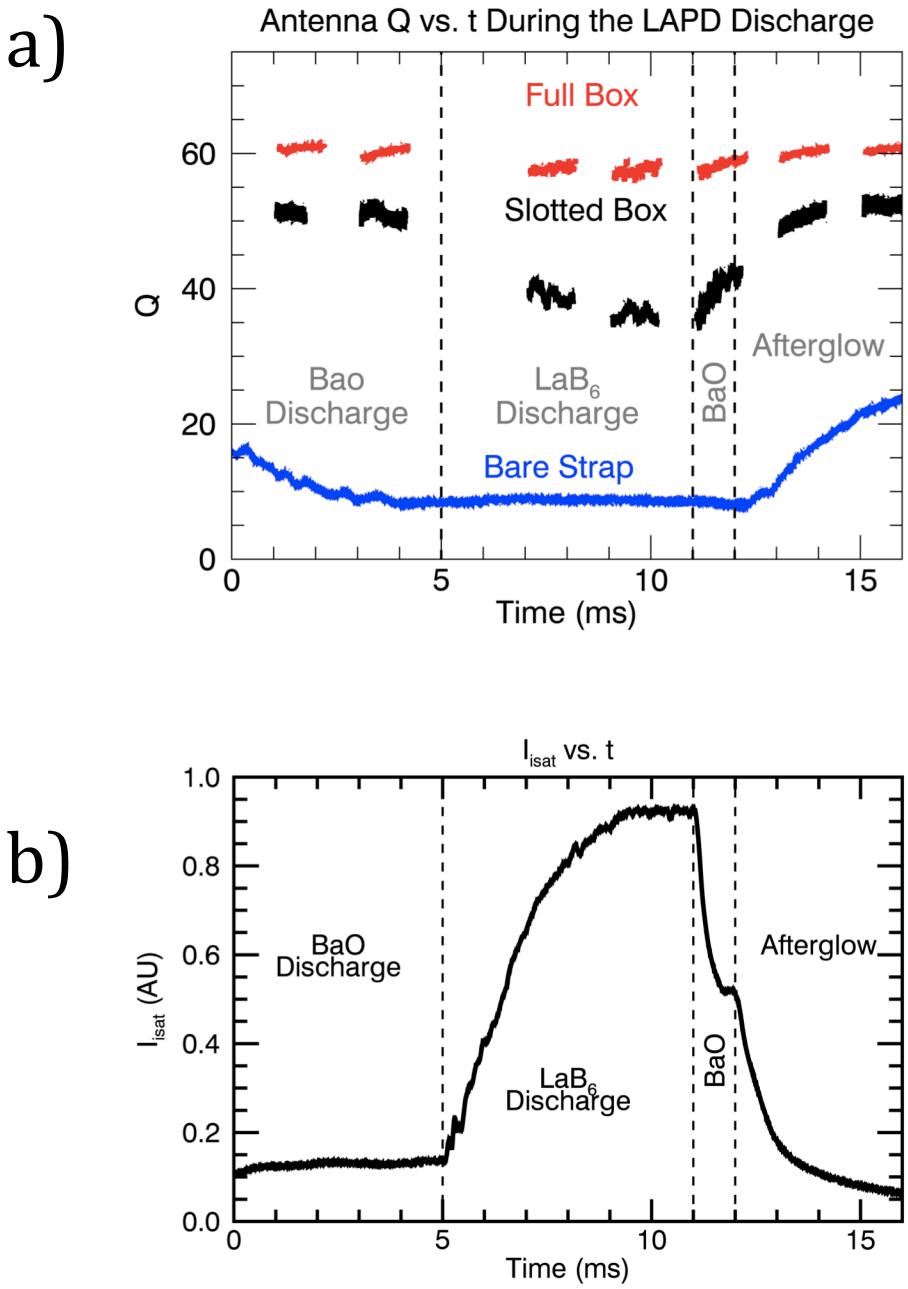

Figure 2.9: a) Ensemble averaged Q profiles vs. time for three different antenna enclosures. Vertical dashed lines indicate times during which different plasma sources were active. The curves for the full box and slotted box enclosures are not continuous in time because calculated Q values that occurred during the turn-on transient were discarded. b) I_{isat} measured the center of the discharge vs. time for reference. For the slotted box antenna, as the I_{isat} increases, Q decreases.

full box, slotted box, and bare strap antennas were, respectively, 0.060 Ω, 0.135 Ω, and 0.734 Ω.

In addition to measuring the Q of the antenna, the radiation efficiency, η, defined specifically for this instance as $\eta_{antenna} = \int \boldsymbol{S_z} \cdot \widehat{dA}/I_{antenna}$ was calculated based on **B**-field measurements made in a plane across the LAPD plasma column at a single axial location. In the previous expression, $\boldsymbol{S_z}$, refers to the Poynting flux along the LAPD axis and the expression represents the radiated power per amp in the antenna. Implicit in this calculation is that the antenna launches a wave and that all the measured **B**-field is due to this wave. Since the **E-**field was not measured, in order to calculate $\eta_{antenna}$, the approximation $\boldsymbol{E}_\perp \propto \boldsymbol{B}_\perp$ was made. The resulting practical definition for $\eta_{antenna}$ based on the limitations of the experiment becomes, $\eta_{antenna} = \int \frac{|B_\perp|^2}{\mu_0} dA/I_{antenna}$. **B**-field measurements were made in an x-y plane across the plasma column 1.9 m away from the antenna. The calculated efficiencies were, $\eta_{full\ box} = (2.2 \pm 1.1)10^{-7}\frac{J}{Am}$, $\eta_{bare\ strap} = (2.4 \pm 1.1)10^{-7}\frac{J}{Am}$, and $\eta_{slotted\ box} = (11.2 \pm 5.3)10^{-7}\frac{J}{Am}$. The results of the efficiency measurements had high measurement error due to the fact that the B-field of the wave varied significantly from shot to shot. The cause of this is uncertain but may be due to the dominant wave mode changing during the RF pulse, which would cause significant changes to the wave profile. In the end a conditional averaging procedure was performed on the wave-field data in order to get rid of the contribution of spuriously high or low wave fields to the efficiency measurements.

The slotted box antenna was chosen as the final antenna design for initial RF experiments because it had higher average efficiency than the full box and bare strap antennas, despite its reduction in Q being less significant than the bare strap antenna. In addition, its construction most resembles tokamak ICRH antennas, such as the Alcator C-Mod antenna in figure 1.1. Finally, the circuit was not dramatically changed between having the antenna face a vacuum and plasma load, meaning tuning would not depend on load conditions.

2.6 Comparison of Antenna B-field

The $\boldsymbol{B_z}$ component of the magnetic field produced by the antenna was measured both on the bench and during the experiment described in the following chapters. A plot of the natural logarithm of $\boldsymbol{B_z}$ vs. distance away from the current strap of the antenna is shown in figure 2.10 for measurements made both on the bench and in the plasma. The magnitudes are scaled to be comparable on the same verticle axis. Also shown in figure 2.10 are linear fits to the ln ($\boldsymbol{B_z}$) $vs. x$ data. The $\boldsymbol{B_z}$ measurements taken on the bench show a much larger radial decay than the measurements taken in the plasma. The $\boldsymbol{B_z}$ e-folding length on the bench is 1.9 cm, whereas the e-folding length in the plasma is 6.7 cm.

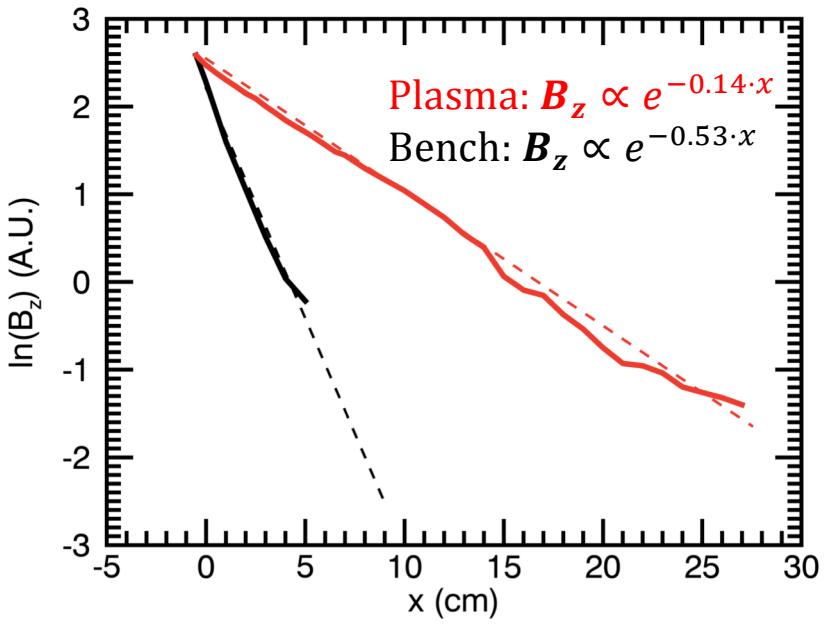

Figure 2.10: B_z vs. x profiles measured on the bench (black) and in the plasma (red). The radial decay of the measured B_z is quicker on the bench than in the plasma.

2.7 RF System Performance

During bench testing of the RF system, the design goal was to couple 1 kA into the antenna tank circuit, shown in figure 2.5. During the bench test, a prototype tank circuit with a measured Q of 14.5 was used. The capacitance was 15.67 nF, and the frequency was 2.91 MHz, giving a resistance of .24 ohms. With 1 kA in the tank circuit, the RMS coupled power was 120 kW, in compliance with the design goals of the amplifier.

Chapter 3

Experimental Methods

3.1 The LAPD

The experiment was conducted in the **LA**rge **P**lasma **D**evice (LAPD) located at the **BA**sic **P**lasma **S**cience **F**acility (BAPSF) at UCLA. A photograph of the LAPD is shown in figure 3.1. A detailed discussion of the LAPD is given in ref. [51], but a brief discussion will be given here for cohesion. The LAPD vacuum chamber is a 24.4 m long cylindrical, stainless steel vessel. It consists of two pump-out sections at each end of the chamber that are 2 m long and 1.5 m in diameter. The middle section of the LAPD is 1 m in diameter and approximately 20 m long. Four turbo-molecular pumps evacuate the chamber to a base pressure less than 5×10^{-7} torr. The middle section of the LAPD is surrounded by yellow and purple solenoidal magnets that produce the axial magnetic field profile in the chamber, as can be seen in figure 3.1. Ten independently controlled power supplies supply current to the magnets, making a variety of magnetic field profiles possible. Typical operating magnetic fields are 200 – 2000 Gauss. Once the chamber is evacuated, gas is inserted into the chamber through Mass Flow Controlers (MFCs). Possible fill gasses include H_2, He, Ne, Ar with a typical fill pressure of 5×10^{-5} torr. The gas and impurity content is constantly monitored by a Residual Gas Analyzer (RGA) located near the BaO cathode.

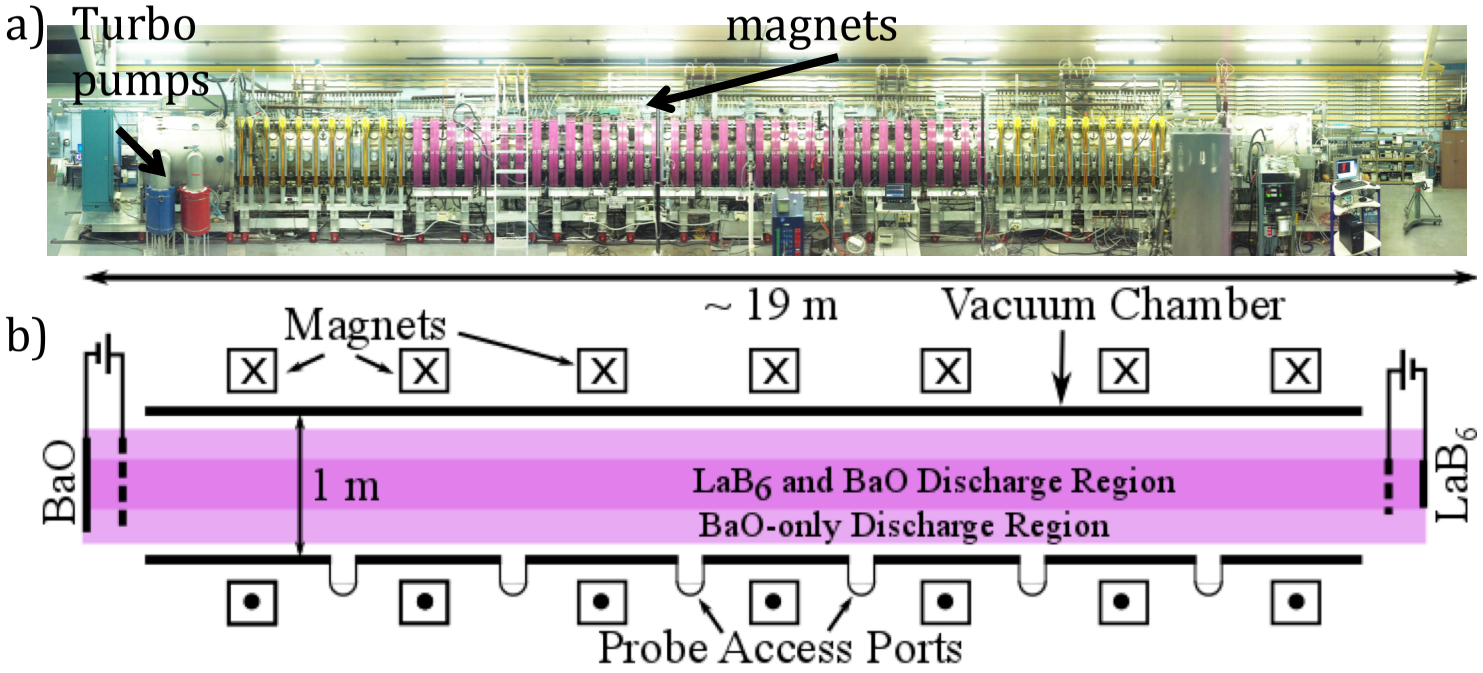

Figure 3.1: a) A picture of the LAPD experiment. The turbo pumps and magnets are labeled in the figure. b) A cutaway schematic of the LAPD. Both the BaO and LaB_6 plasma sources are shown in the figure. When both sources are operating, the density and temperature are higher in the LaB6 and BaO discharge region (labeled) than in the BaO-only discharge region (also labeled). External solenoidal magnets produce an axial magnetic field with an adjustable profile. Probe access ports located every 32.5 cm provide numerous diagnostic access to the plasma.

A BaO cathode-anode pair is located on one side of the machine. The cathode consists of a 60 cm diameter nickel substrate that is coated with BaO [52]. The cathode is indirectly heated by an array of resistive tungsten filaments located behind it. A 50% transparency molybdenum mesh anode is located 50 cm away from the BaO cathode in front of it. When the BaO cathode is heated to a 750° - 800° C, it becomes a strong thermionic emitter, with an emission current density of 2 A/cm^2. Plasma production by the BaO cathode discharge is achieved by pulsing the bias voltage between the cathode and anode [53]. Typical discharge parameters are 40 – 70 V and 3 – 5 kA. The bias voltage on the anode attracts the thermionically emitted electrons from the BaO cathode to the anode. Due to its transparency, some of the electrons accelerated towards the anode are not collected by it and instead continue moving into the middle section of the LAPD chamber where they collide with the fill gas, ionize it, and create a current-free plasma. Ionization also occurs between the cathode and anode, but what is the dominant mechanism in creating the plasma has not been researched in detail. A LaB_6 cathode-anode pair is located on the opposite end of the LAPD chamber from the BaO cathode-anode pair. Its operation is similar to the BaO plasma source. LaB_6 is capable of achieving a higher emission current than BaO, but at a much higher temperature [54]. At ~ 1800 °C, the emission current of LaB_6 is approximately 20 A/cm^2. Thus the LaB_6 can produce hotter, denser plasmas because of the higher number of primary electrons with high energies (> 100 eV). The LaB_6 cathode is a 20 cm x 20 cm square and is indirectly heated by a graphite filament located behind it. The LaB_6 cathode can have its anode placed at a variety of axial locations, the choice of which depends on the type of

experiment. In this experiment the anode was located 32 cm away from the cathode. Each cathode-anode pair electronically floats with respect to chamber ground, and is independently controlled.

The LAPD vacuum chamber is equipped with probe access ports located every 32.5 cm along the z-direction. Each port is equipped with a ball valve [55] that allows for changing a probe's angle. Probes are installed on KF-40 or KF-50 nipples attached to the ball valves and are evacuated using a cryogenic pump-out system before they are opened to LAPD vacuum. Automated probe drives move the probes to user-specified positions within the plasma column. Volumetric data is possible to obtain by creating x-y or x-z planes at different axial locations. During experiments, the probe signals are connected to an A/D converter that stores the information for later analysis. The digitization is triggered at a user-specified delay with respect to the start of the LAPD BaO discharge.

3.2 Plasma Diagnostics

The majority of measurements made are in-situ probe measurements. Probes are inserted into the LAPD vacuum chamber once they have been pumped down to pressures less than $8 \cdot 10^{-6}$ torr, which is below normal neutral fill pressures in the LAPD ($\sim 10^{-5}$ torr). Probes are positioned inside the chamber by automated probe drives that can adjust the x-y or x-z position of the probes. This 2-D motion is achievable because the vacuum ball-joint [55] and double o-ring seals allow independent control of the probe shaft tilt angle and the insertion distance into the chamber, as in figure 3.2. The probe's position inside the LAPD vacuum chamber is calibrated by a telescope looking along the LAPD axis, x = y = 0. Finally, a

probe motion grid, as in figure 3.2, is programmed into the probe motion computer. The probe tip is positioned at each point on the grid, and it acquires data for a user-specified number of LAPD plasma discharges. After it is finished acquiring data at one position it moves to the next position in the grid and acquires data there. In this way, single point, 1-D, or 2-D profiles are built up over many successive discharges.

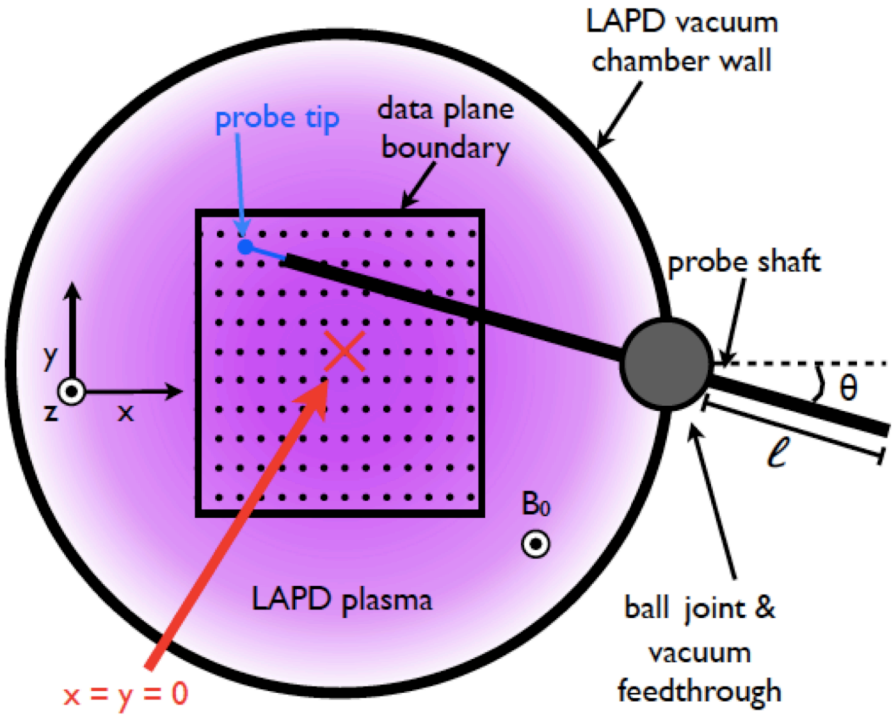

Figure 3.2: Probe motion and data acquisition method in the LAPD. Automated probe drives change the probe's angle and insertion distance into the LAPD vacuum chamber, θ and ℓ, respectively. Though this figure shows an x-y plane, x-z probe motion is possible in the LAPD. An example probe motion is shown in the grid in the figure, each point representing a probe motion. Data sets are comprised of collected data during multiple LAPD discharges at each probe motion location.

3.2.1. Langmuir Probes

One of the workhorse probes in plasma physics is the Langmuir probe, named after Irving Langmuir. The term "Langmuir probe" generally refers to conducting electrostatic probes in direct contact with plasma, regardless of their bias potential with respect to the plasma. They are easy to build and use but may be inaccurate in measuring density. When diagnosing a Maxwellian plasma, information on the plasma parameters can be obtained from the current-voltage characteristic curves, often called I-V curves. Figure 3.3 shows an example of an I-V curve obtained in the LAPD plasma column. Swept I-V curve analysis is well established in other texts [56, 57] and so will only be briefly explained here.

In a Maxwellian plasma with thermal electrons and positively charged cold ions, the electron current to a planar biased probe is given by:

$$I_e(V) = A_p q_e n_e \sqrt{\frac{T_e}{2\pi m_e}} e^{\frac{-q_e(V-V_p)}{T_e}}. \quad (3.1)$$

Where A_p is the probe plus sheath area, q_e is the electron chage, and m_e is the electron mass. T_e is the electron temperature in eV, V_p is the plasma potential, and V is the probe bias potential. This equation is valid for $V - V_p \leq 0$. When $V - V_p > 0$, a constant electron saturation current, I_{esat}, is drawn by the probe in ideal cases. For real probes, however, sheath expansion may cause the collected current to vary at probe biases above the plasma potential. Assuming cold ions, with $V - V_p \leq 0$, the ion current to the probe is the ion saturation current:

$$I_{isat} = .61 A_p q_i n_{i,\infty} c_s, \quad (3.2)$$

where q_i is the ion charge, $q_i = Z|q_e|$, and c_s is the ion sound speed, $c_s = \sqrt{T_e/m_i}$ for cold ions, with m_i the ion mass. The total current to the probe tip for $V - V_p \leq 0$ is then,

$$I_{probe}(V) = I_{esat} e^{\frac{e(V-V_p)}{T_e}} - I_{isat}, \tag{3.3}$$

where quasineutrality has been assumed, e is the unit of the fundamental charge, I_{esat} is defined as $A_p e n_e \sqrt{T_e/2\pi m_e}$ and the electron current is considered positive, as per convention. V_p can be determined from the location of the maximum value of $\frac{\partial I_{probe}}{\partial V}$, and the electron current measured by the probe at V_p is considered I_{esat}. When the probe draws zero net current, it is at the "floating potential," V_f. It can be shown that,

$$V_f - V_p = \frac{T_e}{e} \ln\left(\frac{I_{isat}}{I_{esat}}\right). \tag{3.4}$$

This equation will appear later when considering the behavior of emissive probes with low emission currents compared to I_{esat}. Figure 3.3, includes dashed lines indicating I_{isat}, I_{esat}, V_f, and V_p. The horizontal lines indicate the I_{isat} and I_{esat} values, while the vertical lines indicate V_f and V_p.

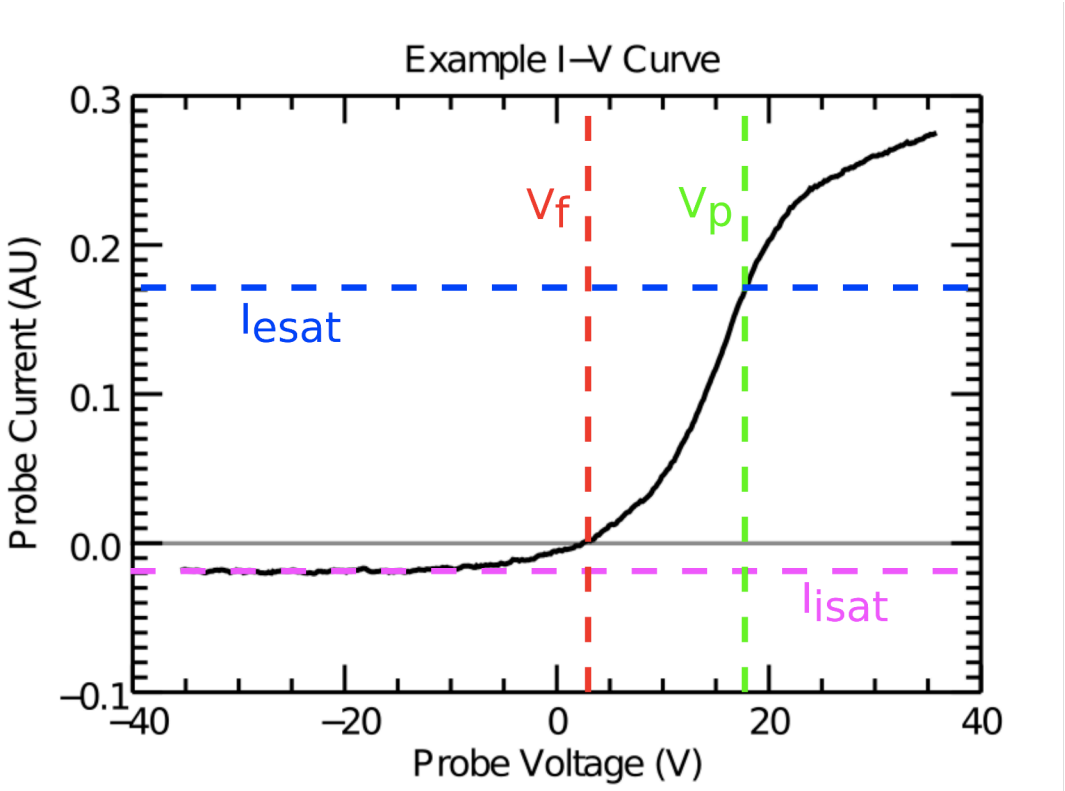

Figure 3.3: An example Langmuir probe I-V trace. Dashed lines indicate V_p, V_f, I_{isat}, and I_{esat}. Electron current is taken as positive.

T_e and V_p are determined from the swept I-V characteristics, and n_e is determined from I_{isat}, with T_e known. The n_e measurement is calibrated with microwave interferometry, which measures the line-averaged density across the plasma column. Langmuir probes are used in various configurations. Swept probes are used to determine T_e, V_p, and n_e, but time resolution of this measurement is limited by the sweeping circuitry. Floating probes measure time-resolved V_f, but the usefulness of this quantity is debatable, especially in the presence of fast electrons [58], RF oscillations [59], or T_e gradients. Langmuir probes may also be used as I_{isat} measurements when connected to a sufficiently negative DC probe bias.

3.2.2. B-dot probes

Fluctuating magnetic field measurements are performed using B-dot probes. The operating mechanism behind the probe is Faraday's law; the probe measures the EMF induced in a loop of wire by time-varying magnetic flux through the loop, $V = -A_{eff}\frac{\partial \boldsymbol{B}}{\partial t}$, where V is the voltage measured across the loop, A_{eff} is the area of the loop, and B is the fluctuating magnetic field parallel to the area normal of the loop. The B-dot probes used in this experiment consist of three orthogonal wire loops wound around a cube with edge lengths of approximately 3 mm. Each winding consists of 10 turns of differentially wound wire (5 turns in each direction). The wire is differentially wound to cancel any electrostatic pickup in the system. The probe windings are covered by a ceramic dome in order to avoid a direct plasma connection with the loops. B-dot probe measurements performed in the LAPD must correct for the probe shaft inclination angle (figure 3.2), though in practice this correction is small.

B-dot probes are calibrated using a network analyzer driving a Helmholtz coil. The probe's frequency response is captured by the network analyzer, and the operating frequency range of the probe is determined by the region in which the probe response is linear. In these experiments, the probe response is linear up to 7 MHz, which is comfortably above the 2.38 MHz launch frequency of the fast wave. More details on the design, operation, and calibration of the B-dot probes can be found in [60] and [61].

3.2.3. Emissive probes

Emissive probes are a diagnostic capable of directly measuring V_p as suggested by Irving Langmuir [62]. Emissive probes consist of a thermionic emitter and the components necessary to heat it. These most often consist of comparatively large current-carrying electrical leads and support structure. In this work, the emissive probe is used as a floating emissive probe [63], though there are other methods for determining the plasma potential from an emissive probe [64].

If a cold, floating probe is in contact with a plasma, then the potential difference, $V_p - V_f$, is governed by equation 3.4. In a Helium plasma with Maxwellian electrons and cold ions, $V_p - V_f \approx 4T_e/e$, with T_e in eV, assuming singly ionized He ions and equal collecting areas for ion and electron current. However, for low emission currents, a floating probe can float closer to the plasma potential by the addition of another term in equation 3.4:

$$V_{f,e} - V_p = \frac{T_e}{e} \ln\left(\frac{I_{isat}+I_{emit}}{I_{esat}}\right), \tag{3.5}$$

where I_{emit} is the emitted electron current. Here the term "float" means the probe's potential is set by the current balance of the plasma rather than the operator. Equation 3.5 above is only valid for low emission currents, where a cloud of negative space charge around the probe does not occur. An important distinction between equation 3.4 and equation 3.5 is that $V_{f,e}$ is used instead of V_f, where $V_{f,e}$ refers to an electron emitting probe's floating potential. Langmuir probes that experience secondary electron emission record floating potentials in this same way. The emissive probe can emit electrons in either a temperature-limited or space charge-

limited regime. In the temperature-limited regime, V_p increases monotonically away from the probe, and the probe's emission current is limited by its temperature according to the Richardson-Dushman equation,

$$J = AT^2 e^{-\phi/T}, \tag{3.6}$$

where J, T, A, and ϕ are the probe's emission current, temperature, Richardson constant, and material work function, respectively. In the space-charge limited regime a cloud of negative charge develops around the probe, and V_p no longer increases monotonically away from the probe tip. In this situation a virtual cathode forms around the probe. The space-charge limited regime is reached when the current emitted by the probe, according to the Richardson-Dushman equations, is comparable to I_{esat}. In the event that the probe's emission current is space-charge limited, as opposed to temperature limited, then

$$V_p = V_e + \alpha T_e, \tag{3.7}$$

where α is an order unity correction to the plasma potential and V_e is the floating potential of a space-charge limited emissive probe. The value of α has been derived analytically using fluid theory [65] to be 1.02 for He. Ye and Takamura [66] developed a model that takes space charge effects into account, and calculate α to be .99 for He. Kinetic PIC codes and theory also show order unity T_e corrections to the emissive probe floating potential [67, 68]. Throughout this work the value of α used in the data analysis will be $\alpha = 1$. The main benefits of the emissive probe over standard swept Langmuir probes is that they offer better time resolution of the

plasma potential, are unaffected by radio frequency (RF) oscillations of V_p, and float closer to V_p than floating probes.

In many applications an emissive probe consisting of a thoriated tungsten filament is sufficient. However, in the BaO discharge plasma in the LAPD, $n_e > 10^{12} cm^{-3}$. A thoriated tungsten probe operating in this plasma density is at its structural limits; in order to be sufficiently emissive it is necessary to heat it to such high temperature that the filament breaks. Therefore, in the LAPD plasma a higher emissivity material, such as CeB_6 or LaB_6 is needed [69]. A resistively heated CeB_6 emissive probe was developed in order to obtain measurements in the LAPD plasma. A picture of the probe is shown in figure 3.4a, along with schematics in figure 3.4b-c. The CeB_6 tip is resistively heated by DC electrical current flowing from 10 AWG copper leads, through the nickel lugs, through the carbon tweezers, and finally through the CeB_6 emitter. The CeB_6 is held in place by the class 3 lever action of the carbon tweezers, with the fulcrum-force-load points being the alumina fulcrum, the steel clamp, and the CeB_6, respectively. The electrically conducting elements of the emissive probe are insulated from the plasma by the Boron Nitride (BN) and silica foam components so that only the tip of the CeB_6 protrudes through a hole in the BN cap and is in direct contact with the plasma. The silica foam is a poor thermal conductor, and helps keep the heat at the probe tip rather than conducting it back to other probe components.

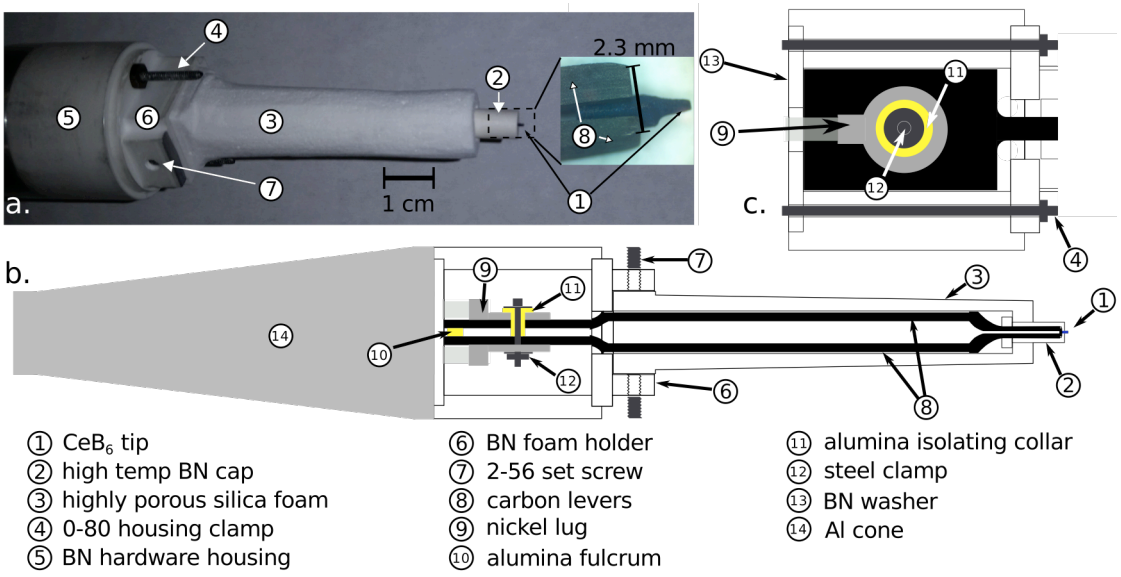

Figure 3.4: CeB_6 emissive probe schematic. a) A picture of the probe. The inset photo is a close-up of the CeB_6 tip in the carbon tweezers. b) A schematic of the emissive probe with components labeled. c) A schematic of the BN hardware housing, rotated 90° from part b) Reprinted with permission from ref. [69]

During experiments, one must be careful to assess whether the probe is sufficiently heated before beginning data acquisition with the probe. The probe is moved to the highest density location in the plasma. This can be roughly determined by I_{isat} or swept Langmuir probe measurements. Once the tip is at the highest density location in the device, it is slowly heated by increasing the DC current through the probe. The heating current is switched off during the entire LAPD discharge, and the probe bias voltage is swept in the same way as with a swept Langmuir probe. Figure 3.5 shows a progression of emissive probe I-V characteristics. At low heating currents the I-V curve resembles a normal swept Langmuir probe I-V curve (the black curve in figure 3.5). As the probe starts emitting, the apparent I_{isat} value increases (red and green curves in figure 3.5). The

probe is hot enough once the emitted current is greater than the collected electron current (the blue curve in figure 3.5). An alternate method of assessing whether the emissive probe is sufficiently heated involves tracking the floating potential of the emissive probe as its temperature is increased. Once the value of the emissive probe's floating potential, the probe is sufficiently emissive. It is then operated as a floating probe, and the value V_e is digitized.

The time response of the emissive probe in this experiment is determined by the distributed capacitance in the copper wires contained in the probe shaft and by the connection impedance between the probe tip and the plasma. An electrically floating emissive probe's effective sheath impedance is larger when the probe is cold and non emitting than when it is heated and emitting approximately I_{esat}. This effect is visually evident in the improved time response of the emissive probe as it is gradually heated from non-emitting to emitting in the space-charge limited regime. In the non-emitting regime, potential oscillations in the ICRF are not visible. Whereas in the space-charge limited emission regime potentials in the ICRF become measureable. The emissive probe was determined to be able to effectively capture plasma potential oscillations up to 10 MHz by connecting the probe tip to the output of a signal generator through a resistor approximating the sheath impedance and verifying that the measured probe potential remains flat.

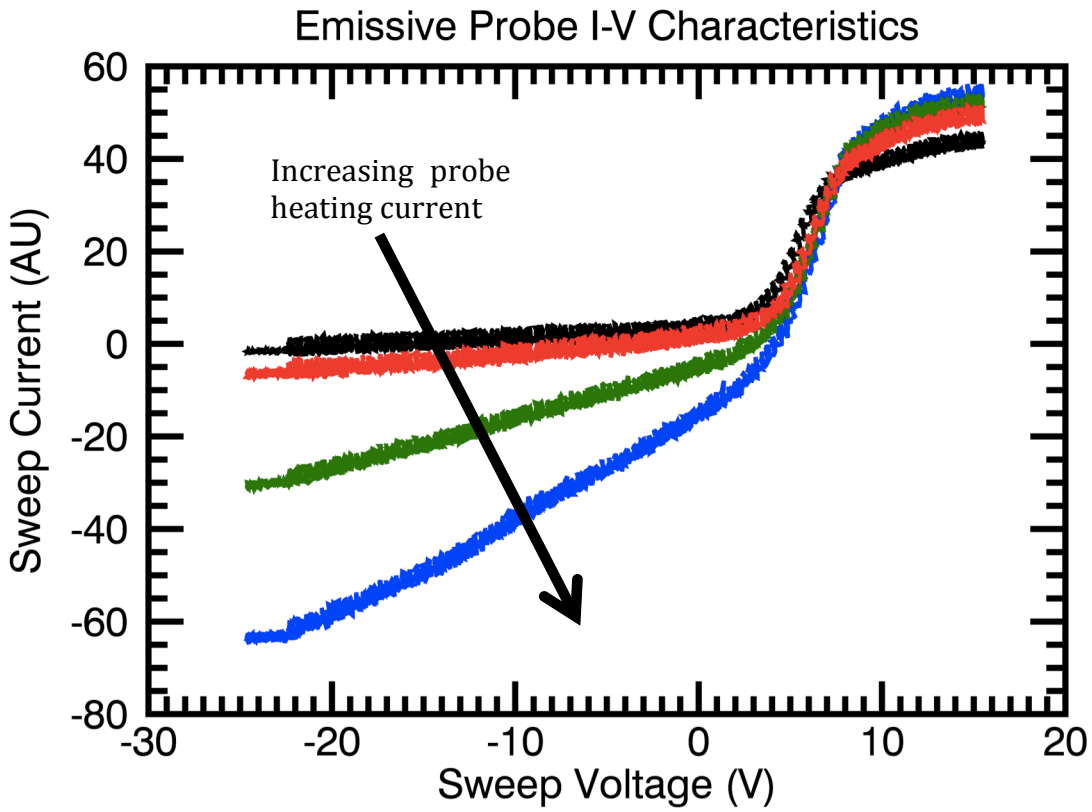

Figure 3.5: Emissive probe I-V characteristics for varying probe heating currents. Heating current, from least to most, in black, red, green, and blue traces. As the emitting probe tip becomes hotter, its emitted current increases, eventually becoming greater than I_{esat}. I_{esat} also increases with heating current, suggesting the thermal expansion of the probe tip.

3.2.4 Mach Probes

The Mach probe is a type of directional Langmuir probe used for measuring the ion flow speed in a plasma. It consists of two conducting probe tips facing opposite directions, each of which is independently biased to collect ion saturation current. Three orthogonally directed pairs of tips may be placed on the same probe, in which case the probe is able to measure the three components of the ion drift velocity. Mach probe analysis is often separated into the magnetized [70, 71] and unmagnetized [72 - 74] ion limits. The unmagnetized approximation is valid for $\rho_i \gg d$, where ρ_i is the ion Larmour radius and d is the typical probe dimension. The

Mach probe conductor area used in this experiment was 1 mm^2, making the value of $d = 1mm$. As for ρ_i, the expression, $\rho_i = v_{Ti}/\omega_{ci} = \sqrt{T_i m_i}/(q_i B_0)$, requires some knowledge of the ion temperature. Assuming $T_i \approx 1\ eV$, which is consistent with spectroscopic measurements of the ion temperature in the LAPD, and singly ionized He, then $\rho_i = 2.04\,mm$, in which case the unmagnetized approximation is marginally satisfied. In fact, ρ_i reaches the collector size when the ion temperature is .24 eV.

Unmagnetized Mach probe interpretation relies on the ratios of collected ion saturation currents à la [72, 73],

$$\frac{J_{iisat}^{+}}{J_{iisat}^{-}} = e^{KM}, \tag{3.8}$$

where M is the ratio of ion drift speed, v_{di}, to the ion sound speed, c_s, K is a proportionality constant of order unity, and superscripts '+' and '–' refer to upstream and downstream facing probe tips. Eq. 3.8 agrees with PIC simulations of a spherical Mach probe for a K value of 1.34[73] when the probe is much larger than the Debye length. Eq. 3.8 has been experimentally validated with flows deduced by LIF [75] and emissive probes [74] with a value of K in the same ballpark, K = 1.3. Most K values determined by experiment, simulation, and theory determine that K falls in the range $1 \leq K \leq 2$. As such, in the interpretation of Mach Probe data, a value of K = 1.3 will be used throughout the analysis. This will give good order of magnitude measurements. However, when the Mach probe dimensions are comparable to the Debye length, $.1 \leq d/\lambda_{De} \leq 10$ the value of K can become negative because the electric field of the downstream collector may accelerated ions

moving upstream into it [76]. This has been experimentally verified [77]. The probe tip used in this experiment has the lowest value of $d/\lambda_{De} \approx 33$ ($T_e = 3.8, n_e = 2 \cdot 10^{11} cm^{-3}$), safely putting it in the "positive K" operating regime.

Recalling from above that the measured value of $I_{isat}^{\pm}$ is proportional to the probe collection area, means that the value of R in equation 2.8 needs to be calibrated to account for different collection areas of realistic probe tips. In principle, this can be accomplished by positioning the probe at a single location in the plasma and acquiring I_{isat} values with both tips. Afterwards, rotating the probe 180° and following the same procedure should give a calibration to the area of $b = A_a/A_b = (I_a^+ + I_a^-)/(I_b^+ + I_b^-)$, where $I_{a,b}^{\pm}$ refers to the measured probe signal, with subscripts a and b referring to the different probe tips, superscripts "+" and "–" refer to upstream and downstream facing. Unfortunately, in the experiments described this calibration method was not suitable, possibly due to sheath effects [78]. Instead, the value of $(\Delta I_a^+)/(\Delta I_b^-)$ was taken as the area calibration factor, where ΔI is the current difference on one probe tip between the plasma discharge and the afterglow plasma.

3.3. Summary of experiment

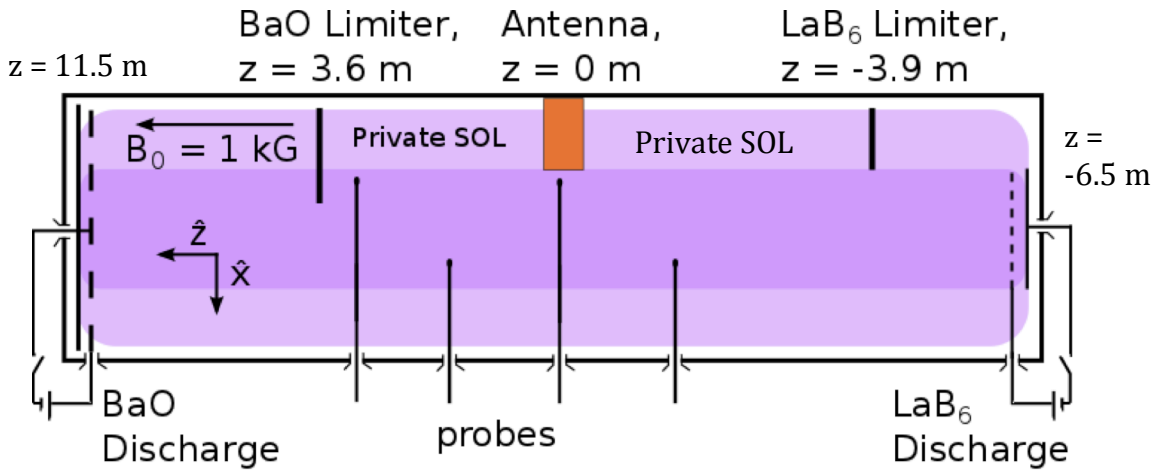

Figure 3.6: Experiment schematic. The fast wave antenna is inserted into the chamber. Its axial location defines z = 0 m. Limiters consisting of 12"x12" stainless steel plates were inserted at z = 3.6 m and z = -3.9 m to x = -4.5 cm and x = -9.9 cm, respectively. Both the BaO and LaB_6 plasma sources were in operation. A private SOL is created between the antenna and the limiters. Probe measurements were made in the private SOL and the bulk plasma.

The main findings of this thesis follow a single experiment performed on the LAPD. The experiment schematic is shown in figure 3.6, and it can be considered a cut across y = 0 in the LAPD vacuum chamber. In the Cartesian coordinate system used in the experiment, z = 0 is the location of the fast wave antenna port, and both x = 0 and y = 0 fall along the center of the LAPD axis. Both the BaO and LaB_6 discharges are in operation during the experiment. The BaO discharge voltage and current are 58 V and 3.1 kA, and the LaB_6 discharge voltage and current are 120 V and 1.25 kA. It was decided that operating the LaB_6 at lower discharge current than its maximum was beneficial for obtaining emissive probe measurements during the data run.

Limiters consisting of 12”x12” 304 stainless steel plates whose area normal vectors, were aligned with $\hat{z}$, were inserted on either side of the antenna. The BaO limiter extended from x = -4.5 cm to x = -35 cm, and the LaB_6 limiter extended from x = -9.9 cm to x = -40.4 cm. At y = 0, the antenna extends to x = -10 cm. Both limiters and the antenna are connected to chamber ground. The limiters serve the function of blocking direct connection through the plasma between the antenna and the floating cathode-anode discharge circuits at either end of the machine. They also serve the additional purpose of providing a ground reference potential to V_p measurements inside the private scrape-off layer plasma that exists between the limiters and the antenna.

The antenna is operated at 2.38 MHz for 2000 RF cycles. The value of t=0 is chosen to correspond to the starting time of the RF antenna pulse. Often, time will be reported in normalized time, $t/t_{RF} = tf_{RF}$, where t is time relative to the start of the RF antenna pulse, and f_{RF} is the launch frequency.

Because there are many objects inserted into the plasma during this experiment, there is certainly a modification of the plasma parameters. n_e, V_p, and T_e color maps all show traces of the antenna outline. Figure 3.7-3.9 shows the measured n_e, V_p, and T_e before the start of the RF pulse. Table 3.1 shows typical experiment parameters, in the main discharge region of the plasma (around x = y = 0) and in the private scrape-off layer region (x = -15 cm, y = 0). T_e values were determined from swept Langmuir probe measurements at z = 65 cm. n_e values were determined using the T_e values and I_{isat} measurements at z = 1.3 m, and V_p values

were determined from emissive probe measurements with T_e corrections at z = 65 cm.

Quantity	Main Discharge (z = y = 0) value	Private SOL (-15 cm ≤ x ≤ -10 cm, y = 0) value
T_e (eV)	10	3.8 - 8
n_e (cm^{-3})	$8 \cdot 10^{12}$	$2 \cdot 10^{11} - 1 \cdot 10^{12}$
$\lambda_D (\mu m)$	8.3	32.4 – 21.0
v_{Te} (cm/s)	$1.33 \cdot 10^{8}$	$0.82 - 1.19 \cdot 10^{8}$
f_{rf} (MHz)	2.38	2.38
f_{rf}/f_{ci}	6.23	6.23
f_{pi}/f_{rf}	125	19.7 - 44.1
ν_{ee} (MHz)	8.43	0.94 - 1.6
f_{LH} (MHz)	32.5	26.8 – 31.2
c_s (cm/s)	$1.55 \cdot 10^{6}$	$9.6 \cdot 10^{5} - 1.4 \cdot 10^{6}$
ν_{in} (Hz)	0	527 - 700
ν_{ei} (MHz)	2.2	0.063-0.295
ρ_i (cm)	.2	.2
$f_{e,\,transit}$ (MHz)	13.3	8.2 – 11.9

Table 3.1: Typical operational parameters in the experiment in both the main discharge and the private SOL created by the limiters and the antenna. The fill gas used during the experiment was He. In the main discharge, 100% ionization is assumed.

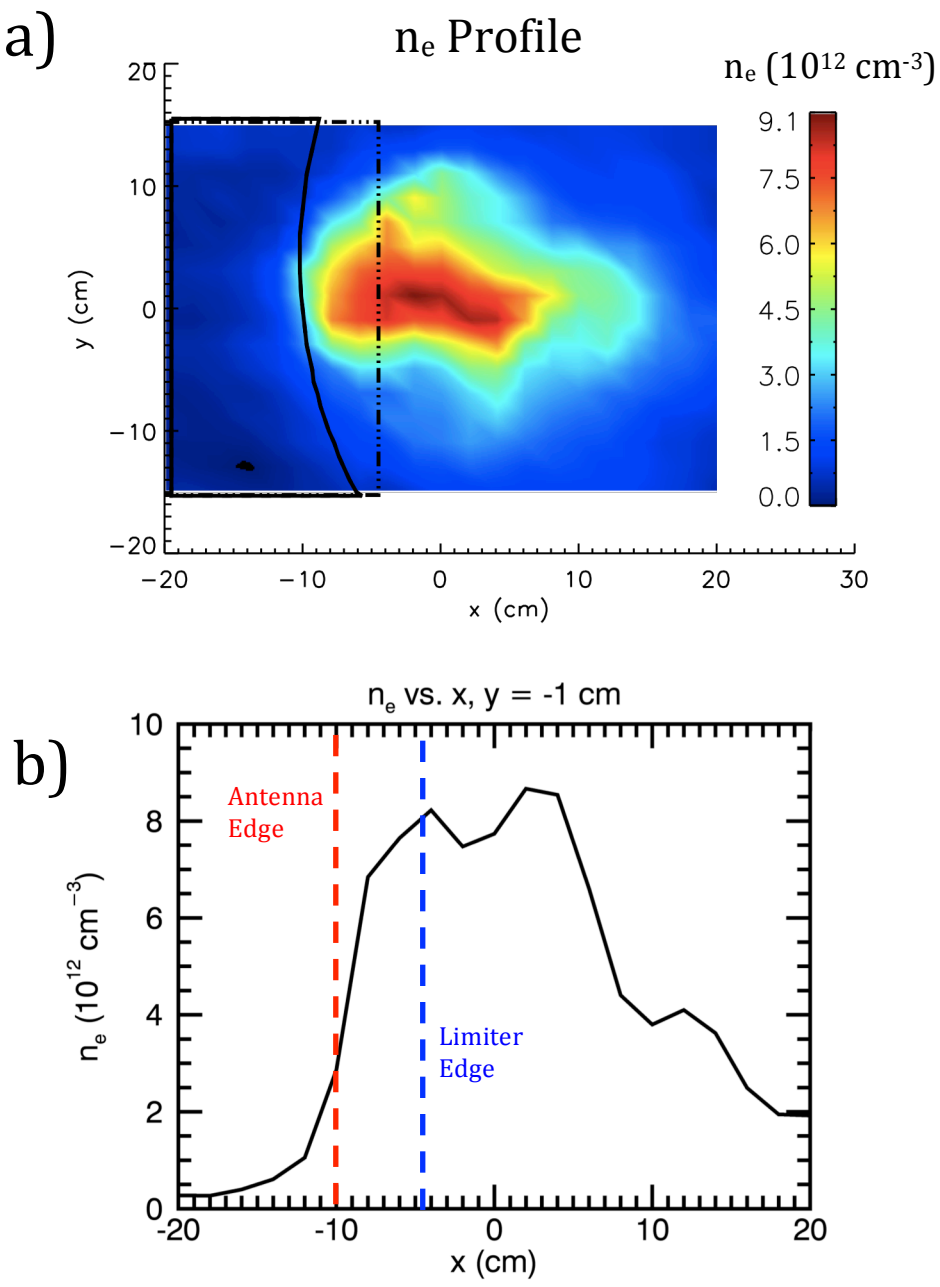

Figure 3.7: Electron density, n_e, measured with a Langmuir probe before the RF pulse. Plotted values are calculated using equation 3.2 with T_e measurements obtained at z = 0.65 m with a swept Langmuir probe and I_{isat} measurements obtained at z = 1.3 m and calibrated against microwave interferometers. a) A color map of n_e. The outline of the antenna and the limiter at z = 3.6 m is shown for reference. The LaB_6 plasma discharge region in the center of the column is denser than the BaO region. The density if the "shadow" of the antenna is less than elsewhere. b) A line plot of n_e vs. x at y = -1 cm.

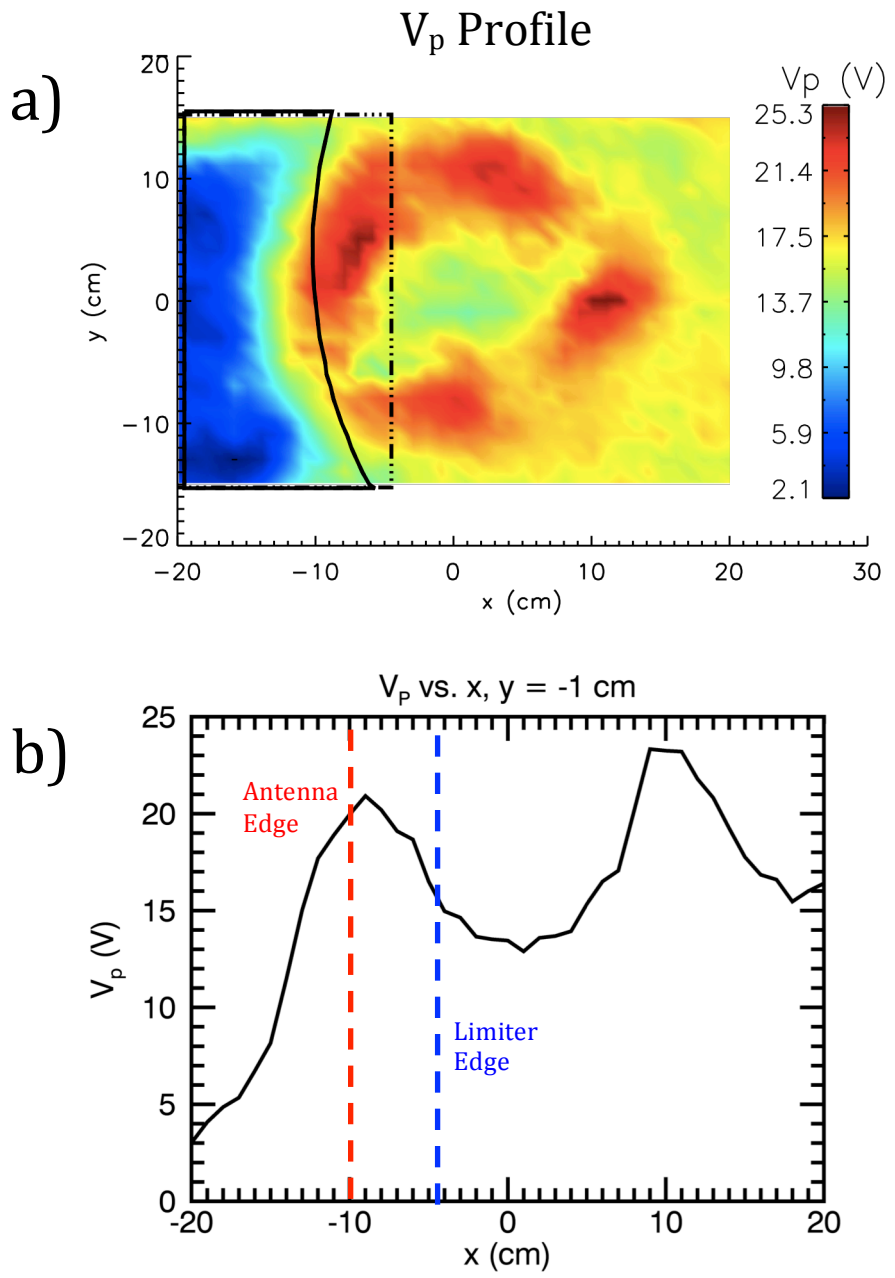

Figure 3.8: Plasma potential, V_p, at z = 0.65 m measured with an emissive probe before the RF pulse. Plotted values are calculated using equation 3.7 with T_e measurements obtained at z = 0.65 m with a swept Langmuir probe. a) A color map of V_p. The outline of the antenna and the limiter at z = 3.6 m is shown for reference. V_p in the private SOL is clearly influenced by the presence of the antenna b) A line plot of V_p vs. x at y = -1 cm. V_p in the middle of the plasma column, $|x| \leq 5$, is lower than at the edge of the LaB_6 discharge plasma, $|x| \approx 10$.

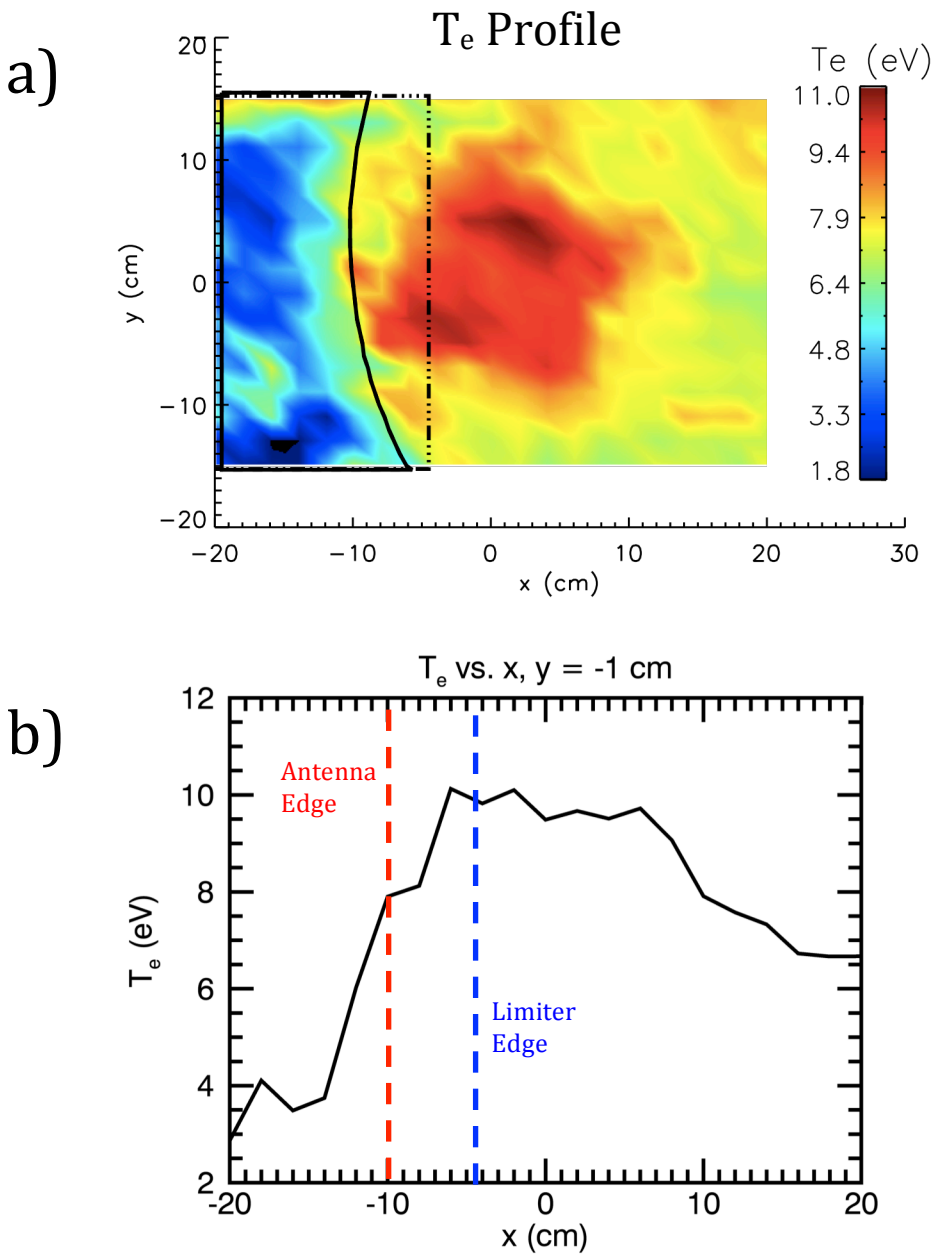

Figure 3.9: Electron temperature, T_e, at z = 0.65 m measured with a swept Langmuir probe before the RF pulse. a) A color map of T_e. The outline of the antenna and the limiter at z = 3.6 m is shown for reference. T_e in the private SOL is clearly influenced by the presence of the antenna b) A line plot of T_e vs. x at y = -1 cm.

Chapter 4: Properties of RF-Enhanced Plasma Potentials in the LAPD

4.1 Observed Properties of the RF-Enhanced Plasma Potentials

During this experiment the ICRF antenna pictured in figure 2.7 was oriented vertically in the LAPD vacuum chamber, and at y = 0 it extended to x = -10 cm. The antenna outline is clearly seen in the color map of the plasma parameters in the previous chapter (fig 3.7-9 a)). In most cases the RF amplifier supplied 120 kW +- 40 kW of RF power to the plasma, which corresponds to an RMS antenna current of 565 A. For comparison, the power supplied by the

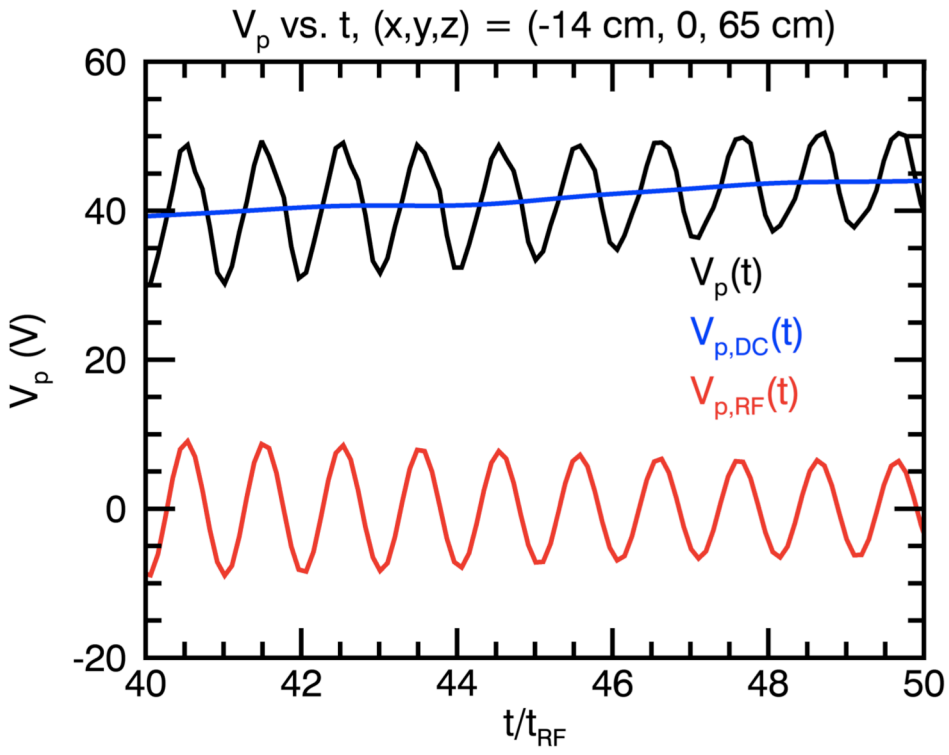

Figure 4.1: $V_p(t)$, $V_{p,DC}(t)$, and $V_{p,RF}(t)$ curves in black, blue, and red, respectively. $V_{p,DC}(t)$ changes on a timescale slower than the RF oscillation period.

BaO and LaB_6 sources was 180 kW and 150 kW, respectively. Only the capacitor bank voltage was changed during power scans of the RF amplifier, and it was varied from 1 kV to 12 kV. When the RF pulse was applied to the antenna, the floating potential of the space-charge limited emissive probe, V_e, was seen to change. Throughout this discussion, measured quantities may be divided into their various frequency components as,

$$V_p(t) = V_{p,DC}(t) + V_{p,RF}(t). \quad (4.1)$$

Figure 4.1 shows a plot with all of these components clearly labeled. The low-pass filtered data, the quasi DC component, is obtained by digitally applying a filter to the quantity between 0 and

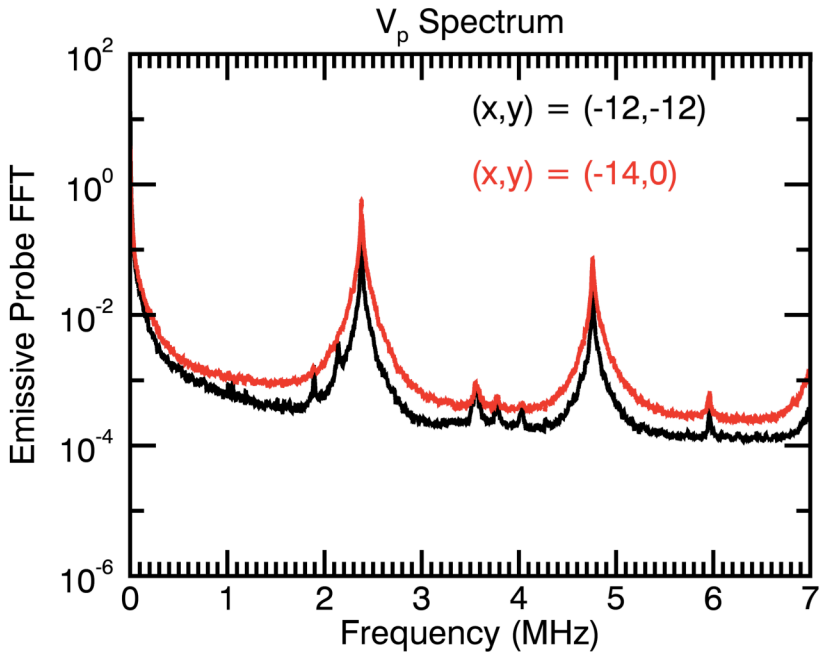

Figure 4.2: A power spectrum of the emissive probe signal at two locations. The magnitude of the RF amplifier frequency at 2.38 MHz is almost 10x more than the magnitude of the second harmonic signal.

1 MHz. It is called the "DC" component of the quantitiy because its time variation is slow compared to the RF period and is denoted by a "DC" in the quantity subscript, as in $V_{p,DC}$. The RF component refers to the digitally band-pass filtered data between 1 – 4 MHz and is dominated by the RF launch frequency. It will be denoted by an "RF" in the quantity subscript, as in $V_{p,RF}$. The V_p trace in figure 4.1 does not appear to have a large second harmonic component to the oscillation. A V_p frequency spectrum is shown in figure 4.2, where the red trace shows the frequency spectrum of the data in figure 4.1. Figure 4.2 shows that, indeed, the fundamental RF frequency component is approximately 10x larger than the second harmonic.

Figure 4.3 a) shows a plot of V_p vs. time for the entire RF pulse during a single LAPD discharge when the probe tip was located at (x,y,z) = (0,0,65 cm). Figures 4.3 b) and c) show the antenna current, $I_{antenna}$, and the potential of the BaO anode, V_{BaO}, respectively. All potentials are measured with respect to the LAPD vacuum chamber ground. In figure 4.3 a) and c) the gray traces are the measured values of the potentials, and the blue lines are a result of digitally applying a low pass filter to the raw data. Within 100 RF cycles after the start of the RF pulse, the DC V_e increases and subsequently establishes itself at a near-steady value. The same is true of the DC BaO and LaB_6 anode voltages, V_{BaO} and V_{LaB_6}, respectively. In fact, the DC voltage increase on the anodes is the same as the increase in $V_{p,DC,}$ along the center of the LAPD axis. After the RF pulse, the antenna current returns to 0 A. The BaO and LaB_6 discharges both end at $\frac{t}{t_{RF}} = 3570$, well after the phenomena discussed in this and the next chapter.

The change in $V_{p,DC}$ is spatially dependent, as can be seen in figure 4.4, which now shows the DC plasma potential, $V_{p,DC}$, at $\frac{t}{t_{RF}} = 199.84$. The DC plasma potential is calculated from $V_{p,DC} = V_{e,DC} + \alpha T_e$ [66], where the value of α used is 1.0, rather than the recommended value

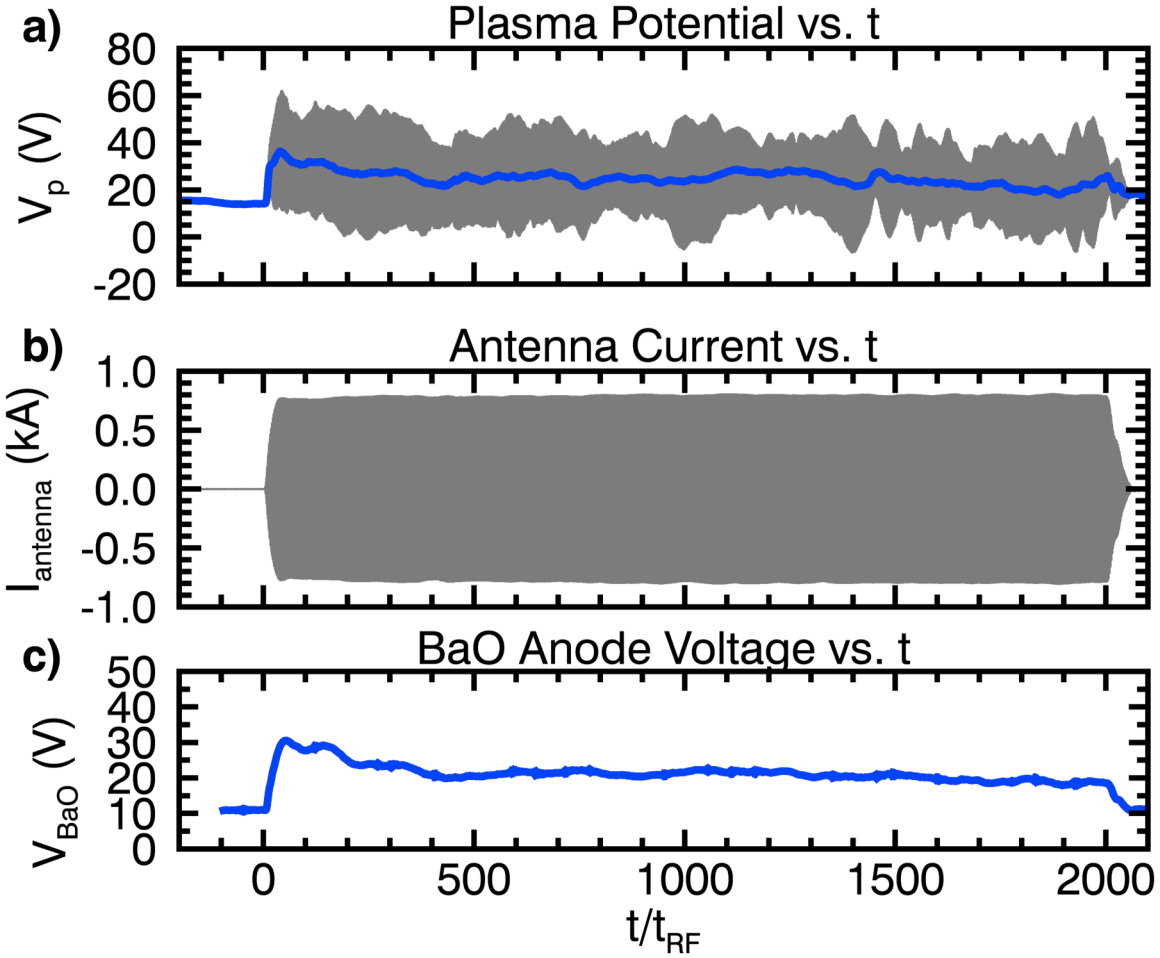

Figure 4.3: Timing in the LAPD ICRF experiment. a) V_p and $V_{p,DC}$ vs. t. b) $I_{antenna}$ vs. t. c) $V_{BaO,DC}$ vs. t. The gray (blue) curves are the raw (low pass filtered) data. $V_{p,DC}$ and $V_{BaO,DC}$ both increase in response to the RF pulse applied to the antenna.

of 0.99 from ref. 66. This produces a negligible change in the results. Typical errors in the value of T_e are 20-30% in the SOL and 10% in the main discharge based the standard deviation of five T_e measurements taken before the RF pulse. The electron temperature used in the calculation of $V_{p,DC}$ is measured with a swept Langmuir probe before the RF pulse to the antenna was applied. This is a limitation on the data, but in practice it is not a large limitation. $V_{e,DC}$ changes up to 80 V at the top and bottom of the antenna, and T_e is expected to change by no more than 10 eV. This limit to the expected change in T_e comes from the fact that highest observed electron

temperature values in the LAPD are of order 10 eV. This means that changes in $V_{e,DC}$ are much larger than any expected change in T_e, and that using the measured T_e before the RF pulse to calculate the $V_{p,DC}$ values will not greatly change the results. Indeed, swept probe measurements performed 60 us after the RF pulse with a 100 us sweep time show modest increases in T_e of up to a maximum of 3 eV in both the main discharge and SOL. The spatial locations where T_e is higher after the RF pulse do not correspond to where the largest V_p is observed. Assuming all of the RF power is somehow transferred to heating electrons for an $18\ m$ plasma column with an axially uniform density profile given in figure 3.7, the expected energy increase for each electron would be over 113 eV! This calculation ignores all mechanisms of energy loss for the plasma, for example radiative energy loss. A more reasonable calculation compares the power ratios of the BaO plasma source to the injected RF power, 180 kW vs. 120 kW, respectively. The BaO plasma source produces approximately 6 eV plasma column. Increasing its power by two-thirds, assuming a linear relationship between power and T_e, would increase the temperature by 4 eV. The measured 3 eV increase in electron temperature is, at any rate, within reasonable expectations. Figure 4.4 is assembled from data collected at z = 65 cm. Outlines of the antenna box enclosure, the current strap, and the BaO limiter are shown in the figure for convenience and reference. The most significant rectification of the plasma potential occurs in line with the top and bottom of the antenna, qualitatively consistent with floating potential and IR camera measurements in Tore Supra, e.g., [18].

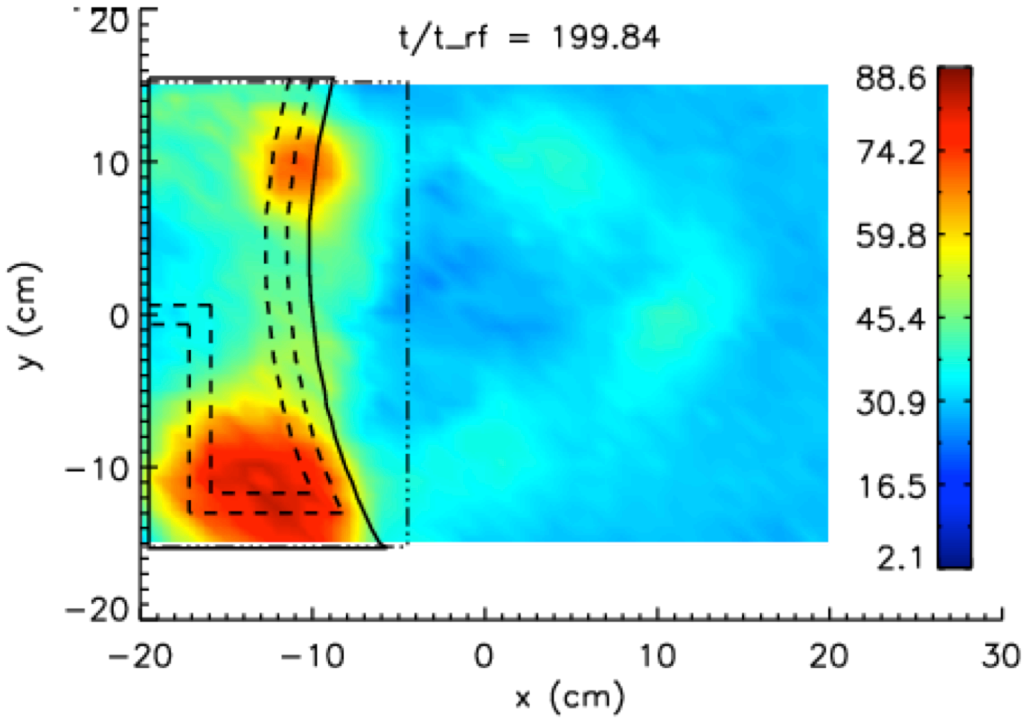

Figure 4.4: $V_{p,DC}$ measured at z = 65 cm and $\frac{t}{t_{RF}} =$ 199.84. The location of the antenna box enclosure(—), the current strap internal to the box enclosure (--), and the limiter located at z = 3.6 m. (··· —) are marked for reference. The most significant values occur at the top and bottom of the antenna box.

Since the value of $V_{p,DC}$ reaches almost 100 V, singly charged He ions in the bulk plasma are accelerated into the antenna enclosure with energies of almost 100 eV. This energy is sufficient to cause He^+ sputtering on Cu [79] with a sputtering yield of a single Cu atom sputtered for every 22.2 He^+ atoms impinging on the antenna. Evidence for the antenna material sputtering is observed by the copper coatings that develop on probes used during this experiment. Figure 4.5 shows pictures of B-dot and emissive probes before and after being used in this experiment. Both the emissive and B-dot probes have copper deposited on them. The B-dot probe has a single copper stripe, oriented in the $\pm\hat{y}$ direction. The presumed reason for this is that Cu deposits form on the entire surface of the B-dot probe tip while it is in the plasma, but

plasma ions and electrons, having a smaller gyro-radius than the sputtered copper, strike the probe tip where $d\hat{A} \cdot \hat{z} \neq 0$, where $d\hat{A}$ is the differential area normal of the B-dot probe. Similarly, Cu deposits form on the porous silica foam component of the emissive probe, except close to the probe tip and carbon tweezers where the temperature of these components approaches 2000° C. Figure 4.5 shows clear evidence that plasma-materials interaction (PMI) is an important consideration in ICRH studies, even at the modest antenna powers in this experiment (~ 120 kW) compared to tokamak antenna powers (> 1 MW). Large values of $V_{p,DC}$ will accelerate plasma ions into antenna components, and antenna materials will sputter and end up in the bulk plasma. A combination of approaches to address this problem during ICRH is necessary, including designing antennas, through proper materials selection, that are resilient to high-energy ion bombardment, determining mitigating scenarios of antenna operation that

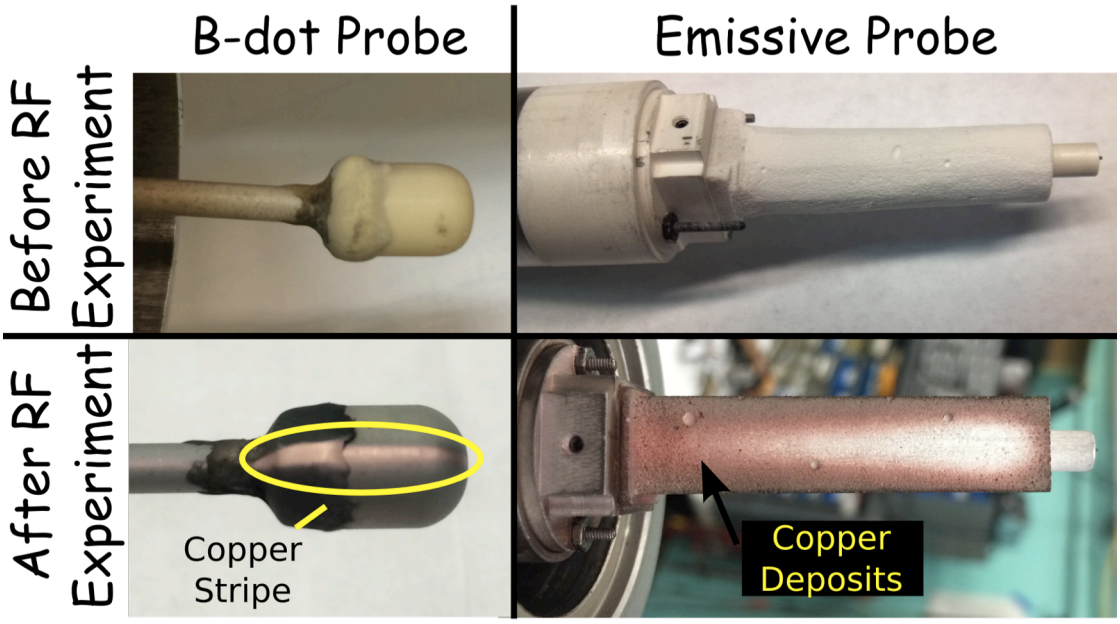

Figure 4.5: Pictures of probes before and after being used in the ICRF experiment described in this thesis. The top/bottom rows shows probes before/after being used. The left/right column show B-dot/Emissive probes. There are distinct copper stripes on the B-dot probes. The silica foam of the emissive probe has copper deposits.

produce smaller and acceptable values of $V_{p,DC}$, and operating in plasma scenarios less prone to being influenced by PMI.

The rectified potentials that form in the LAPD bias the field lines for several meters. Figure 4.6 illustrates this. The emissive probe was used to measure V_e at z = 0, 0.65 m, 3.25 m, and 4.9 m axial locations. V_e measurements taken at z = 0 m were obtained only on the y = 0 line between $-9\ cm \leq x \leq 20\ cm$ due to technical difficulties with the emissive probe, while measurements at z = 0.65 m, 3.25 m, and 4.9 m axial locations were performed in an x-y plane. Figure 4.6 a)-c) shows single line plots of $V_{e,DC}$ for various lines cutting across the LAPD column. Figure 4.6 d) shows the locations of these lines for reference. All lines show the 20 cycle average of $V_{e,DC}$ between $200 \leq t/t_{RF} \leq 220$. As can be seen from figures 4.6 a)-c), the $V_{e,DC}$ profiles line up, within experimental uncertainty, regardless of axial location. Exceptions to this occur most notably at and around $x = \pm 10\ cm$, where there is a strong density gradient due to the LaB_6 plasma source region. These locations correspond to where the I_{isat} signals show a local maximum in their magnitude of low frequency oscillations (10 – 50 kHz), suggesting the presence of drift waves at this location. The existence of drift waves at the LaB_6-BaO discharge region interface is likely to contribute to the low frequency measurements of $V_{e,DC}$. The magnetic field magnitude at the discharge region interface was not observed to be larger than in the LaB_6 discharge region, suggesting that edge modes did not contribute to the observed $V_{e,DC}$ peaks at $x = \pm 10\ cm$. Field lines experience a uniform potential increase along the $\hat{z}$ direction, within the region data were collected. This confirms the conjecture that the RF enhancement to the plasma potential is a global effect along magnetic field lines. The high potential rectification between the antenna and the limiter does not occur between the limiter and the BaO anode, as can be seen by comparing the blue curves to the other curves in fig 4.6 a) – c). These blue curves

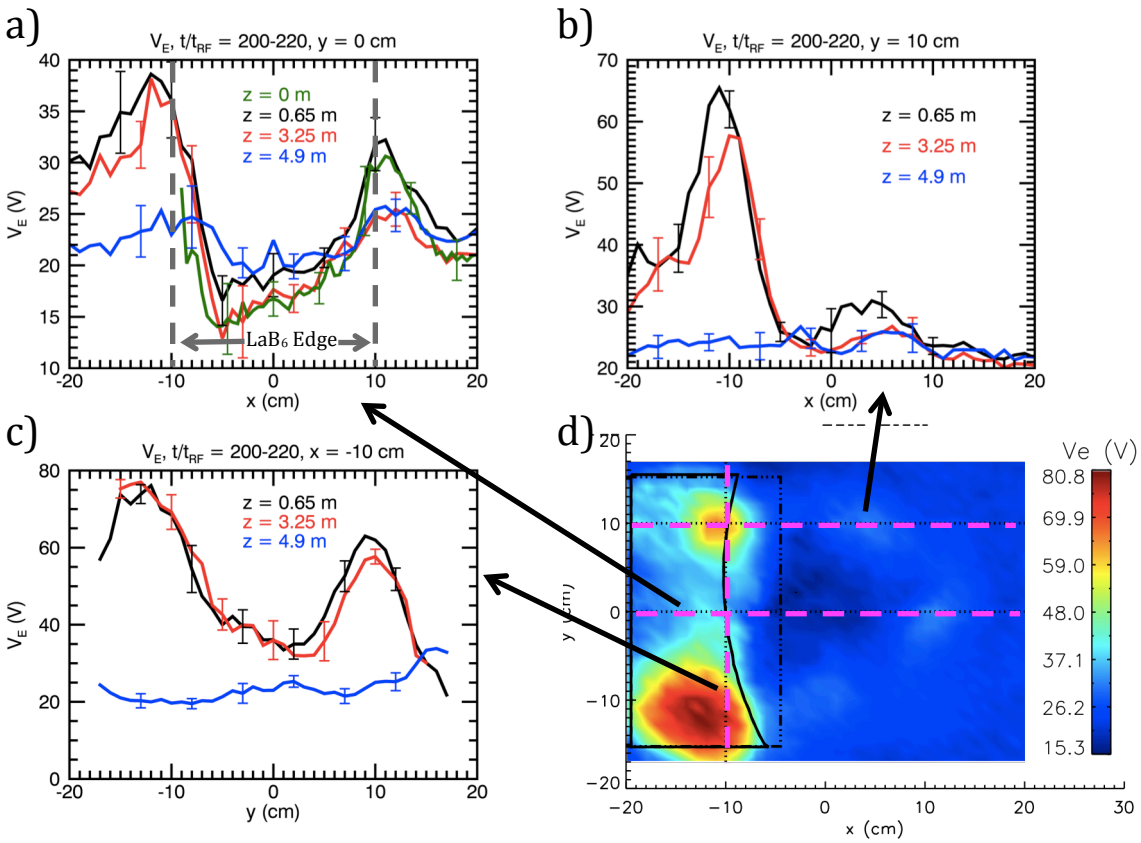

Figure 4.6: $V_{e,DC}$ measured at z = 0, 0.65, 3.25, and 4.9 m and time-averaged over $200 \leq \frac{t}{t_{RF}} \leq 220$. Measurements at z = 0, 0.65, and 3.25 m are axially between the antenna and the limiter located at z = 3.25 m. The measurements at z = 4.9 m are between the limiter and LAPD's BaO plasma source. The $V_{e,DC}$ spatial profile (shown in figure 4.4) exists only in the private SOL between the antenna and the limiter. a) – b)$V_{e,DC}$ vs. x at y = 0 and y = 10 cm, respectively for several axial locations. The blue curve deviates from the other curves starting near x = -4.5 cm. c) $V_{e,DC}$ profiles measured at x = -10 cm. The blue curve bears no resemblance to the red and black curves, as expected because the $V_{e,DC}$ spatial profile exists only in the private SOL between the antenna and limiter. d) A color plot of $V_{e,DC}$ at z = 65 cm, with dashed lines for reference to parts a)-c).

represent measurements taken at z = 4.9 m, which is not in the private SOL formed by the antenna and the limiters. Large rectified potentials are not expected to exist here, and figure 4.6

confirms this suspicion. The potential rectification pattern in fig. 4.6 d) is local to between the antenna and the limiter only.

Figure 4.6 illustrates that the largest enhancement to $V_{p,DC}$ is confined to the axial region between the limiter and the antenna, z = 3.6 m and 0 m, respectively. Removing the limiters from the plasma and comparing the $V_{e,DC}$ profiles between the two cases (i.e. limiters present and limiters removed) further exhibits their effect. A color map of $V_{e,DC}$ measured at z = 3.25 m with the limiters removed (present) is shown in figure 4.7 a) (figure 4.6 b)). The $V_{e,DC}$ patterns are quite different between the two figures. Figure 4.7 a) shows a more uniform $V_{e,DC}$ profile when the limiters are removed from the plasma than figure 4.7 b). The presumed reason for this potential pattern is that with the limiters removed, there is nothing preventing a direct connection between the antenna and the LAPD plasma sources' anodes through the plasma. This means that any large increase in the value of $V_{e,DC}$ at one location biases the potential at that x-y location for all axial locations, consistent with the data shown in figures 4.6. This increased potential then biases the anodes' potentials. Because the anodes are electrically conducting, they are able to set the potential across the magnetic field, so if their potential increases, $V_{e,DC}$ across the plasma column will increase. Both anodes' potentials increased by 60 V with the limiters removed; with both limiters in the plasma, the anodes' potentials increased by only 10 V. Only by having the limiters inserted in the plasma is the $V_{e,DC}$ pattern in figure 4.7 b) observable. The influence of the limiter location, both axially and radially, on the $V_{e,DC}$ profiles has not yet been explored experimentally, and is recommended for future experiments.

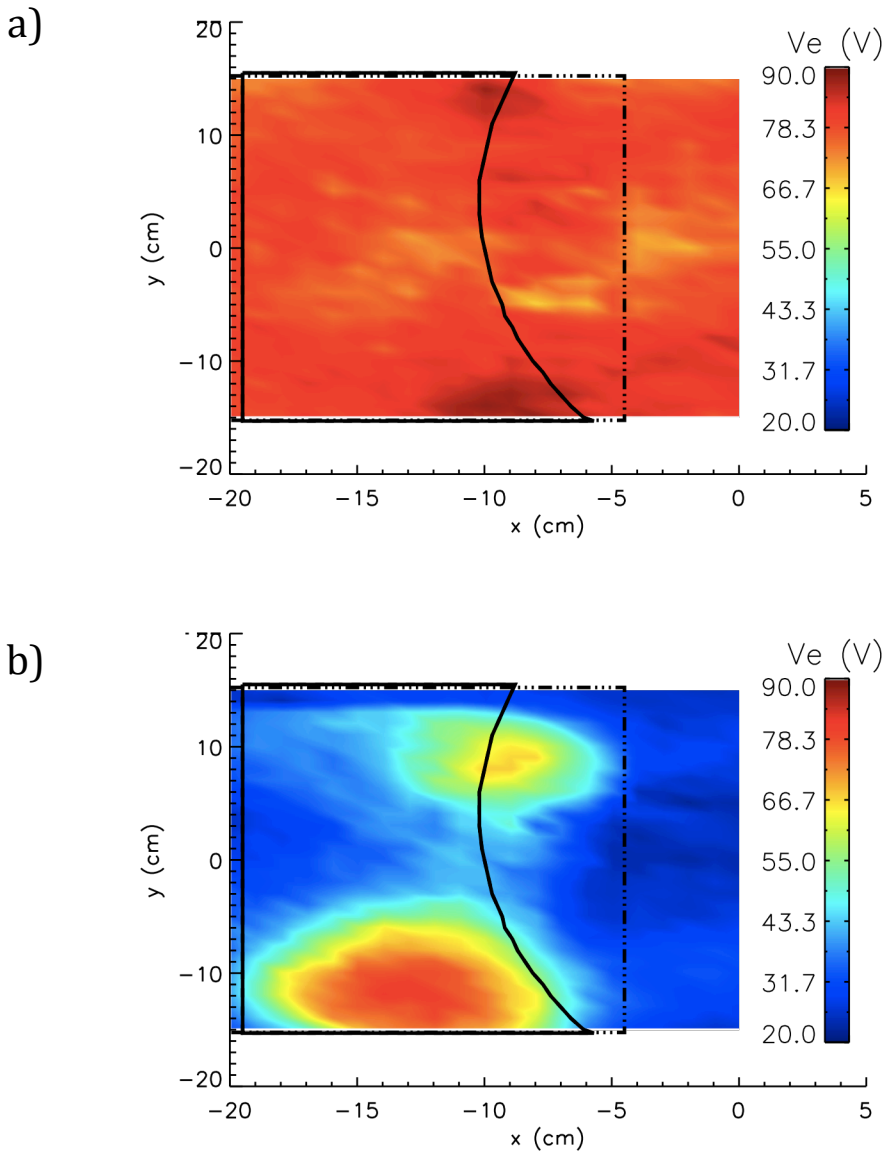

Figure 4.7: a) $V_{e,DC}$ profile measured at z = 3.25 m and averaged over the time interval $200 \leq \frac{t}{t_{RF}} \leq 220$ when the limiters are fully retracted from the plasma. b) $V_{e,DC}$ profile measured at the same location and averaged over the same time period when the limiters are present. The color bars are the same for both figures.

4.2 Relevant RF Sheath Theory

4.2.1 1-D Low Frequency RF Sheath Theory

A low frequency RF sheath model is introduced in order to obtain a point of comparison for LAPD results. The presence of RF potential oscillations between a plasma and a confining boundary have the ability to significantly alter the ion dynamics in the sheath region. These dynamics become much different from their behavior in DC sheaths. An important parameter determining the behavior of an RF sheath is the ratio of the ion transit time through the sheath to the RF period, $t_{RF}/t_{sh} = \omega_{RF}/\omega_{sh}$, where t_{RF} is the RF period and t_{sh} is the ion transit time through the sheath, and ω_{RF} and ω_{sh} are their respective angular frequencies. For $t_{RF}/t_{sh} \gg 1$, an ion traversing the sheath does not experience a significant change during the RF cycle. Thus, the phase of the RF at which it enters the sheath determines its dynamics, and the system behaves as an ensemble of DC sheaths with ions entering them, each representing a different phase of the RF. In contrast, when $t_{RF}/t_{sh} \ll 1$, an ion traversing the sheath experiences a significant number of RF periods during its trajectory. This may be modeled as a single, time-averaged sheath. In order to procede with analysis of RF sheath phenomena, it is important to understand the regime of this experiment. As is often the case in theoretical plasma physics (and probably physics in general), much less work has been performed on understanding the intermediate frequency regime where $t_{RF}/t_{sh} \approx 1$, where sheath impedance has comparable real and imaginary components. The nature of the sheath impedance is calculated by estimating the ratios of conduction current density and displacement current density through the sheath [24]. When $t_{RF}/t_{sh} \ll 1$ the displacement current is much larger than the conduction current, and the sheath impedance is mostly capacitive. On the other hand, when $t_{RF}/t_{sh} \gg 1$ the conduction current is

much larger than the displacement current, and the sheath impedance is mostly resistive. In the intermediate regime the IEDs are bimodal and the sheath impedance is a mix of comparably large resistive and capacitive components, and the phase at which the ion enters the sheath is important. Recent experimental [26-28] and simulation [25] efforts have been aimed at understanding this regime.

In order to determine the nature of the RF sheath, it is important to define the sheath transit time. The following analysis is that given in [24]. The first step is to calculate the sheath thickness assuming a high voltage, collisionless Child-Langmuir sheath. The assumed spatial scalings are $s \ll \lambda_i, L$, where $s, \lambda_i, and\ L$ are the sheath thickness, the ion mean free path, and the system size, respectively. A Child-Langmuir sheath differs from a Debye sheath due to the presence of a high voltage DC bias, $|V_0| \gg T_e/e$, driving the sheath potential, where V_0 is the bias existing between the bulk plasma and the boundary. In the Child-Langmuir sheath, the bias is significant enough to repel all plasma electrons and draw ion saturation current from the plasma. In contrast, a Debye sheath is the natural result of a bounded plasma consisting of electrons and positive ions and usually refers to a surface drawing no net current from the plasma. The electrons are the more mobile species and first establish the sheath by being lost to the confining vessel walls. The Debye sheath potential drop to an electrically floating surface is on the order of $\Delta V_{sh} = V_{p,DC} - V_{f,DC} \approx 4\ T_e/e$, for a Helium plasma. The sheath thickness was estimated in an unbiased etch tool to be on the order of $s \approx 10\lambda_{De}$ [80], where s is the sheath thickness, and λ_{De} is the electron Debye length, defined as,

$$\lambda_{De} = \sqrt{\frac{\epsilon_0 T_e}{n_e e^2}}, \tag{4.2}$$

The sheath thickness was estimated based on where the ion fluid satisfied the Bohm criterion. The Child-Langmuir sheath width, on the other hand, scales as,

$$s = \frac{\sqrt{2}}{3}\left(\frac{2qV_0}{T_e}\right)^{3/4}\lambda_{De}, \tag{4.3}$$

where in the analysis it is assumed that the energy the ion gains traversing the sheath is much larger than the initial energy it has upon entering the sheath, in other words, $\frac{1}{2}m_i c_s^2 \ll -q_i V_0$ and that the ion temperature is negligible compared to the electron temperature. For typical LAPD SOL parameters in this experiment, $V_0 \approx 100\,V, T_e \approx 3\,eV$, and $\lambda_{De} \approx 20\,\mu m$ the expected sheath thickness is $220\,\mu m$ based on equation 4.3.

Having obtained a sheath width for the Child-Langmuir sheath, one can then obtain the ion transit time through the sheath, which is,

$$t_{sh} = 3s\left(\frac{m_i}{2qV_0}\right)^{1/2}, \tag{4.4}$$

This expression once again assumes that the initial ion energy into the sheath is much less than the energy gained traversing the sheath. In the case of an RF sheath, the location of the sheath edge is changing with RF phase, as is the potential drop through the sheath. In this case, the expressions used in the sheath transit times are their time-averaged values, and s and V_0 are replaced by their time-averaged values, $\bar{s}$ and $\overline{V_0}$, respectively. Note that equation 4.4 blows up as V_0 approaches 0 because the additional presence of the Debye sheath was neglected in the derivation. Now it is possible to define the ratio,

$$t_{RF}/t_{sh} = 2\pi/\omega_{RF} \cdot \left(2q\overline{V_0}/M\right)^{\frac{1}{2}}\left(1/3\bar{s}\right), \tag{4.5}$$

and substituting equation 4.3 into equation 4.5,

$$t_{RF}/t_{sh} = \omega_{pi}/\omega_{RF} \cdot \left(2T_e/q\overline{V}_0\right)^{\frac{1}{4}}\pi, \quad (4.6)$$

Inserting LAPD parameters measured/used during this thesis experiment (T_e ~ 1 eV, n_e~ 10^{11} cm^{-3}, $\overline{V}_0$~100 V, and f_{RF}= 2.379 MHz in a Helium plasma) into equation 4.6, we find $t_{RF}/t_{sh} \approx$ 16.4. This means that an ion traversing the sheath experiences relatively little change in the accelerating potential during the RF cycle during its trajectory through the sheath and the low frequency RF sheath limit can be used.

In low-frequency analysis of RF sheaths, one can assume a sinusoidal RF bias applied between a plasma and a PFC. It does not matter which side has the bias applied. In this case, the instantaneous plasma current to a PFC, I_{PFC}, can be described by a modified form of equation 3.3 [10, 22, 59, 81]

$$I_{PFC}(V,t) = I_{esat}e^{\frac{e\left(V_{PFC,DC}-V_{p,DC}+V_{RF}\cdot\cos(\omega_{RF}\cdot t)\right)}{k_B T_e}} - I_{isat}, \quad (4.7)$$

Note that implicit in this low frequency analysis is the assumption that the current through the sheath is particle current rather than displacement current. This means the sheath is resistive rather than capacitive, consistent with parallel plate capacitor sheath estimates for RF sheaths [24]. Langmuir probe analysis electrical current signage conventions are invoked in equations 4.7 and the following analysis, in which current due to positive charge carriers is negative. Equation 4.7 is valid within the voltage limits for which $\left|V_{PFC,DC} - V_{p,DC}\right| \geq V_{RF}$. Within this voltage limit, the PFC may collect I_{esat} for only a single instant during the RF cycle, when $\omega_{RF}t = 2\pi n$, where n is an integer. In the situation where $\left|V_{PFC,DC} - V_{p,DC}\right| < V_{RF}$, equation 4.7 becomes, $I_{PFC}(V,t) = I_{esat}$, at times for which $V_{PFC,DC} - V_{p,DC} + V_{RF}\cdot\cos(\omega_{RF}\cdot t) > 0$. In the limit $I_{PFC}(V,t) = -I_{isat}$, $V_{PFC,DC} - V_{p,DC}$ goes to infinity, signifying that all electrons in the

distribution function are prevented from contributing to I_{PFC}. A common approach to the problem of collected current in a time-varying system is to find the average value of the current through the sheath over one RF period. In normalized units equation 4.7 becomes,

$$\langle \frac{I_{PFC}(V,t)}{I_{isat}} \rangle = (v_{te}/0.61 \cdot c_s) e^{\frac{e(\Delta V)}{k_B T_e}} \langle e^{\frac{e(V_{RF} \cdot \cos(\omega_{RF} \cdot t))}{k_B T_e}} \rangle - 1, \tag{4.8}$$

where the quantities in brackets are time-averaged quantities and ΔV is the DC-rectified potential difference between the PFC potential and the plasma potential, $V_{PFC,DC} - V_{p,DC}$. Normalization to I_{isat} is done because, in the LAPD, V_p is a factor 2-3 times T_e greater than the grounded limiter potential, and electron current to the limiter is greatly reduced from I_{esat}. To continue with the derivation, one uses [82]:

$$I_0(z) = \frac{1}{\pi} \int_0^{\pi} e^{\pm z cos(\theta)} d\theta, \tag{4.9}$$

where $I_0(z)$ is the modified Bessel function of the first kind of order 0. Then equation 4.8 becomes,

$$\langle \frac{I_{PFC}(V,t)}{I_{isat}} \rangle = (v_{te}/0.61 \cdot c_s) e^{\frac{e(\Delta V)}{k_B T_e}} I_0 \left(\frac{eV_{RF}}{k_B T_e} \right) - 1, \tag{4.10}$$

In the limit of $eV_{RF} \gg k_B T_e$,

$$\langle \frac{I_{PFC}(V,t)}{I_{isat}} \rangle = (v_{te}/0.61 \cdot c_s) e^{\frac{e(\Delta V)}{k_B T_e}} \frac{1}{\sqrt{2\pi \left(\frac{eV_{RF}}{k_B T_e} \right)}} e^{\left(\frac{eV_{RF}}{k_B T_e} \right)} - 1, \tag{4.11}$$

A common approximation in the ICRF literature [15] is that the boundary is an electrically floating surface ($\langle \frac{I_{PFC}(V,t)}{I_{isat}} \rangle = 0$), in which case equation 4.11 becomes,

$$\frac{-e\Delta V}{k_B T_e} = \ln \left(\frac{v_{te}}{0.61 \cdot c_s} \right) + \frac{eV_{RF}}{k_B T_e} - \frac{1}{2} ln \left(2\pi \frac{eV_{RF}}{k_B T_e} \right), \tag{4.12}$$

where the DC rectified sheath potential voltage is now on the left hand side of the equation. The first term on the right hand side of the equation is the Debye sheath potential (recall equation 3.4), and the second and third terms, which contain V_{RF}, represent the RF contribution to the sheath potential. In the limit of $eV_{RF} \gg k_B T_e$, the term linear in V_{RF} is the dominant contributor to the low frequency RF sheath potential. The floating boundary assumption is taken assuming that the plasma cannot supply current to the boundary and will therefore, in steady-state, supply zero time-averaged current.

Figure 4.8 shows how the low frequency RF sheath potential, ΔV, scales with RF potential oscillations, V_{RF}. As can be seen in the figure, for RF potential oscillations above 3Te, the scaling becomes linear with applied RF potential. In addition, drawing net current from the plasma merely displaces the curve in the y-direction in figure 4.8, so the ΔV vs. V_{RF} trend is general, regardless of current drawn from the plasma, within the limits of this discussion.

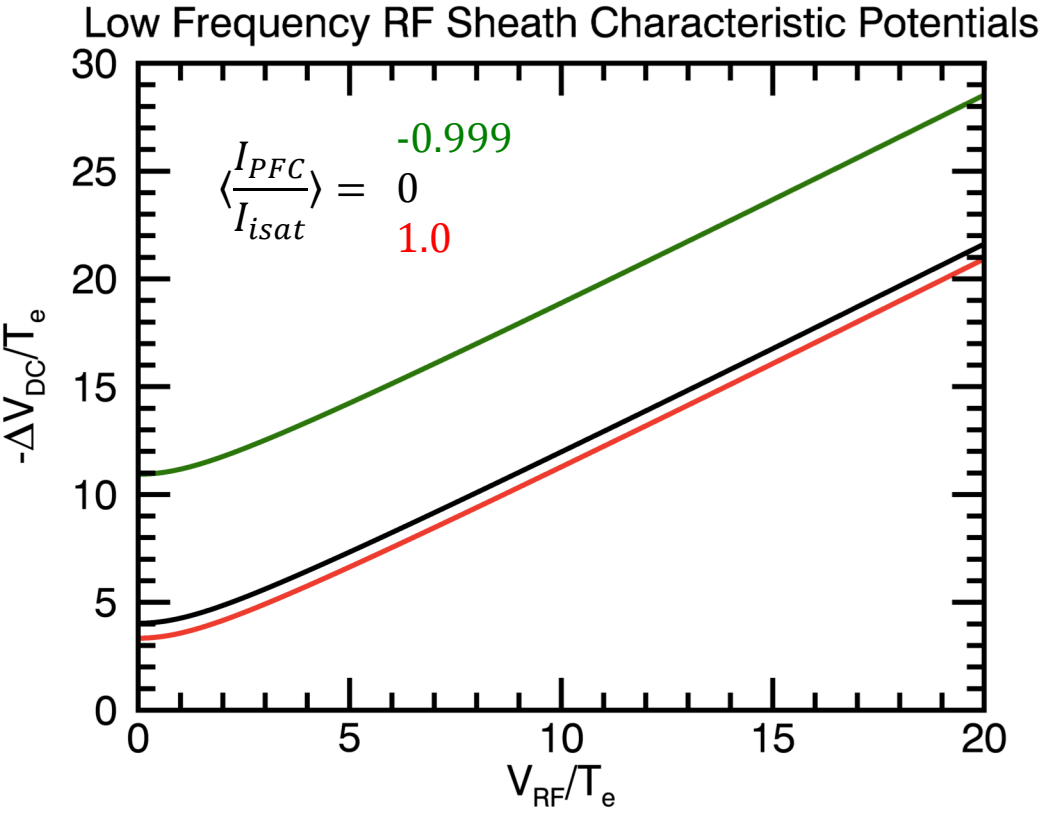

Figure 4.8: 1-D low frequency RF sheath voltage drop scaling with RF potential, from equation 4.10. Green, black, and red curves represent surfaces biased to draw $\sim I_{isat}$, 0, and $-I_{isat}$ current from the plasma, respectively.

4.2.2 RF Sheaths in tokamaks

The previous analysis was performed assuming no background magnetic field, $\boldsymbol{B}_0$, is present. In the LAPD and tokamak environments, however, a $\boldsymbol{B}_0$ does exist. In the event that $\boldsymbol{B}_0$ is not of grazing incidence, $\alpha > \sin^{-1}\left(\sqrt{\frac{m_e}{m_i}}\right)$, where α is the angle between the magnetic field and the PFC tangent, as shown in figure 4.7, the sheath can be treated approximately as in the unmagnetized case [83, 84] for magnetized plasma along background magnetic field lines. This

approach is appropriate in tokamaks for antenna components, with a typical pitch angle of up to

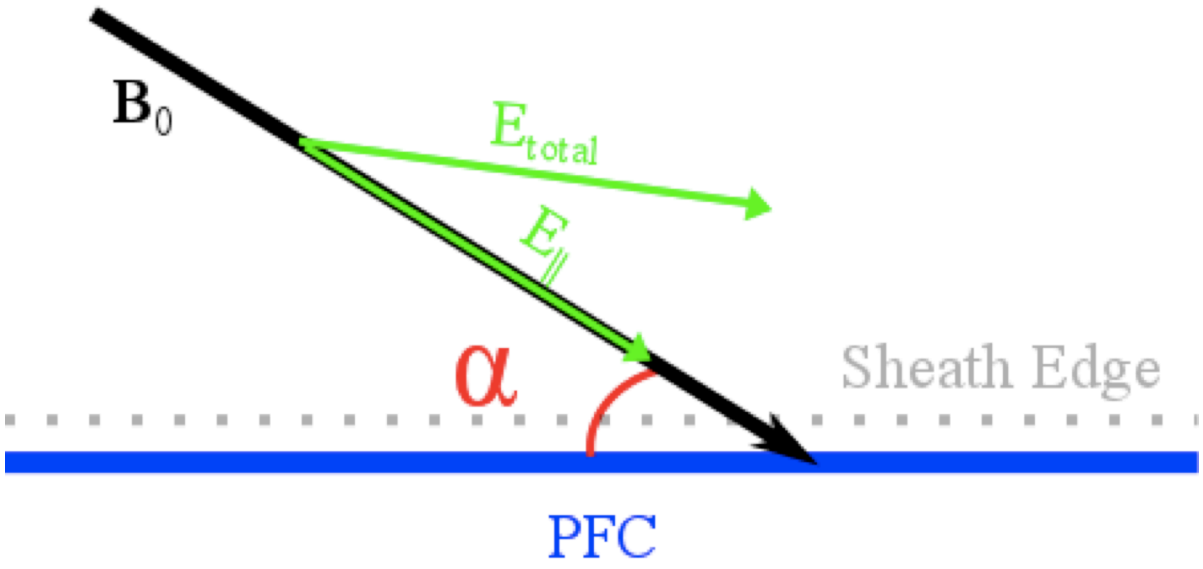

Figure 4.9: The geometry of the problem of RF sheaths in a plasma with a background magnetic field, $\boldsymbol{B}_0$. $\boldsymbol{B}_0$ intersects the PFC surface at an angle α. An electric field parallel to $\boldsymbol{B}_0$, $\boldsymbol{E}_\parallel$, accelerates particles into the PFC and creates the oscillating RF voltages, V_{RF} that form the RF sheath.

13 degrees with the surface normal, however, it may not be appropriate for divertor tiles where the magnetic fields make a grazing angle with the tiles. The common ansatz [9] is that an RF electric field parallel to $\boldsymbol{B}_0$, $\boldsymbol{E}_\parallel$, drives the RF sheath potential,

$$V_{RF} = \int \boldsymbol{E}_\parallel \cdot \boldsymbol{dl} \qquad (4.13)$$

Where V_{RF} is the oscillating potential, $\boldsymbol{dl}$, is the differential length vector, and the integral bounds are momentarily undefined. The original application of equation 4.13 was to describe accelerating RF sheaths that form between adjacent Faraday screen elements [9] as a result of sinusoidal magnetic flux through the closed-loop formed by faraday screen rods and their supports. In this instance the bounds of the integral in equation 4.13 are the locations of the Faraday screen surfaces. In general this integral should be made over definite bounds, but in

practice the bounds are limited by the spatial extent of the calculation area [85, 34]. Equation 4.13 has since been more generally applied to studies of wave-induced sheaths [85, 86] and to sheaths forming on antenna side limiters [87]. Though equation 4.13 is a one-dimensional description of RF sheath-forming potentials, analytical efforts are being made towards more sophisticated two-dimensional descriptions of RF sheath formation by use of a plasmas Green's function [88].

The value of $\boldsymbol{E}_{\parallel}$ is essentially the only term in equation 4.13. Thus, tokamak antenna design efforts concentrate on either minimizing $\boldsymbol{E}_{\parallel}$ or the integration result of equation 4.13. This minimization is performed on both the launched wave fields [85, 34] and on the fields at the antenna limiter surfaces [87]. These efforts have produced mixed results in minimizing RF enhanced DC potentials and deleterious RF-sheath effects in tokamaks [18, 7, 89]. Ref. [18] describes an experiment performed in the Tore Supra tokamak utilizing a 2-strap antenna designed to minimize $\int \boldsymbol{E}_{\parallel} \cdot \boldsymbol{dl}$ (and allegedly RF sheath voltages) by diverting RF current paths in the antenna box enclosure. However, floating potential measurements showed high floating potentials (up to 170 V) along field lines connected to the top and bottom of the antenna, as in figure 1.2 a). In the same experiment, IR camera measurements showed that the areas of the antenna that experienced the most significant heating during the RF pulse was at the top and bottom. In ref. [7], a novel field-aligned (FA) antenna was installed in the Alcator C-mod tokamak that was designed to reduce launched $V_{RF} = \int \boldsymbol{E}_{\parallel} \cdot \boldsymbol{dl}$ [85] compared to the standard toroidally aligned (TA) antenna. Results obtained with an emissive probe showed that rectified potentials due to the TA and FA antennas were quantitatively similar over a range of antenna powers 200 kW – 1.5 MW, but that the FA antenna reduced the presence of core Mo impurities. Additionally, ref. [89] describes a novel three-strap antenna experiment performed in the

ASDEX-U tokamak. Experiments show that when the strap phasing is [0, pi, 0] and the current in the middle strap is twice the current in the other two straps that the tungsten sputtering is reduced by a factor of 2 or higher than a typical 2 strap antenna. The suspected reason for this was that the magnitude and phasing of the three strap antenna was effectively minimizing RF image currents in the antenna box enclosure, and was thus minimizing the launched $\boldsymbol{E}_{\|}$, thought to drive the sheath potential, as opposed to $\int \boldsymbol{E}_{\|} \cdot \boldsymbol{dl}$. Experimental validation that this was effective in minimizing V_{RF} is only indirect, as seen in the reduction in tungsten sputtering.

In summary, equation 4.12 gives a dimensionless power scaling for low frequency RF sheaths. This is based on a one-dimensional treatment of the RF sheath. The spatial location of the enhanced potentials can be determined from the location of large $\boldsymbol{E}_{\|}$ forming at the antenna structure. This is often done by finite-element modeling of the antenna using codes such as TOPICA [90]. The result is a map of $\boldsymbol{E}_{\|}$ at the antenna, and is merely qualitative, giving the locations of the RF sheaths, rather than the value of them, due to the fact that the integration length in equation 4.13 is often ill defined. Attempts at converting the $\boldsymbol{E}_{\|}$ resulting from antenna simulations into RF sheath potentials is an ongoing effort [87].

4.3 Comparison of Results 1-D RF-sheath model

The discussion will now focus on the region at the bottom of the antenna in figure 4.4 where the rectified potentials are the highest. In order to determine the effect of heating, the time evolution of the ion saturation current is plotted in figure 4.10 a), in the middle of this region of high RF rectified potential. As can be seen in the figure, I_{isat} at x = y = -12 cm increases during the RF pulse by a factor of 2 within the first 100 cycles, and slowly decays to less than its pre-RF value. At (x,y) = (-10 cm, -12 cm) there is no discernible increase in I_{isat} during the RF pulse.

From these plots, it is determined that the effect of the RF on the electron temperature is to increase it by no more than a factor of 4 at x = y= -12 cm, with little to no change in T_e at (x,y) = (-10 cm, -12 cm). Interestingly, 100 cycles after the RF pulse is over the value of the I_{isat} sharply increases at both locations. This will be discussed later. For now the focus is on the potentials during the RF pulse. Figure 4.10 b) now shows how I_{isat} changes at y = -12 cm for x between -20 cm and 0 cm and for various times during the RF pulse. As can be seen in this figure, for x < - 15 cm the value of I_{isat} changes dramatically over time, whereas for x > -15 cm, changes in T_e are not expected to play a large role in determining the cause of RF potential enhancements, though they may influence the plasma potential for x < - 15 cm.

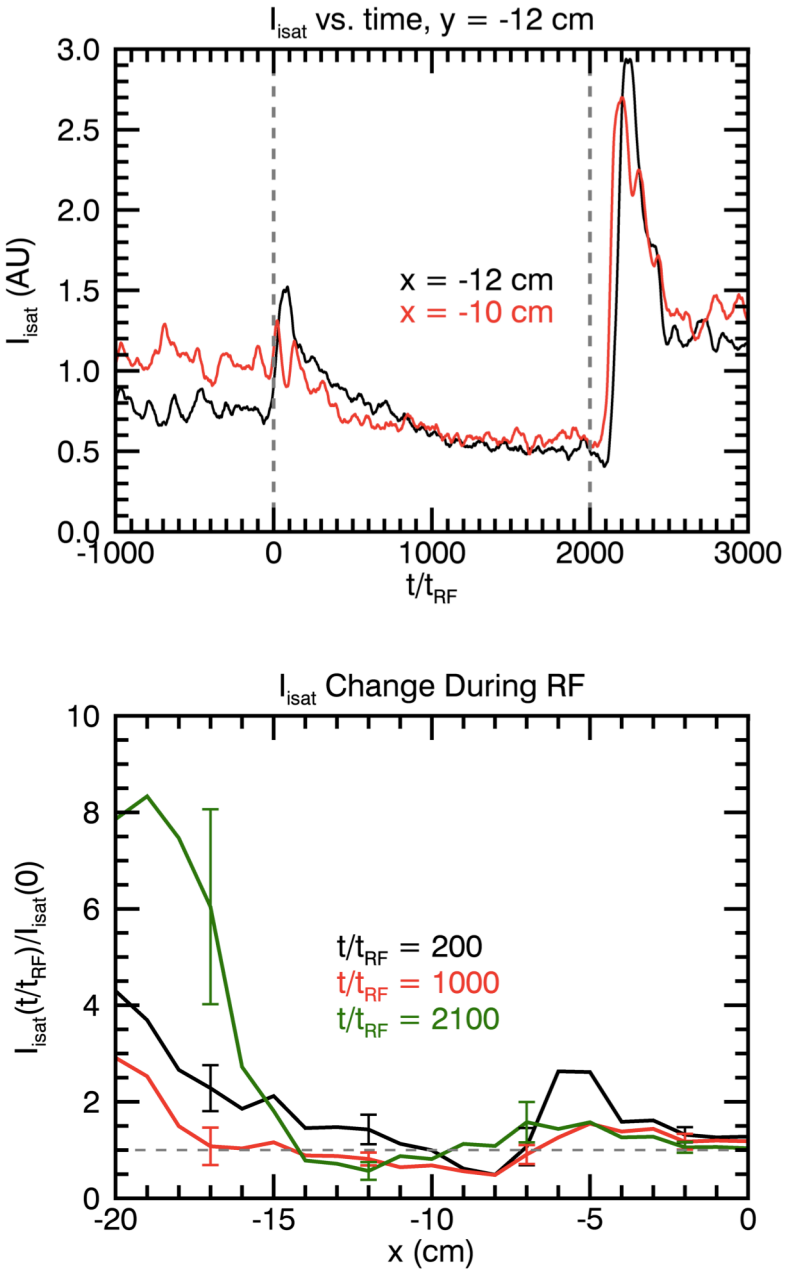

Figure 4.10: I_{isat} vs. time and space. a) I_{isat} vs. time at (x,y,z) = (-10 or -12 cm, -12 cm, 65 cm). Even if all of the increase in $I_{isat} \propto n_e\sqrt{T_e}$ during the RF pulse is due to increased T_e, that only amplifies T_e by a factor of 4. b) Normalized I_{isat} vs. position at (y,z) = (-12 cm, 65 cm). For the most part I_{isat} changes insignificantly during the RF pulse. For $x \leq -15$, I_{isat} increases significantly due to the applied RF. It is suspected that this is due to a combination of increased T_e and n_e.

An RF power scan was performed to determine the effect of the RF enhancement of the plasma potential. The emissive probe is able to reliably capture potential oscillations up to 10 MHz [69]. Unfortunately for comparison to equation 4.10, the oscillating RF potentials appear to be electrostatically screened by the plasma, meaning the majority of the sheath oscillation occurs very close to the antenna. This has been reported in a commercial plasma etch tool, where the geometry is different and there is no $\mathbf{B}_0$; the RF bias applied to the wafer is observed to no longer influence the ion energy distribution functions 1 cm above the wafer [91]. This is explained as the bias voltage not penetrating into the plasma and is essentially the size of the RF sheath and presheath. To illustrate this electrostatic screening, the RF oscillation amplitudes of the plasma potential are plotted in a color map across the plasma column in figure 4.11. Data in figure 4.11 were acquired at z = 65 cm. This figure plots the maximum oscillation amplitude of the RF plasma potential. It is clear that there are dark spots in the color map, corresponding to low RF plasma potential oscillations, at the top and bottom of the antenna. These locations correspond to the locations where the DC component of the plasma potential is the highest.

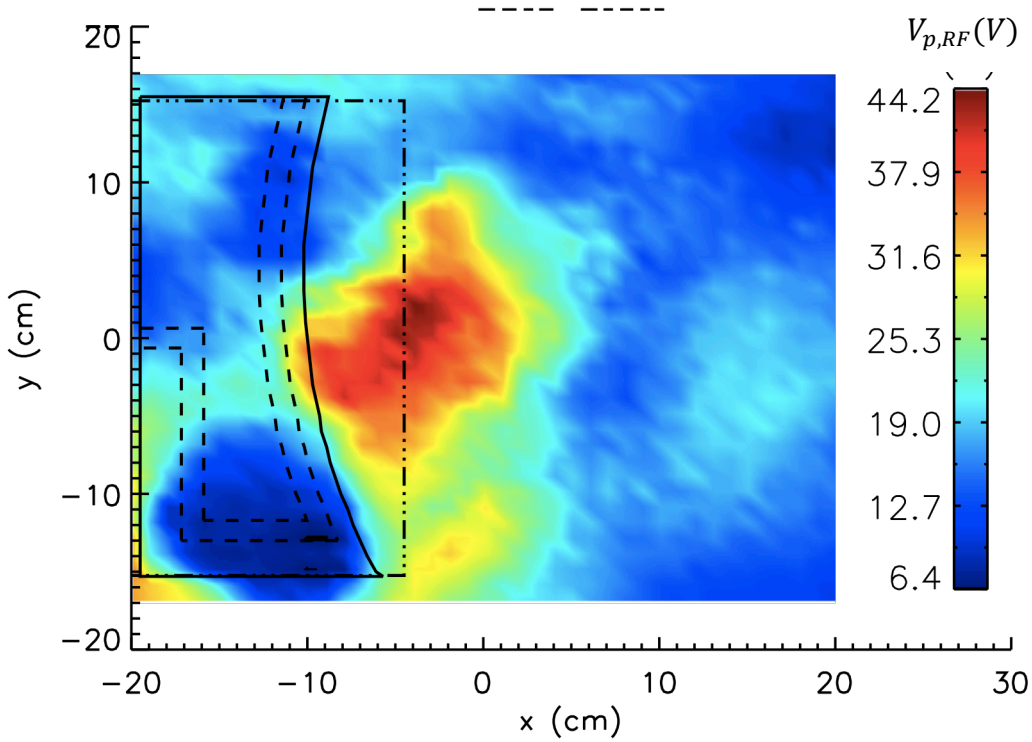

Figure 4.11: Color map of $V_{p,RF}$. The color map shows the maximum value of $V_{p,RF}$ during the RF pulse. The location of the antenna box enclosure(—), the current strap internal to the box enclosure (--), and the limiter located at z = 3.6 m. (··· —) are marked for reference. The color map is the peak value of $V_{p,RF}$ over the entire RF discharge. It is largest in front of the antenna and at the limiter edge. At the top and bottom of the antenna the RF potential oscillations are much smaller than elsewhere. The color map in this figure is different from the color map in figure 4.4. In this figure the lowest potentials, $V_{p,RF}$, are located at the top and bottom of the antenna, whereas in figure 4.4 the highest potentials, $V_{p,DC}$, is at the top and bottom of the antenna.

Since the measured $V_{e,RF}$ is not useful for substitution into equation 4.10, a proxy for it must be used. In this experiment, the natural proxy is the current in the antenna strap, with the assumption that $V_{e,RF} = V_{p,RF} \propto I_{antenna}$. The result of the power scan is shown in figure 4.12 at (x,y) = (-10 cm,-12 cm) for $200 \leq \frac{t}{t_{RF}} \leq 1900$, where the $V_{p,DC}$ is plotted vs. the RMS antenna current. This timeframe is chosen because both the antenna current and the plasma potential

reach near steady state values in this window. As the antenna current is increased, the plasma potential rectification linearly responds at high power RF operation. Future theoretical studies should explain this linear behavior. The *magnitude* of the impedance measured across the antenna coaxial input was 4.6 Ω, measured by the ratio of the RMS voltage across the antenna over the RMS current in the antenna. Thus, at the highest antenna powers, with 560 A RMS in the antenna, the voltage on the antenna was close to 2600 V RMS. Also shown in figure 4.12 are two curve fits to the data; the red line is a fit using equation 4.10, and the green line is the result of a linear fit to the data. T_e used in the red curve is 5.5 eV, within experimental error of the value measured at this location. The fitted curve using equation 4.10 lines up with the data well for all antenna powers. The linear fit to the data aligns well with the data for non-zero antenna current, indicating that the rectified plasma potential is linear in antenna current. In figure 4.10, the DC plasma potential for various antenna currents changes by a factor of ~ 6, from 12 V to 75 V when the RF is present. This indicates that if the potential rectification were a Debye sheath it would be due to electron temperatures greater than 20 eV, which have never been reported in the LAPD. Both fits plotted in figure 4.12 provide good approximations to the measurements, however, it should be noted that the error bars in the plasma potential are large. The significant result of figure 4.12 is that the plasma potential rectification is linear with antenna current. It is not surprising that equation 4.10 provides a good fit to the measured data, because for $V_{RF} \gg T_e$ equation 4.10 becomes approximately linear in the RF oscillating potential. To more rigorously apply 1-D RF sheath theory, many similar measurements must be made in the $0 < I_{antenna} < 100\ A$ range of antenna operation.

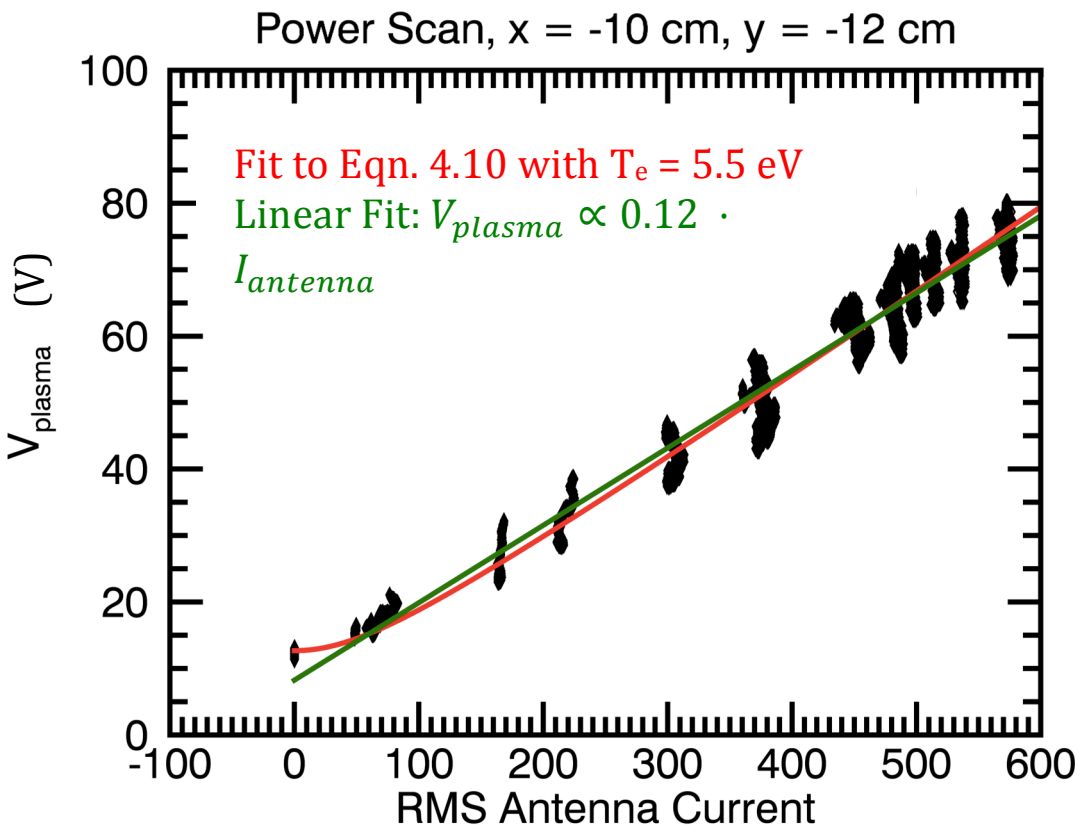

Figure 4.12: $V_{p,DC}$ vs. RMS antenna current at (x,y,z) = (-10 cm, -12 cm, 65 cm). Data are plotted for $200 \leq \frac{t}{t_{RF}} \leq 1900$. Black diamonds represent values averaged over one RF cycle. The red curve is a fit of equation 4.10 to the data, and the green curve is a linear fit to the data.

A nonlinearity in the RF potential rectification is easily observed in figure 4.13, which plots the rectified component of $V_{p,DC}$, $\Delta V_{p,DC} = V_{p,DC}\left(\frac{t}{t_{RF}}\right) - V_{p,DC}(0)$, divided by the RMS antenna current. The figure shows that for low RMS current in the antenna, the rectified potential increases less rapidly with antenna current than for high RMS currents in the antenna. This is particularly apparent for x < -8 cm.

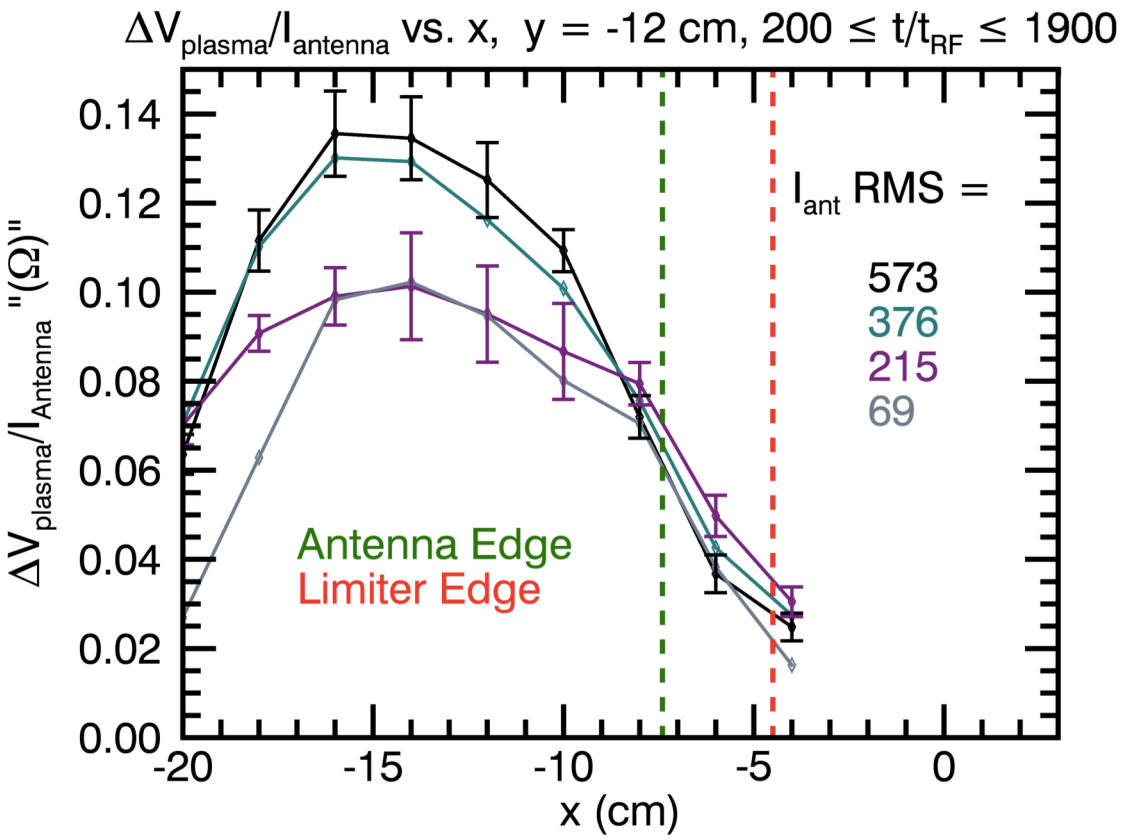

Figure 4.13: Scaled $V_{p,DC}$ vs. position for y = -12 cm. Data plotted are averaged over $200 \leq \frac{t}{t_{RF}} \leq 1900$. The effect of the RF rectification lies spatially between the limiter and the antenna. For low power operation, the scaling is different than that for higher power antenna operation. Above a threshold power, the scaling is the same regardless of antenna power.

4.4 Rectified Potential Ring Down

Nowhere in equations 4.8 – 4.12 is there any time dependence other than an integration over an RF period. This is due to the resistive, rather than capacitive, nature of the low frequency RF sheath. Because the ions respond instantaneously to the impressed RF potentials, the RF rectification should immediately respond to changes in the RF bias voltage. This is observed during the initiation of the RF pulse. As the RF current in the antenna increases, the rectified

potential instantaneously increases. However, after the antenna is shut-off, the rectified potential remains. Figures 4.14 a) - b). show the timing of this phenomenon. Figure 4.14 a) shows the RMS antenna current between $1900 \leq \frac{t}{t_{RF}} \leq 2200$. As can be seen in the figure, the antenna current has rung-down to less than 10% of its value during the RF pulse 50 RF cycles ($\frac{t}{t_{RF}} = 2050$) after RF shutoff. However, as can be seen in figure 4.14 b), the plasma potential decays much slower. The measurements for figure 4.14 b) were acquired with the emissive probe at z = 65 cm, but are similar to those acquired at z = 3.25 m in that the ring down takes place over the same time range at the same x-y position. The **B**-field magnitude measured at z = 65 cm decreases after the RF pulse at a rate similar to the antenna current. It is thus presumed that the persistence of the DC plasma potential is not a wave-induced phenomenon for waves with strong magnetic fields. This slow ring down behavior is in stark contrast to that exhibited in a previous ICRF experiment on the LAPD in which an un-slotted metal box enclosure was used instead of the current slotted-box with a dielectric. In the previous experiment the plasma potential decreased with the antenna current, rather than continuing to decrease long after it. One may speculate as to why the plasma potential takes so long to decrease to its pre-RF value. It may have to do with the macor dielectric on the interior of the box charges positive during the RF pulse. This seems unlikely because there is no sign of the slots in the box when looking at the results from data planes. If the enhanced potential were due to the macor, one would expect data magnetically aligned with the macor to be different from data magnetically aligned to copper antenna components. In addition, dielectric charging has been observed in smaller plasma chambers where it charged the plasma negatively. Another proposed reason the plasma potential takes so long to decrease is that the flows created by the $\boldsymbol{E}\times\boldsymbol{B_0}$ drifts decrease electron transport to this portion of the plasma. An interesting thing to note is that the I_{isat} measurements show a

large increase after the RF pulse. Here, I_{isat} is used as a proxy for n_e. T_e was measured between $2141 \leq \frac{t}{t_{RF}} \leq 2379$, soon after the RF pulse. Little electron heating was observed with these measurements. This, combined with square root dependence on temperature for ion saturation current is why I_{isat} is treated as a proxy for n_e. Even though the timeframe in figure 4.15 ends at $\frac{t}{t_{RF}} = 2200$, an inspection of figure 4.10a shows that I_{isat} is larger during the swept probe measurements after the RF pulse, indicating that if significant increases in T_e had occurred, they would have been measured. The timing of this increase is in I_{isat} is shown for various x locations at (y,z) = (-12 cm, 65 cm) with an RMS antenna current of 565 A in figure 4.15 a). The figure shows that I_{isat} increases sooner after the RF pulse outside the center of the high plasma potential region, $x \leq -15\ cm$ and $x \geq -10\ cm$. Closer to the center of the region with large increases in plasma potential, $-15\ cm \leq x \leq -10\ cm$, the time it takes for I_{isat} to increase is much longer, up to 100 RF periods. Figure 4.15 b) shows a similar trend for how long it takes $V_{p,DC}$ to decay. $V_{p,DC}$ takes longer to decay in the center of the region of high $V_{p,DC}$, $-15\ cm \leq x \leq -10\ cm$, and shorter outside this region. Thus, at all powers, the RF-enhanced DC plasma potentials must be reducing transport to the regions where the potentials are the highest. This is fairly interesting, given that I_{isat} increases farther in the SOL, $x \leq -15\ cm$, than where the high RF potentials form. The density changes in figure 4.15 a) indicate the presence of strong restoring flows that redistribute the density after the RF pulse. Figure 4.10 a) hints at the presence of these flows during the RF pulse. The flows due to the electrostatic electric field shown in figure 4.4 is the subject of the next chapter.

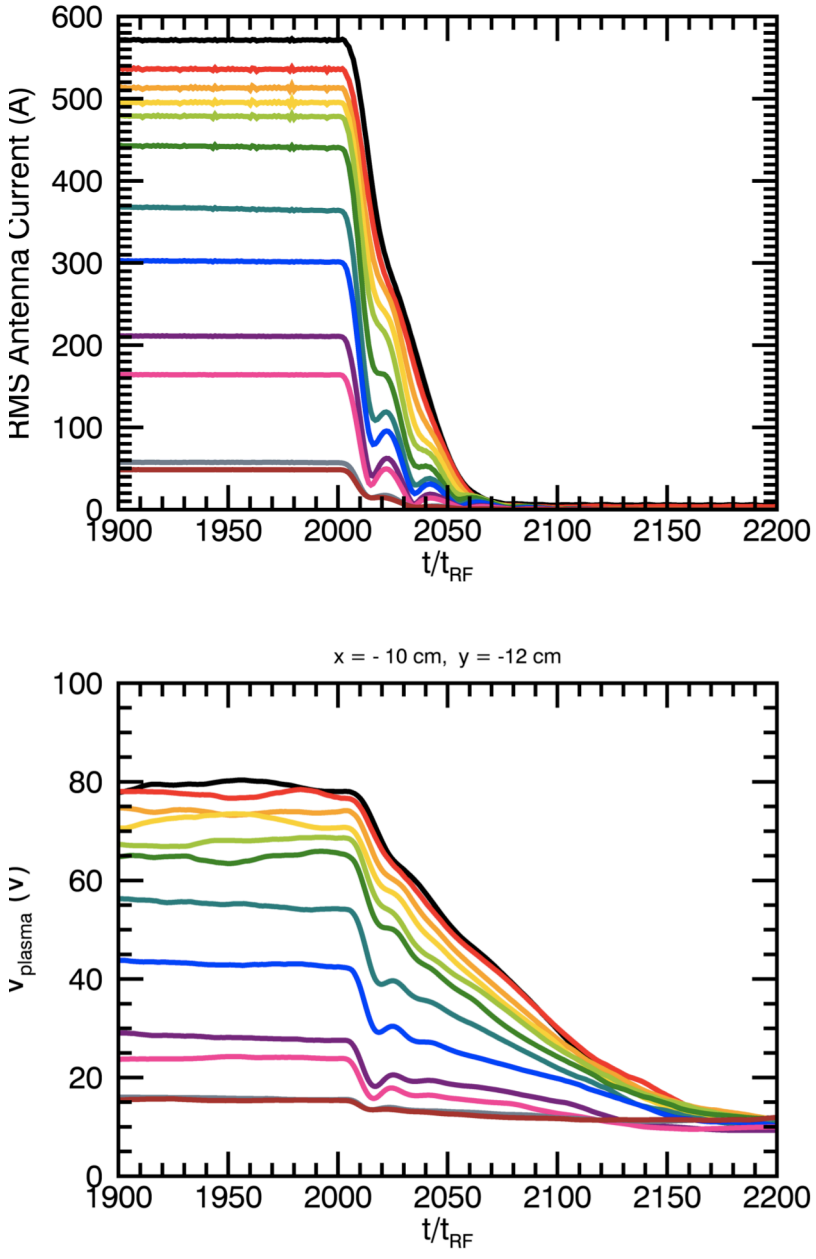

Figure 4.14: Power scan of the ring-down of the antenna current and the rectified potentials. a) RMS antenna current vs. time. b) $V_{p,DC}$ vs time at (x,y,z) = (-10 cm, -12 cm, 65 cm). The fall time of $V_{p,DC}$ is much longer than that of $I_{antenna}$ at all antenna powers.

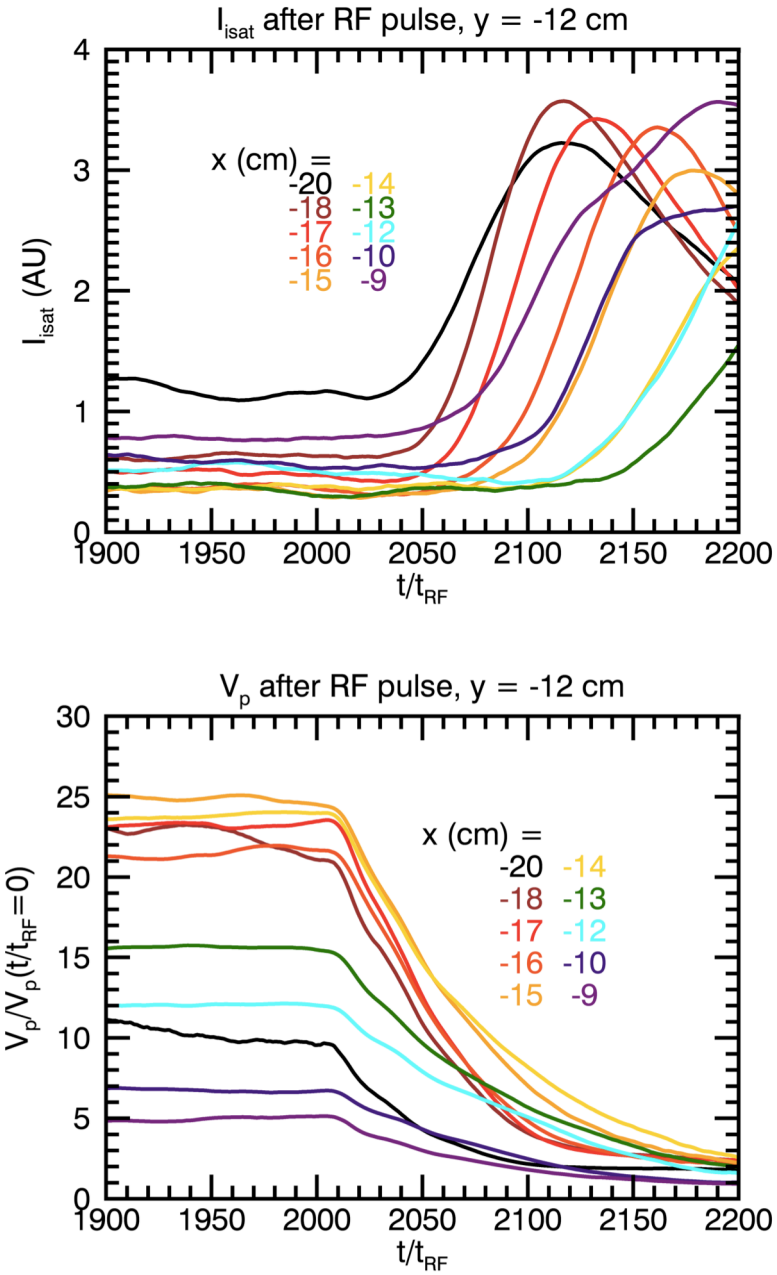

Figure 4.15: I_{isat} and $V_{p,DC}$ profiles after the RF pulse at y = -12 cm, z = 65 cm. a) I_{isat} vs. time. b) $V_{p,DC}$ vs. time at (x,y,z) = (-10 cm, -12 cm, 65 cm). I_{isat} increases sooner for higher values of $|x - x_0|$, where $x_0 = -13\ cm$. Conversely, $V_{p,DC}$ decays faster for higher values of $|x - x_0|$. This indicates the slow $V_{p,DC}$ decay time is related to the density fill-in.

Chapter 5: Properties of RF-Induced Flows

5.1 Properties of RF Induced $\boldsymbol{E}\times\boldsymbol{B_0}$ flows in the SOL

The $V_{p,DC}$ profiles discussed in the previous chapter create electrostatic electric fields, $\boldsymbol{E} = -\boldsymbol{\nabla} V_{p,DC}$, that induce $\boldsymbol{E}\times\boldsymbol{B_0}$ drifts with velocity $v_{\boldsymbol{E}\times\boldsymbol{B_0}} = \frac{\boldsymbol{E}\times\boldsymbol{B_0}}{\boldsymbol{B_0^2}}$. These flows are calculated from the $V_{p,DC}$ measurements made with the emissive probe. A color and vector map of these particle drifts is displayed in figure 5.1. The color bar in figure 5.1 denotes the electrostatic electric field perpendicular to $\boldsymbol{B_0}$, $\boldsymbol{E}_\perp$, in V/cm as well as the flow speed in km/s derived assuming the drift is due to $\boldsymbol{E}\times\boldsymbol{B_0}$. Figure 5.1 shows two distinct regions of high flow velocity, at the top and bottom of the antenna on the edges of where the $V_{p,DC}$ profile during the RF pulse is the highest. The two circular regions of high flow velocity on the top and bottom of the antenna will henceforth be referred to as "convective cells." The convective cells are linked by vertical flows so that the whole flow region resembles two bicycle gears plus their chain. Three additional flow vortices can be seen in the bulk plasma region. Those flows exist before the RF pulse and are a result of the background $\boldsymbol{E}_\perp$ due to the two plasma sources. The RF-induced flows in figure 5.1 are much larger in magnitude than these background flows. Is the $\boldsymbol{E}\times\boldsymbol{B_0}$ flow description appropriate to describe the particle response to the electrostatic electric fields due to the limited spatial region in which they exist? In order to determine this, the non-dimensional length scaling is calculated for the drifts as,

$$\rho_{T_i} \cdot l_{E_\perp}^{-1} \equiv \rho_{T_i} \cdot \left| \frac{d(ln(\boldsymbol{E}_\perp))}{dr} \right|, \tag{5.1}$$

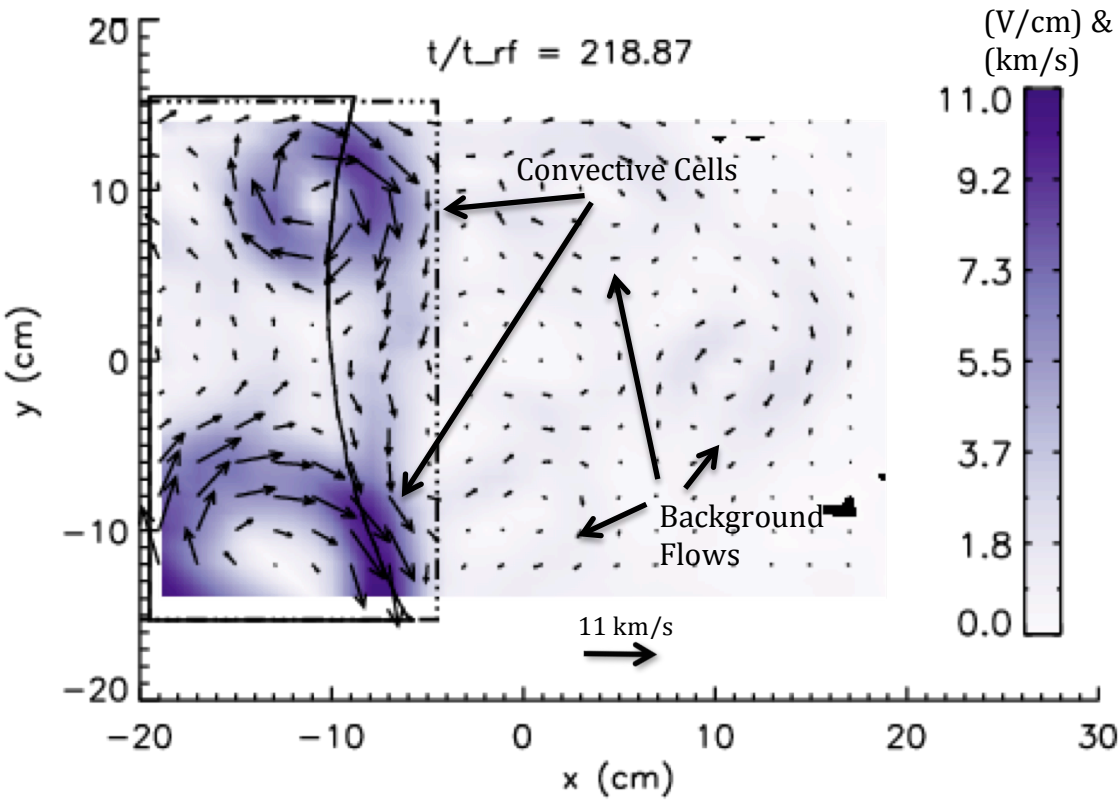

Figure 5.1: A color map of the **E**-field (V/cm) and flow speed (km/s) magnitudes. A vector map of the calculated $\boldsymbol{E}\times\boldsymbol{B_0}$ drift velocity is superimposed. The maximum flow speeds occur at the top and bottom of the antenna box, where the value of $V_{p,DC}$ reached its highest values. The two circular flow regions at the top and bottom of the antenna are commonly known as "convective cells." The two convective cells are linked by flows between them.

where $l_{E_\perp}^{-1}$ is defined as the inverse scale length of the electrostatic electric field, and ρ_{T_i} is the thermal Larmour radius for ions, and $\boldsymbol{E}_\perp$ is inside the argument of the natural logarithm function. In order to use the $\boldsymbol{E}\times\boldsymbol{B_0}$ drift explanation for particle trajectories, it is required that the ratio $\rho_{T_i}\cdot l_{E_\perp}^{-1} \ll 1$. The calculated values satisfy the inequality $\rho_{T_i}\cdot l_{E_\perp}^{-1} < 0.2$, so describing the response in terms of $\boldsymbol{E}\times\boldsymbol{B_0}$ drifts is appropriate. Flow speeds approach 11 km/s, according to figure 5.1, which is the sound speed for cold Helium ions with a 5 eV electron temperature.

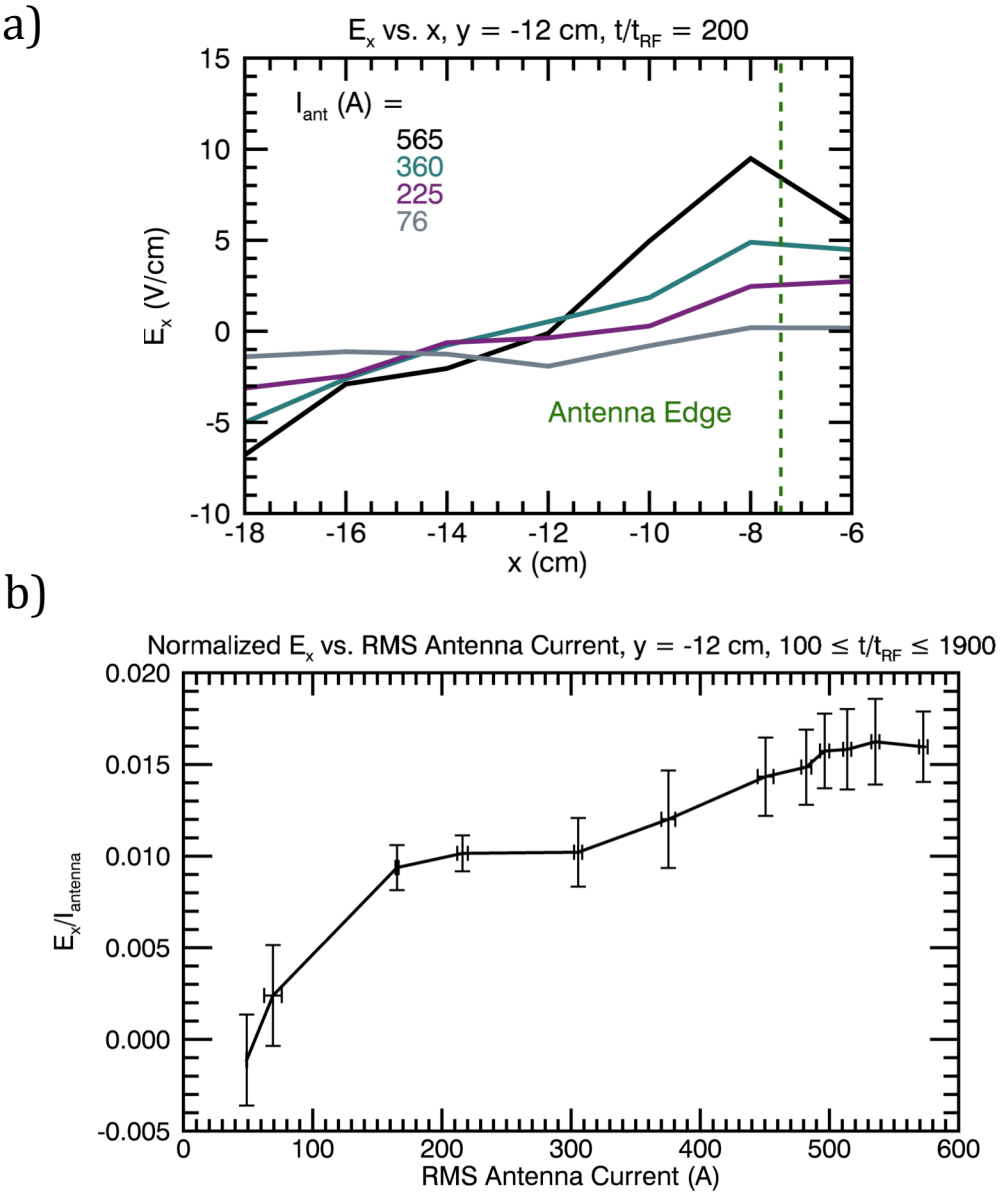

Figure 5.2: a) $\boldsymbol{E_x}$ vs. x profiles for several antenna currents. The maximum value of $\boldsymbol{E_x}$ is reached inside the region between both the antenna and the limiter. The limiter edge is located at x = -4.5 cm, and its boundary is not shown in the figure. b) Normalized $\boldsymbol{E_x}$ vs. RMS antenna current.

The calculated $\boldsymbol{E_x} = -\boldsymbol{\nabla_x} V_{p,DC}$ is plotted in figure 5.2a for several antenna currents. It shows the steepening of the $\boldsymbol{E_x}$ vs. x profile steepens with increasing antenna current. The maximum electric field occurs between the antenna and the limiter, at x = -8 cm. The maximum

value of $\boldsymbol{E_x}$, normalized to the RMS antenna current, is plotted vs. $I_{antenna}$ in figure 5.2b. The figure shows a threshold current for the onset of large $\boldsymbol{E_x}$. For RMS antenna currents less than 100 A, there appears no appreciable $\boldsymbol{E_x}$. Above 150 A RMS in the antenna the electrostatic electric field increases significantly. Between 150 A and 570 A normalized $\boldsymbol{E_x}$ increases gradually with antenna current. Within this range of currents is where the RF enhanced plasma potential, shown in figure 4.12, increased linearly with antenna current; this indicates that the potential oscillations at the antenna are $\sim 3T_e$ or greater. Figure 5.2 b) indicates that though the rectified potentials increase linearly with antenna current, the electric fields increase quadratically above a threshold current.

5.2 Density Convection in the SOL across $\boldsymbol{B_0}$

The SOL density profile experiences a profound adjustment during the application of an RF pulse. As mentioned previously, I_{isat} measurements are used as a proxy for density. Langmuir probe sweeps acquired in a plane at z = 1.63 m and performed after the RF pulse showed no significant heating in the bulk plasma region. Figure 5.3 below shows a time sequence of I_{isat} measurements with $\boldsymbol{E}\times\boldsymbol{B_0}$ vectors superimposed. At time $\frac{t}{t_{RF}} = 218.87$ the density on magnetic field lines connected to the front of the antenna is significantly altered. At the antenna midplane and above, $0\ cm \leq y \leq 10\ cm$, the density is decreased, while below the midplane, $-10\ cm \leq y \leq 0\ cm$, the density is increased. The density profile relaxes to an equilibrium state after $\frac{t}{t_{RF}} \approx 440$, at which point the profile is still altered from its profile before the application of the RF pulse.

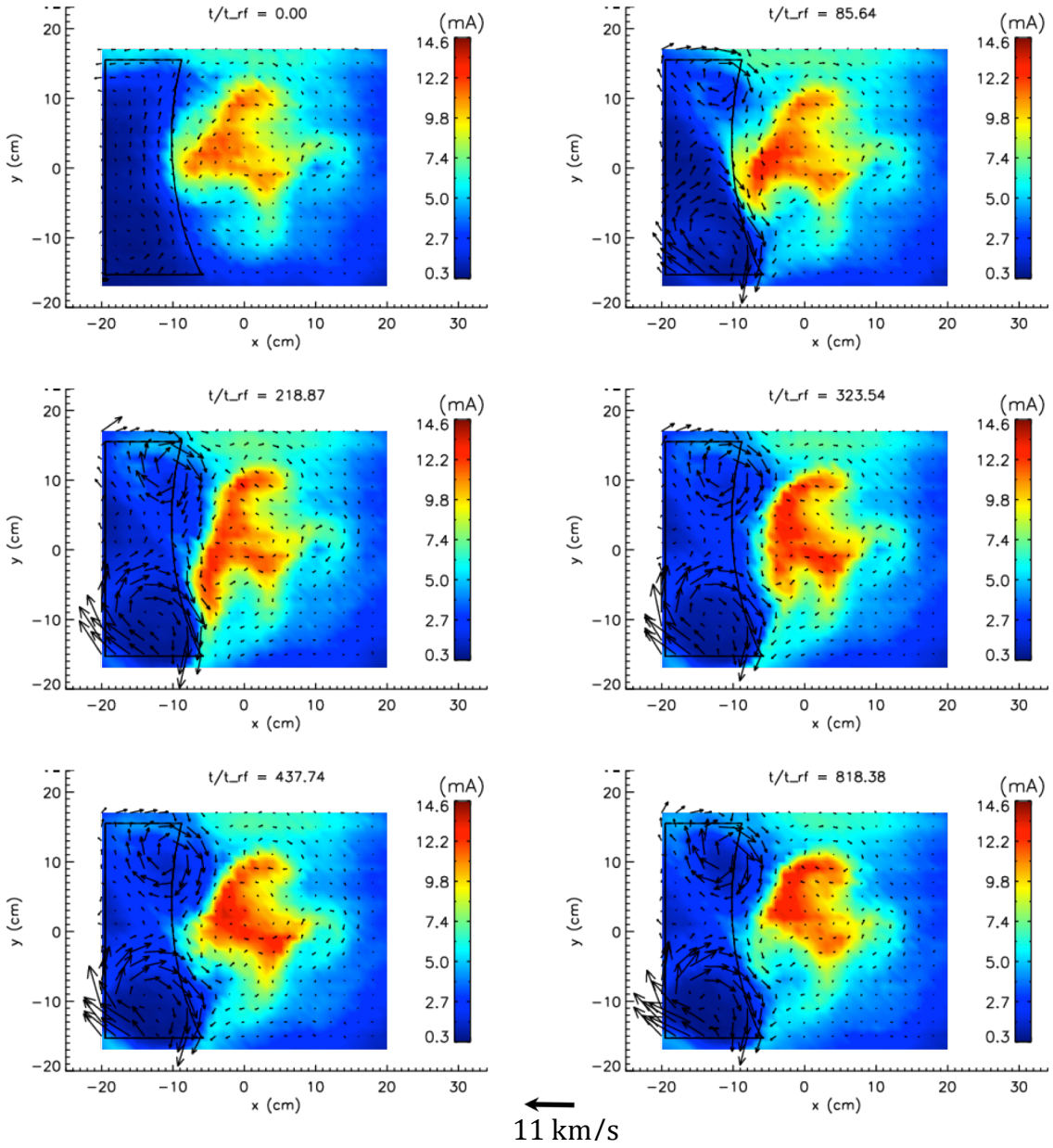

Figure 5.3: A time sequence of I_{isat} measurements at z = 65 cm (color) with calculated $\boldsymbol{E}\times\boldsymbol{B_0}$ vectors superimposed. Time is increasing left to right and top to bottom. The plasma density is significantly altered due to the application of the RF pulse to the antenna. Plasma density on field lines connected to the front of the antenna is pushed downward, in the direction of the $\boldsymbol{E}\times\boldsymbol{B_0}$ flow arrows. Some density is also moved into the private SOL due to the convective cells. The density is most significantly altered at $\frac{t}{t_{RF}} =$ 218.87. After this time, density in front of the antenna is seen to increase until an equilibrium state is attained.

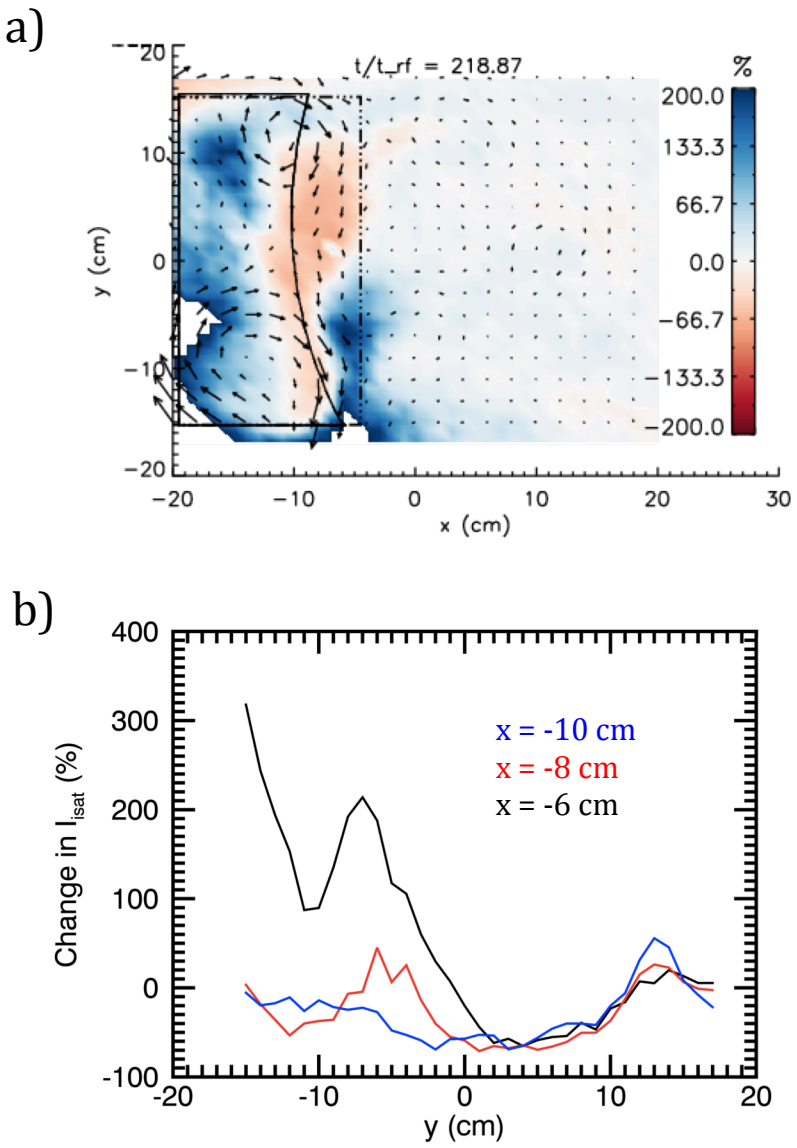

Figure 5.4: a) A color map of the percent change in density, as calculated from I_{isat} measurements with a vector plot of $\boldsymbol{E}\times\boldsymbol{B_0}$ drifts superimposed. Density in front of the current strap is decreased while density in the private SOL and at the bottom of the antenna are increased. b) Line plots through the data plotted in figure 5.4 a). There is a significant increase in the density at the lower end of the antenna.

A vector plot of the $\boldsymbol{E}\times\boldsymbol{B_0}$ flows and a color plot of impact on the density is displayed in figure 5.4 for the time at which the density is most significantly modified. The color map shows $I_{isat} \equiv I_{isat}(t)/I_{isat}(0) * 100.0$, which is the ratio of the value of I_{isat} during the RF pulse to the value of I_{isat} before the RF pulse. The density profile in the region directly in front of the antenna ($-10\ cm \leq x \leq -6\ cm$) experiences a change that differs depending on y-location in the figure. In tokamak parlance the density change is "poloidally asymmetric." At the top of the antenna ($-5\ cm \geq y \geq 10\ cm$), there is a depletion of density. Closer to the bottom-right corner of the antenna in figure 5.4, $-10\ cm \geq y \geq -5\ cm$, the density has increased. Figure 5.4 is consistent with the $\boldsymbol{E}\times\boldsymbol{B_0}$ flow "pushing" density in front of the antenna in the $-\hat{y}$ direction. In addition, the SOL density profile exhibits a significant change during the RF pulse, and some density is swept into the SOL by the convective cells. Density profile modification in front of the antenna affects the antenna coupling, and no current simulations self-consistently calculate the nonlinear interaction between the plasma and the antenna; often a density profile is assumed. Figure 5.4 b) shows line cuts of this data for various values of x. A clear poloidal asymmetry can be seen in this figure.

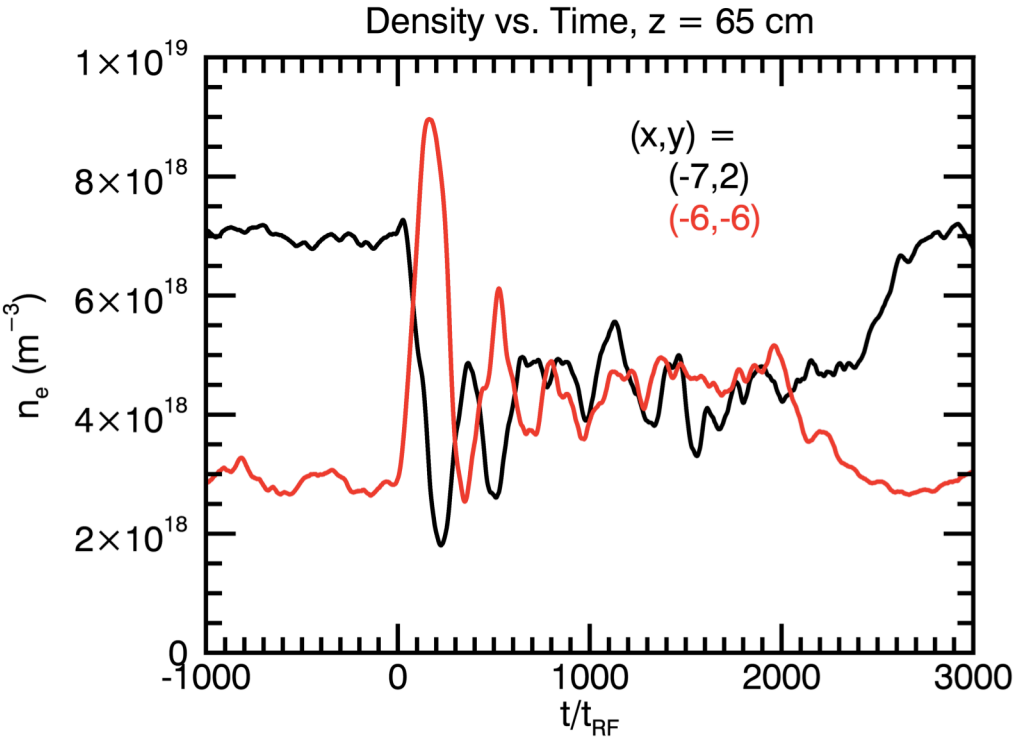

Figure 5.5: A trace of the density vs. time inferred from the measured I_{isat} values. The red/black traces are acquired at (x, y, z) = (-6 cm, -6 cm, 65 cm)/(-7 cm, 2 cm, 65 cm). After 1000 RF cycles, the density has equilibrated and increased/decreased at locations magnetically connected to the bottom/middle of the antenna.

Figure 5.4 shows a single snapshot in time of the density modification in a plane across the plasma column. The density profile, however, does not reach an equilibrium until much later during the RF pulse. Figure 5.5 shows a plot of two locations where the density fluctuates significantly. Within 200 RF cycles, the density significantly increases at (x,y) = (-6 cm, 6 cm) and decreases at (x,y) = (-7 cm, 2 cm). This density modulation is almost 180 degrees out of phase between these two locations. A more quiescent state is reached at $\frac{t}{t_{RF}} = 1000$, where the final density at (-6 cm, 6 cm) is higher than before the RF pulse and the final density at (-7 cm, 2 cm) is lower than before the RF pulse. During the RF pulse, the change in density triggers the onset of low frequency, coherent oscillations in the I_{isat} measurements, as shown in figure 5.5.

The frequency of these oscillations is 7 kHz. This low frequency oscillation in the I_{isat} measurements suggests that drift waves may play a role how the density reaches an equilibrium state after the start of the RF pulse. As can be seen in the figure, this relaxation to quiescence requires only a couple of cycles before an equilibrium is obtained.

The main effect of the RF pulse is to eject density directly in front of the antenna region. A power scaling of the effect on the density is shown in figure 5.6 a). This shows the ratio of I_{isat} measured 100-125 RF cycles after the RF pulse to I_{isat} measured 2250 - 0 RF cycles before the RF pulse at (y,z) = (0, 65 cm). The figure displays a significant increase in the SOL density between $x \leq -14\ cm$ and a decrease in the density near the antenna edge $-14\ cm \leq x \leq -6\ cm$. The change in the density at the antenna edge is independent of RF power above 390 A RMS in the antenna, as shown in figure 5.6 b). This is interesting given that results plotted in figure 5.3 b) where the electric field responsible for $\boldsymbol{E}\times\boldsymbol{B_0}$ convection continues increasing with increasing antenna current. In the bulk LaB_6 plasma discharge region, $-6\ cm \leq x \leq 8\ cm$ the density is unchanged after the RF pulse regardless of RF power.

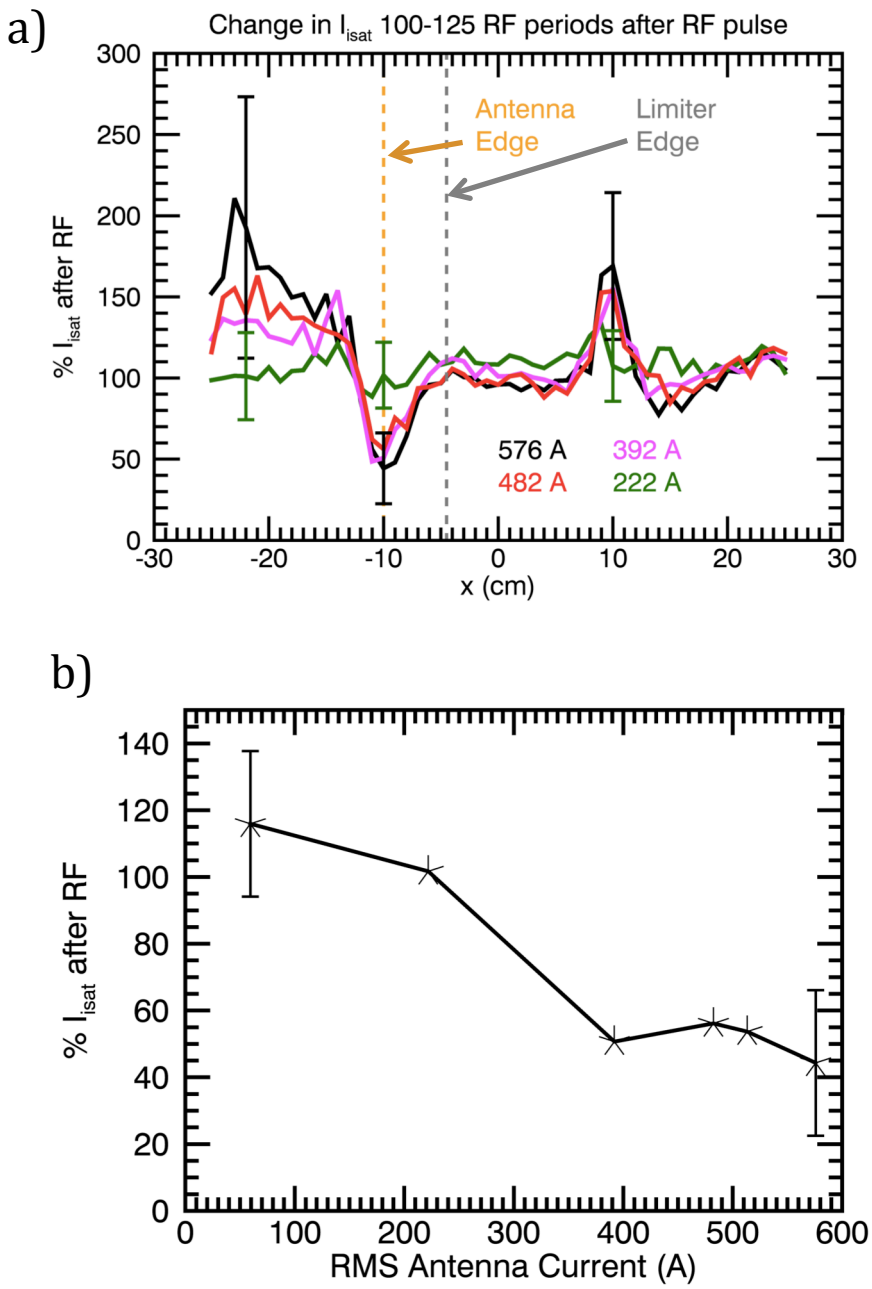

Figure 5.6: a): Percent of density change measured 100 cycles after the RF pulse, (y,z) = (0, 65 cm). The density is significantly depleted at the antenna edge, x = -10 cm. In the far SOL, x < -14 cm, the density is significantly increased. Otherwise, the density remains the same across the column. The RMS antenna current is indicated at the bottom of the figure. b) The same data plotted in figure 5.6 a) but at x = -10 cm only for all antenna currents.

5.3 Consideration of Ponderomotive Effects

In addition to convective cells being a proposed mechanism for causing density redistribution during tokamak ICRH experiments, the ponderomotive force is often implicated in altering the density profile. Particles are thought to experience this force mainly in the region directly in front of the ICRF antenna where evanescent electric fields are highest in magnitude, but the effect on the density is suspected to propagate toroidally and poloidally due to $\boldsymbol{E}\times\boldsymbol{B_0}$ drifts. The ponderomotive force, $\boldsymbol{F}_{pond,no\ B_0}$, is experienced by a charged particle in a spatially inhomogeneous oscillating electric field [e.g. 92],

$$\boldsymbol{F}_{pond,no\ B_0} = -\frac{q_\sigma^2}{4m_\sigma\omega^2}\boldsymbol{\nabla}(\mathbf{E^2}), \tag{5.2}$$

where q_σ and m_σ are the particle's charge and mass, respectively, where σ represents the particle species, ω is the oscillation frequency, and $\boldsymbol{E}$ is the spatially dependent oscillating electric field, whose amplitude is assumed constant in time. This expression is valid only in the absence of an imposed magnetic field, $\boldsymbol{B_0}$, and is therefore not applicable to determining particle drifts when a $\boldsymbol{B_0}$ is present. The ponderomotive acceleration experienced by a charged particle in a magnetized plasma is of considerable interest in the community. Detailed studies of ICRF-relevant ponderomotive effects are given in [93, 94]. A detailed analysis of the ponderomotive effects is beyond the scope of this thesis. However, an attempt at determining the importance of the ponderomotive force in determining the observed effects is made.

In order to estimate the importance of ponderomotive effects, the RF electric field must be determined. The oscillating inductive electric field in front of the antenna was not measured during this experiment. However, the oscillating $\boldsymbol{B}$-field was measured, and it can be used to gain insight into the ponderomotive effects due to the antenna. Figure 5.7 a) shows a color map of the amplitude of $\boldsymbol{B_z}$ measured in the z = 0 plane. The amplitude is highest closer to the

antenna. The black regions in the color map in figure 5.7 a) are where no measurements were made due to concerns about the probe hitting the antenna structure. The exponential nature of the decay in the amplitude of $\boldsymbol{B_z}$ vs. x is shown in figure 5.7 b) with an exponential fit plotted over the data. This plot suggests that at the antenna midplane the exponential decay in $\boldsymbol{B_z}$ vs. x provides a good fit to the data.

Using Faraday's law, the electric field of the antenna can be calculated assuming a predominantly $\boldsymbol{E_y}$ component to the electric field in front of the antenna. This is consistent with TOPICA simulations of ICRF antennas [95] at vertical locations near the center of the antenna strap, near y = 0 in this experiment. Closer to the vertical edges of the antenna this is a poor approximation for the scaling of the electric field. However, it should give a qualitative prediction for the ponderomotive force and the resulting flows due to it. From Faraday's law it can be calculated that, $\boldsymbol{E_y} = \int \frac{\partial \boldsymbol{B_z}}{\partial t} dx$. The expression for $\boldsymbol{E_y}$ becomes $\boldsymbol{E_y} = \frac{1}{k_x}\frac{\partial \boldsymbol{B_z}}{\partial t} = \frac{i\omega}{k_x}\boldsymbol{B_z}$, with $k_x = 0.14\ cm^{-1}$ the exponential decay rate of $\boldsymbol{B_z}$. The maximum value $\boldsymbol{E_y}$ takes for a 20 G $\boldsymbol{B_z}$ at a frequency of 2.4 MHz is then $\boldsymbol{E_y} \approx 2.15\ kV/m$. This calculated value of the induced electric field is almost a factor 2 greater than the strongest DC electric fields measured in the vicinity of the convective cells, where $\boldsymbol{E} \approx 1.10\ kV/m$. For comparison, the maximum measured value of the RF electrostatic electric field was $\boldsymbol{E} \approx 1.0\ kV/m$.

A parameter determining the importance of the non-linear effects due to the ponderomotive force is given by the expression [e.g. 96],

$$\beta_e = \frac{\epsilon_0 E^2}{2 n_e T_e}, \tag{5.3}$$

where $\boldsymbol{E}$ is the magnitude of the RF electric field. Substituting in this expression for LAPD SOL parameters, where $\boldsymbol{E} \approx 3.15\ kV/m$ (approximated from the addition of the electrostatic and

inductive components of the oscillating electric field), $n_e \approx 10^{11} cm^{-3}$, and $T_e \approx 1\ eV$, one obtains, $\beta_e \approx 2.7 \cdot 10^{-3}$. This value of β_e would indicate that nonlinear effects due to the ponderomotive force are small. However, this value of β_e relied upon calculated electric fields, rather than measured fields. Furthermore, the 3-D electric field pattern around the antenna is unknown, with the largest electric fields often seen at the top and bottom of the antenna [87]; thus this calculation of β_e may *underestimate* the value of β_e in the SOL. In order to rigorously determine the role of the ponderomotive force in causing the density depletion, all terms in the ion and electron equations of motion would have to be measured. One could then iteratively calculate the density profile by solving the continuity equation with all measured drifts. Such comprehensive measurements are beyond the scope of this dissertation.

Though the discussion thus far has focused primarily on the perpendicular flows, the RF pulse may also form parallel flows. Evidence for this is seen in Mach probe data taken at z = 1.3 m and is shown in figure 5.8. Unfortunately, 2-D Mach probe flow profiles were not obtained from this data run. However, clear evidence for parallel ion flow is seen in figure 5.8. The Mach probe tip facing the antenna shows enhanced collected current, consistent with an ion flow away from the antenna, whereas the probe tip facing away from the antenna shows less current collected during the RF pulse, indicating an ion flow away from the probe tip. Further data collection with Mach probes must be made in order to determine the 2-D structure of the flows in the SOL. The ion flow shown in figure 5.8 is consistent with parallel flows expected due to the ponderomotive force, assuming $\boldsymbol{\nabla E^2}$ increases towards the antenna. However, a rough calculation of β_e gives values $\beta_e \ll 1$. Attribution of the mechanism driving parallel flows in the SOL is not yet possible without more knowledge of the **E**-field produced by the antenna.

a)

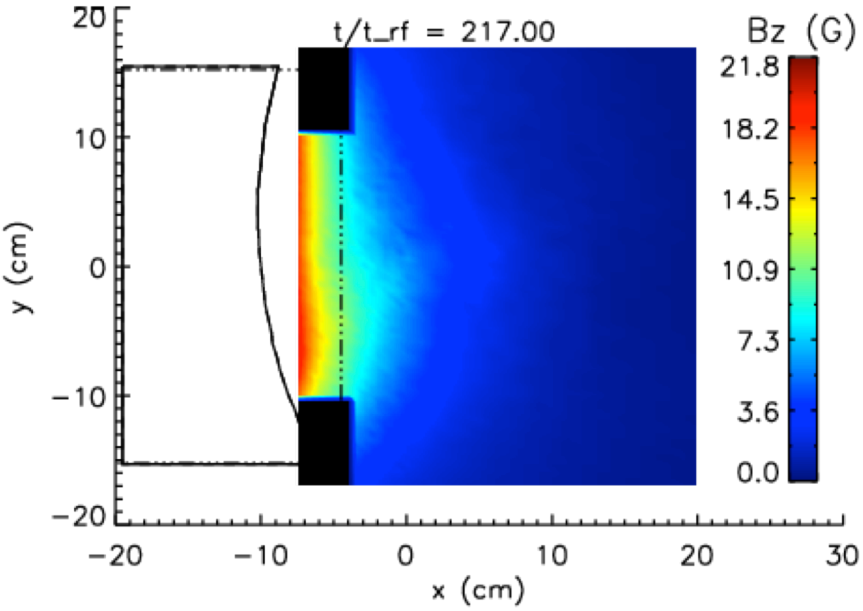

b)

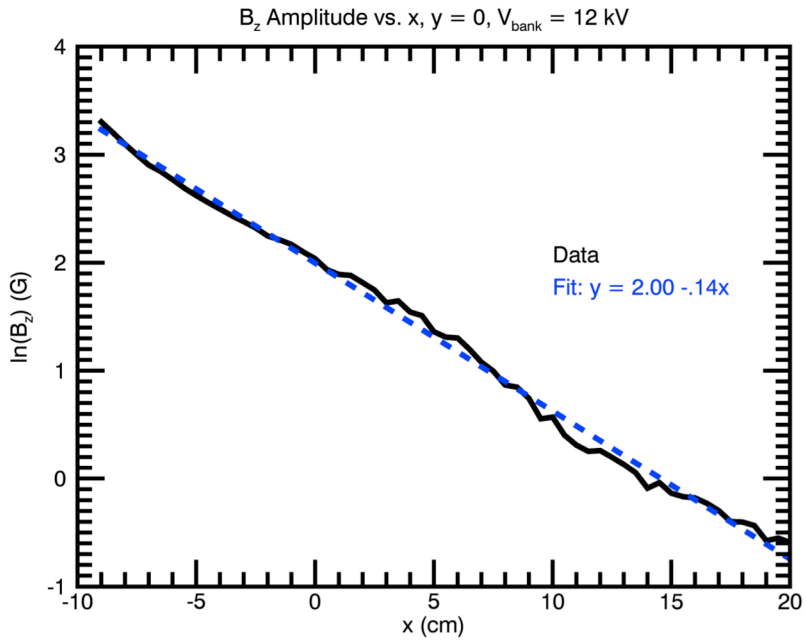

Figure 5.7: a) The measured $\mathbf{B}_z$ profile in the plane of the antenna at at z = 0. The magnitude of $\mathbf{B}_z$ falls sharply with distance away from the antenna. b) A plot showing measured $\ln(\boldsymbol{B_z})$ $vs.\, x$ at (y,z) = (0,0) (black curve). The blue curve shows a linear fit to the data.

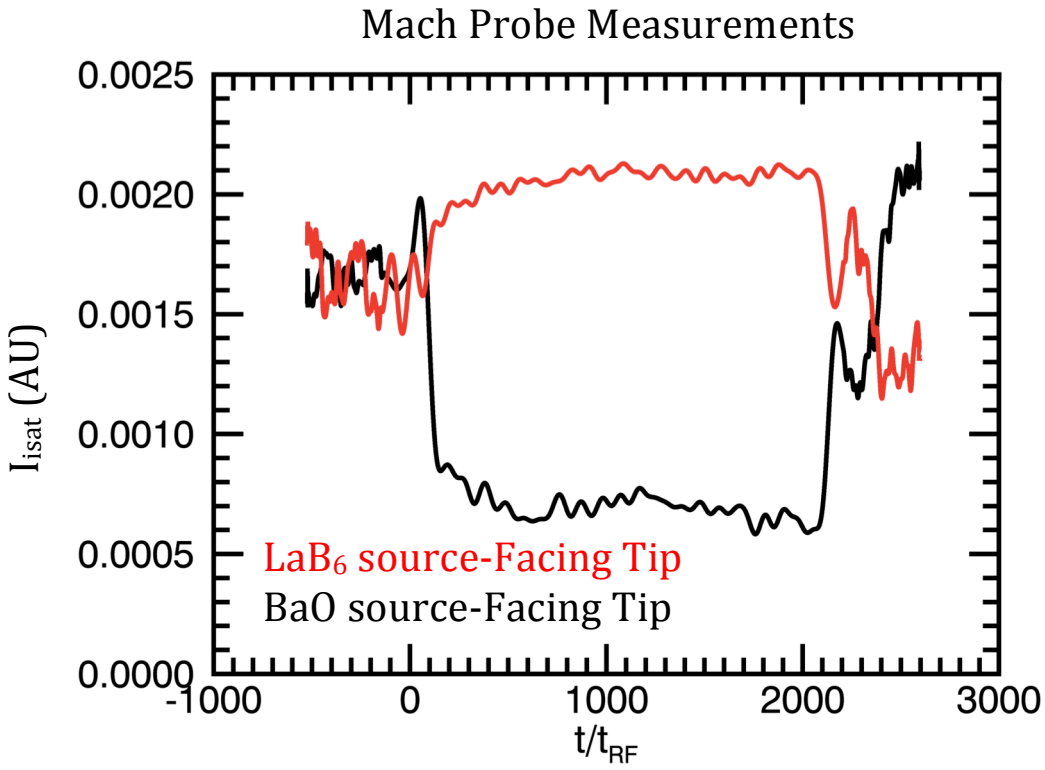

Figure 5.8: I_{isat} measurements from a Mach probe placed at (x, y, z) = (-10 cm, 9 cm, 1.3 m). The figure indicates an ion flow away from the antenna. The probe tip facing the LaB_6 plasma source has a larger value of I_{isat} during the RF pulse than after it, indicating ion flow toward the probe. The probe tip facing the BaO plasma source has a smaller value of I_{isat} during the RF pulse than before it, indicating ion flow away from the probe.

Chapter 6: Conclusions and Future Work

6.1 Conclusions

This dissertation describes detailed measurements of the electrostatic potentials and flows present in the private SOL of an active ICRF antenna. These measurements were made using Mach and emissive probes in a simple, cylindrical geometry. In addition, B-dot probes measured the fast wave pattern launched by the antenna.

Previous work exploring RF sheath formation relevant to ICRF experiments has been performed in research tokamaks utilizing probe diagnostics, reflectometry, and IR thermography. Except for thermography, data obtained in this type of environment has often been 1-D, showing only the radial change in parameters, or has relied on probe diagnostics whose results require a strong dependence on models for interpretation.

The RF system developed for this dissertation was built to operate in the ICRF regime for the LAPD plasma (2 MHz – 6 MHz), with a fixed frequency load of 2.38 MHz. The system is capable of operating with an RF pulse length of 1 ms at the LAPD plasma discharge rate of 1 Hz with up to 150 kW RF power output. The antenna driven by the RF system consists of a single radiating current strap enclosed inside a slotted box with dielectric plates epoxied to the interior of the box sides. This antenna was determined to be the most efficient antenna out of several tried for launching fast waves in the LAPD.

During the RF pulse, the DC plasma potential in the private SOL between the antenna and a limiter was seen to increase, especially at the x-y locations of the top and bottom of the antenna enclosure. This observed plasma potential increase was not observed outside the private SOL. Copper deposits observed on probes removed from the LAPD after the ICRF experiments confirm the large increase in the plasma potential, as the deposits must have come from sputtered

antenna material. These deposits indicate the importance of PMI to ICRF studies, as any antenna design that produces large rectified potentials will cause plasma ion acceleration into antenna components. Based on the ion energy gain through the sheath and the antenna material sputtering yield at that energy, antenna materials may be sputtered and make their way into the bulk plasma.

The ICRF experiment was conducted in the low frequency RF sheath regime, $t_{rf}/t_{sh} \gg 1$, due to both the fixed frequency of the RF amplifier and the plasma density in the private SOL. Both the RF amplifier frequency and the plasma density were unable to be varied at the time of these thesis experiments. Oscillating plasma potential amplitudes were measured to be much less than the DC rectified potentials, indicating that plasma potential oscillations occurred only axially very close to the antenna. Using the antenna current as a proxy for the RF plasma potential oscillations, the DC rectified potential magnetically connected to the bottom of the antenna was observed to scale consistently in power with low frequency RF sheath models. The plasma potential decay after the RF pulse was shut-off lasted much longer than the antenna current decay. It was discovered that this coincided in time with large increases in the density after the RF pulse.

The RF enhanced DC plasma potential creates $\boldsymbol{E}\times\boldsymbol{B_0}$ convective cell flow patterns at the top and bottom of the antenna location in the private SOL. These convective cells are thought to be responsible for the density increase in the SOL. The density in the SOL along $\boldsymbol{B_0}$ lines connected to the antenna edge experienced a poloidal asymmetry, with an increase in density seen at the bottom of the antenna and a decrease at the top. The depletion in the density at the antenna midplane exhibited a saturation above a threshold RF power.

In summary, a 150 kW RF amplifier was developed in order to perform experiments exploring fast wave and RF potential rectification physics. The main findings of this thesis are:

- Plasma potentials rectify up to 96 V, $\approx 20 \cdot T_e$, in the SOL between the antenna and limiter. This potential is of order 3% of the RMS voltage across the antenna coax.
- Convective cells are seen to form in the SOL on magnetic field lines connected to the top and bottom of the antenna. These convective cells are thought to be responsible for modifications to the density in the SOL and at the antenna edge.
- Density modifications occur due to the RF pulse and are consistent with convective cell flow patterns. At the antenna edge, $\frac{\delta n}{n} \approx 0.5$ is observed.

All of these findings present problems for current and future ICRH efforts. Plasma potential rectification increases the likelihood that PMI will become an important consideration in the design and operation of ICRH antennas. Antenna materials are likely to make their way into the plasma. The observed poloidally asymmetric density modification indicates that 1-D antenna wave coupling codes are unrealistic physical descriptions of ICRH experiments. Furthermore, the density modifications due to the active RF antenna highlight the importance of the interplay between fast and slow time scales and the need to integrate both time scales in ICRH simulations.

6.2 Future Work and Outlook

Future Work: The hardware developed in the course of this dissertation is an integral component of the LAPD ICRF campaign involving researchers from several institutions and focusing on fast wave physics and nonlinear interactions between the launching structure and the

plasma. An incomplete discussion of both hardware and physics topics to explore in the future is given in the following paragraphs.

Several improvements to the RF amplifier could be made in order to broaden the scope of the physics that can be investigated. The triodes used in this amplifier are capable of CW operation with an RF output power of 200 kW. Components in the load currently limit the RF pulse length to 1 ms. An upgrade of these components would allow for RF pulsing for the entire LAPD discharge. This would enable the study of low frequency phenomenon that occur due high power RF. In building any RF components, a load impedance must be matched to the conjugate of the generator impedance. In this dissertation, this resulted in a fixed-frequency load at 2.38 MHz. The maximum ratings for the triodes are applicable from between DC to 30 MHz. Adjusting the amplifier to have a broadband operation would allow for the exploration of high power wave physics from the shear Alfvén to the lower hybrid regime. These would of course require their own specially designed launching structures.

As far as the physics results of this dissertation go, there is room to both improve the measurements and place them in a broader scientific context. The RF potential rectification was found to scale consistently with 1-D RF sheath theory. Measuring the spatial distribution of the potential in the sheath using probes with dimensions smaller than the size of the RF sheath would allow for comparison of the sheath structure to the Child-Langmuir sheath. In addition, measurements of the IEDs of ions in the sheath *at the antenna*, using either LIF or RFAs could confirm the nature of the RF sheath with the observation of bimodal energy distributions. This experiment was performed with a specific antenna enclosure consisting of a slotted box with a dielectric material epoxied on the sides. The antenna enclosure type may significantly alter the RF potential rectification. Thus experimenting with several enclosure (dielectric side walls, all

copper box, Faraday shield) types could shed light on the mechanisms rectifying the plasma potential. Furthermore, the results obtained in this thesis could be used to benchmark ICRF simulations purporting to calculate the spatial variations of the RF enhanced plasma potentials and to self consistently calculate the plasma flows and parameters. Though this dissertation has mainly considered the plasma dynamics in the private SOL, there is considerable interest in the plasma directly in front of ICRF antennas. Measurements in the vicinity of the antenna would be directly relevant to the study of how an antenna alters its own coupling.

Physics topics heretofore unexplored in the LAPD could also be investigated using the equipment developed in this thesis. Far-field sheath generation remains an outstanding problem in the ICRH community. The LAPD is an excellent facility for detailed studies of far-field sheaths. Additionally, different types of ICRF antennas could also be constructed, with multiple straps or even entire loops and tested in the LAPD. The amplifier was designed to operate in the ICRF regime in the LAPD. If the ions could be heated such that $T_i > T_e$, this would open up a whole new regime in which to perform basic plasma experiments.

Finally, the wave launched by the antenna has been barely touched upon during the body of this dissertation. A deeper understanding of the launched fast wave and comparison to wave propagation theories and simulations would be interesting.

Outlook: The state of experimental ICRF research programs in the US is in decline. Between 2009 and the present, DIII-D lost its funding for its ICRF program, though the facility is still in operation, and Alcator C-Mod fully lost its funding. ICRF physics research has remained alive and well at both Oak Ridge National Laboratory (ORNL) and Princeton Plasma Physics Lab (PPPL). ORNL facilities include Proto-MPEX and MPEX (planned) for exploring RF sheath physics on fast wave antennas, amongst other things, and NSTX at PPPL employs

High Harmonic Fast Wave (HHFW) heating schemes. It is a shame that two facilities that train students have shut down their research programs that are directly relevant to critical components of ITER, leaving US researchers little alternative but to export their expertise and attention to facilities such as EAST and KSTAR. The UCLA experimental platform, however, offers exciting opportunities to perform basic ICRF experiments in a much more diagnosable environment than a tokamak. The need for this kind of basic experimental study is widely recognized in the community and has inspired the creation of dedicated experiments such as Aline [97] and IShTAR [40] in Europe, both of which, at the time of writing this dissertation, operate with low (≤ 1 kW) RF powers. It is hoped that this encourages more communication between the tokamak and basic plasma communities. The ICRF campaign at UCLA is an optimistic and earnest step in this direction.

Appendix A: Fast Wave Measurements

A.1 Cylindrically Bounded Cold Plasma Waves

This section briefly discusses the theory of wave propagation in a cylindrically bounded plasma. Unlike plane wave theory present in most introductory plasma physics texts, the consideration of these waves involves solving for the spatial profile of the waves in realistic experiment geometry. These types of waves were first considered in the MHD regime in the 1960s [98, 99] and were later considered using the two-fluid equations of motion [100] and [101-103]. The following derivation follows that given in Ch. 5 of ref [92].

Start with a plasma with a dielectric tensor of the form given by,

$$\boldsymbol{\epsilon} = \begin{bmatrix} \epsilon_1 & -i\epsilon_2 & 0 \\ i\epsilon_2 & \epsilon_1 & 0 \\ 0 & 0 & \epsilon_3 \end{bmatrix}. \tag{A.1}$$

In the following theory $\boldsymbol{\epsilon}$ is a rank 2 tensor, and ϵ_1, ϵ_2, and ϵ_3 are given by,

$$\epsilon_1 = 1 - \sum_{\sigma} \frac{\omega_{p\sigma}}{\omega^2 - \omega_{c\sigma}^2},$$

$$\epsilon_2 = \sum_{\sigma} \frac{\pm\omega_{c\sigma} \cdot \omega_{p\sigma}^2}{\omega(\omega^2 - \omega_{c\sigma}^2)}, and \tag{A.2}$$

$$\epsilon_3 = 1 - \sum_{\sigma} \frac{\omega_{p\sigma}^2}{\omega^2},$$

where the subscript σ refers to the particle species and the $\pm$ refers to the species charge. The elements of the dielectric tensor are found by linearizing the charged particle equations of motion neglecting thermal and collisional effects, solving for the particle current in the system and combining it with the displacement current. This dielectric also assumes uniform plasma density. Solutions of the form,

$$\boldsymbol{E} = E(r)e^{i(k_z z - \omega t + m\theta)} \tag{A.3}$$

are considered and substituted into both Faraday's law and Ampere's law,

$$\boldsymbol{\nabla}\times\boldsymbol{E} = i\omega\boldsymbol{B} \tag{A.4}$$

$$\boldsymbol{\nabla}\times\boldsymbol{B} = \frac{-i\omega}{c^2}\boldsymbol{\epsilon}\cdot\boldsymbol{E}\ , \tag{A.5}$$

where c is the speed of light in vacuum. These equations are solved in cylindrical coordinates and after a healthy amount of algebra produce the solution,

$$\left(\boldsymbol{\nabla}_{\perp}^{2} + k_{\perp,-}^{2}\right)\left(\boldsymbol{\nabla}_{\perp}^{2} + k_{\perp,+}^{2}\right)\begin{pmatrix}\boldsymbol{E_z}\\ \boldsymbol{B_z}\end{pmatrix} = 0, \tag{A.6}$$

where the $\perp$ in the subscript refers to directions perpendicular to $\boldsymbol{B_0}$, which is in the $\hat{z}$ direction. The expressions for $k_{\perp,-}$ and $k_{\perp,+}$ is given by solutions to the quadratic,

$$\left(H - \frac{F^2}{G}\right)k_{\perp}^{4} + \left(\frac{i\omega H}{G} + \frac{i\omega\epsilon_3}{c^2}\right)k_{\perp}^{2} - \frac{\omega^2\epsilon_3}{c^2 G} = 0, \tag{A.7}$$

with the "+" and "-" subscripts referring to the quadratic solution with an addition or subtraction in the numerator, respectively, corresponding to the slow and fast wave, respectively. In equation A.7, constants F, G, and H are given by (as well as A and b),

$$A = i\left(\frac{k_z^2}{\omega} - \frac{\omega}{c^2}\epsilon_1\right),$$

$$b = \frac{\omega}{c^2}\epsilon_2,$$

$$F = \frac{\frac{k_z b}{\omega}}{A^2 + b^2}, \tag{A.8}$$

$$G = \frac{A}{A^2 + b^2},$$

$$H = \frac{\frac{ib^2}{\omega} + \frac{A\epsilon_1}{c^2}}{A^2 + b^2}.$$

Equation A.6 is simply the Bessel differential equation with solutions,

$$\boldsymbol{B_z}, \boldsymbol{E_z} \propto A_{m,\pm} J_m\left(k_{\perp,\pm} r\right) e^{im\theta}, \tag{A.9}$$

Where $A_{m,\pm}$ is an arbitrary amplitude factor, and $J_m(k_{\perp,\pm} r)$ is the Bessel function of the first kind of order m. Bessel functions of the second kind do not give valid solutions to the plasma considered in this dissertation because their solutions blow up at $r = 0$. The solution to equation A.6 given in equation A.9 is valid only when $k_{\perp,\pm}$ is real. In the event of an imaginary $k_{\perp,\pm}$, solutions to equation A.6 are given by,

$$\boldsymbol{B_z}, \boldsymbol{E_z} \propto A_{m,\pm} I_m\left(\left|k_{\perp,\pm}\right| r\right) e^{im\theta}, \tag{A.10}$$

Where $I_m(|k_{\perp,\pm}|r)$ are the modified Bessel functions of the first kind of order m. Similarly, modified Bessel functions of the second kind have solutions that blow up at $r = 0$ and are not applicable to the LAPD plasma.

The formula for the radial dependence on the z-component of both $\boldsymbol{B_z}$ and $\boldsymbol{E_z}$ is the same as that given for plane waves in a cold magnetized plasma, e.g. [92]. However, there is a subtle difference between the meaning of $k_\perp$ for plane waves and bounded waves. For plane waves, $k_\perp$, is the wave propagation vector defined by, $k_\perp = \frac{2\pi}{\lambda}$, whereas for bounded waves $k_\perp$ is a constant describing the radial mode of the Bessel function. The $\boldsymbol{B_r}$, $\boldsymbol{B_\theta}$, $\boldsymbol{E_r}$, and $\boldsymbol{E_\theta}$ wave components can be calculated from Maxwell's equations and will not be discussed here.

In a bounded plasma, both fast and slow wave solutions exist simultaneously and the total field is the superposition of these two solutions. Boundary conditions must be matched to find the complete wave profiles across the entire plasma region. For a dielectric interface, the requirement on the fields is,

$$\begin{aligned} \hat{\boldsymbol{n}} \cdot (\boldsymbol{D_1} - \boldsymbol{D_2}) &= \sigma \\ \hat{\boldsymbol{n}} \times (\boldsymbol{E_1} - \boldsymbol{E_2}) &= 0 \\ \hat{\boldsymbol{n}} \cdot (\boldsymbol{B_1} - \boldsymbol{B_2}) &= 0 \\ \hat{\boldsymbol{n}} \times (\boldsymbol{H_1} - \boldsymbol{H_2}) &= \boldsymbol{K} \end{aligned} \tag{A.11}$$

where σ, $\boldsymbol{K}$, and $\hat{\boldsymbol{n}}$ are surface charge density, surface current density, and the unit normal vector pointing from region 1 to region 2; subscripts 1 and 2 indicate the dielectric region. At a perfectly conducting metallic boundary, the tangential component of the electric field must go to zero. The preceding analysis has been conducted only for natural modes of the system, whereas often the wave is launched by an antenna located somewhere in the plasma. This adds an external current term to Faraday's law, further complicating the analysis.

A.2 Fast Wave Measurements in the LAPD

This section describes the fast wave **B-**field measurements made in the LAPD using the slotted antenna described in Chapter 2. The purpose of this section is to document the measurements that have been made and compare them to the simple model presented earlier in this appendix. Unless otherwise noted, the experimental setup used in obtaining the measurements was that described in section 3.3. The theory used for comparison to the measurements is a simplification of the experiment. For example, only the peak density in the LaB_6 discharge region was used to calculate the dielectric in equation A.1. Furthermore, matching boundary conditions at the LaB_6-BaO discharge region interface was not performed. Indeed, even an inspection of figure 3.7 reveals that the plasma is non-cylindrical. The comparison between experiment and theory involves only LaB_6 discharge region plasma parameters and is valid only in that region. This

simplified analysis is instructive in illustrating aspects of the measured wave profiles without having to take into account all of the boundaries in the LAPD: the chamber walls, the limiters, and the slotted-box antenna. Therefore, it is expected that there will exist discrepancies between the model and the measurements.

Fast wave **B**-field measurements were made using the B-dot probes described in chapter 3. All signals were integrated and calibrated using the method discussed in the appendix of ref. [60]. Figure A.1 shows all three wave **B**-field components measured at (x,y,z) = (0, 0, 65 cm) during a single RF pulse. Unlike the antenna current trace, the time

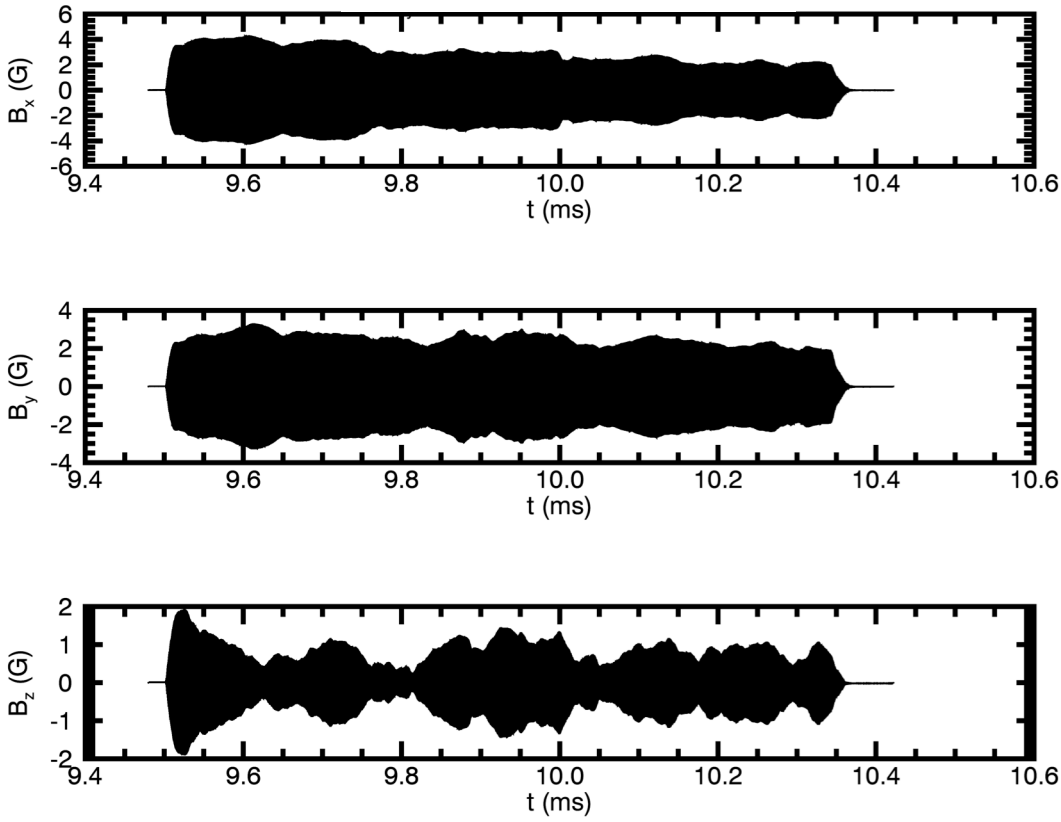

Figure A.1: $\boldsymbol{B_x}$, $\boldsymbol{B_y}$, and $\boldsymbol{B_z}$ wave field measurements vs. time for a single RF pulse with the B-dot probe located at (x,y,z) = (0, 0, 65 cm). The $\boldsymbol{B_z}$ field changes dramatically with time, indicating a change in the wave mode or density profile.

trace of the three components of the magnetic field are not smooth-looking sinusoidal waveforms. This is especially true of the $\boldsymbol{B_z}$ component. This may be due to a combination of either the dominant mode or the r = 0 location of the cylindrically bounded mode changing with time.

If the time window is shrunk to include only a few RF cycles starting at $\frac{t}{t_{RF}} = 116$, the result is figure A.2, showing $\boldsymbol{B_x}$, $\boldsymbol{B_y}$, and $\boldsymbol{B_z}$ at (x,y,z) = (0, 0, 65 cm) . The solid curves in figure A.2 are the measured **B**-field components, and the dashed lines are the results of the model presented in the previous section. The model inputs necessary

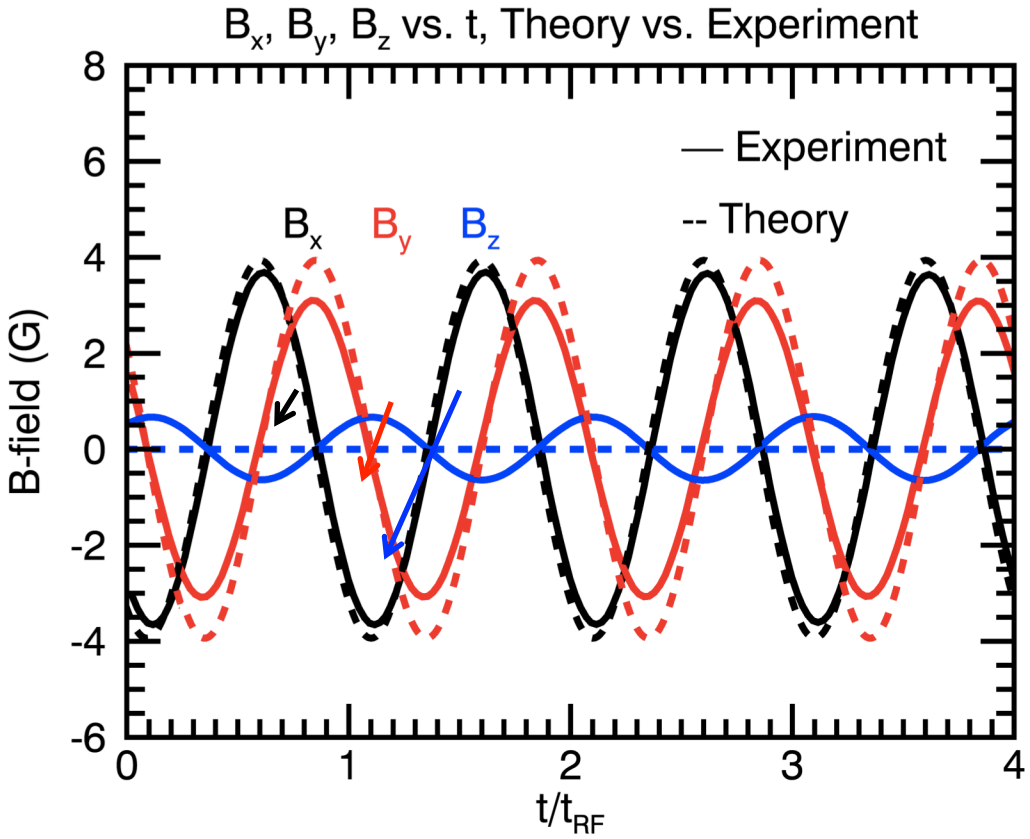

Figure A.2: Four periods of the wave field components (solid curves) compared to theoretically calculated field components (dashed curve). The right-handed polarization of the wave is seen by the $\boldsymbol{B_x}$ trace leading the $\boldsymbol{B_y}$ component by 90°.

to produce the theory curves in figure A.2 were ($\boldsymbol{B_0}$, k_z, n_e, m) = (1000 G, 8 m^{-1}, $7.9 \cdot 10^{18} m^{-3}$, 1), all of which were measured quantities. The theory curves presented are valid only for the fast wave in this model. The calculated magnitude of $k_\perp$ for the slow wave is 859 m^{-1}, so its contribution to the measured fields is thought to be negligible except at the LaB_6-BaO discharge region interface, because of the exponential behavior $I_1(k_\perp r)$ for large argument. Figure A.2 shows the $\boldsymbol{B_x}$ wave component leading the $\boldsymbol{B_y}$ wave component by 90°, showing the fast wave is right-hand circularly polarized. These results agree well with the theoretical wave-propagation model. The measured $\boldsymbol{B_z}$ component at this location is non-zero, as it should be for r = 0. Even a slight deviation in probe location from r = 0 will result in measuring some wave field, thus the disparity between this and the model is expected.

The spatial structure of the wave, $\boldsymbol{B_y}(\boldsymbol{x})$ and $\boldsymbol{B_z}(\boldsymbol{x})$, measured at (y, z) = (0, 65 cm) at $\frac{t}{t_{RF}} = 118$ is shown in figure A.3. The density profile in this experiment is shown in figure 3.7 b). The spacing between positive and negative peaks in the $\boldsymbol{B_z}$ value is what is used to determine $k_\perp$ of the cylindrically bounded mode. Here $k_\perp$ is taken to be π divided by that distance. This does not strictly give the correct argument for the Bessel function form of the wave fields, but it is quite close. $\boldsymbol{B_z}$ profiles involve only a single Bessel function, as indicated in equation A.8, making them a clearer indicator of $k_\perp$ rather than $\boldsymbol{B_x}$ or $\boldsymbol{B_y}$ profiles, which involve the derivatives of Bessel functions, thus involving both higher and lower order Bessel functions. Using this measure of $k_\perp$, the value of $k_\perp$ in figure A.3 is 20.9 m^{-1} for the measured $\boldsymbol{B_z}$ peak separation of 15 cm. This value of $k_\perp$ is used in calculating the model wave profiles, shown as dashed curves, for figure A.3. These curves are calculated for an 18 cm radius LaB_6 plasma discharge

region, though the actual LaB_6 region is roughly within $-8\ cm \leq x \leq 10\ cm$. Outside this region the model cannot be trusted. The comparison between the model and the measurement shows points of qualitative agreement. The $\boldsymbol{B_y}$ wave component for both is highest at x = 0 and decreases with x. The $\boldsymbol{B_z}$ component, on the other hand, resembles a

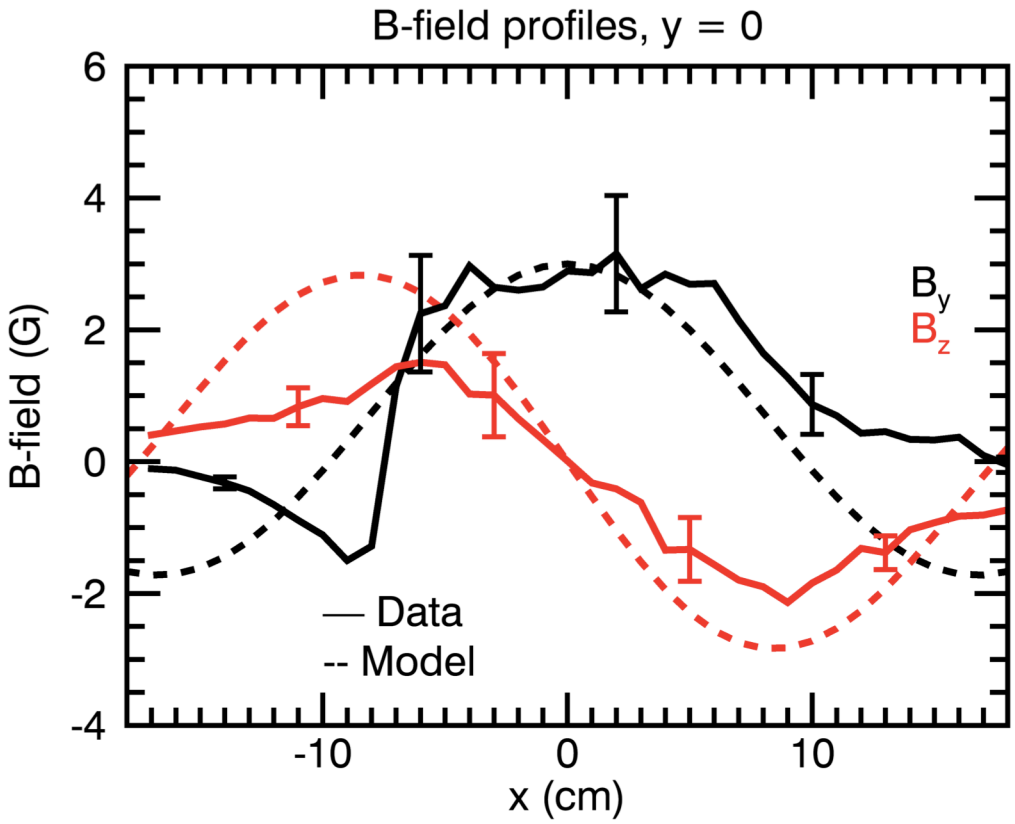

Figure A.3: Wave field profiles at one instant in time, measured/theoretical curves are shown in solid/dashed lines. The LaB_6 plasma radius used in the theoretical curve was 18 cm with the measured $k_\perp$ of 20.9 m^{-1}. For both theory and measurement, $\boldsymbol{B_y}$ is highest at x = 0 cm and falls off from there. For $\boldsymbol{B_z}$, the profile resembles the first order Bessel function.

first order Bessel function centered about x = 0 cm. Quantitatively, the agreement between the model and the measurement is poor. The $\boldsymbol{B_z}$ is too small for how large the $\boldsymbol{B_y}$ component is. Additionally, the $\boldsymbol{B_y}, \boldsymbol{B_z}\ vs.\ x$ profiles are not similar outside $-5\ cm \leq x \leq 5\ cm$. This is partially due to the density profile that was not accounted for in the theory. Figure A.3 shows poorer agreement between theory and measurement than figure A.2 because A.2 compares data and theory at a single location, where the theory is most valid, whereas figure A.3 makes comparisons across the plasma column, including regions where application of the theory is expected to fail.

The fast wave profile was measured in the z = 65 cm plane. This measurement is shown in figure A.4 in the left column for three separate times during a single wave period. The color map represents the $\boldsymbol{B_z}$ field component, and the arrows are vector plots of the $\boldsymbol{B_x}$ and $\boldsymbol{B_y}$ components. The column on the right of figure A.4 shows the same information for the fast wave **B**-field calculated from formulas A.7 and A.9 with the measured $k_\perp$ as an input in the expression and for a LaB_6 discharge region radius of 18 cm. Once again, the agreement between theory and measurements is only qualitative. Both columns of color maps show approximately half the plane is either blue or red (positive or negative $\boldsymbol{B_z}$). The color map of the measurement is similar to the theory-produced color map to its right, resembling the $J_1(k_\perp r)e^{im\theta}$ pattern that is predicted. The arrows concentrated in the middle of the plasma column are pointing either vertically or horizontally, depending on the phase of the fast wave, and they both point in the same direction for the theoretical and measured wave profiles. Additionally, both sets of measurements evolve in time in a similar way, with the entire wave pattern rotating in the counter clockwise direction. Even the simplified theory produces qualitative agreement

with the measurement and quantitative agreement in the center of the LaB_6 discharge. Further studies of the launched wave could involve more refined, non-uniform plasma analytic theories or even 3-D simulations taking into account all of the boundaries present and density nonuniformities utilizing simulations packages such as COMSOL.

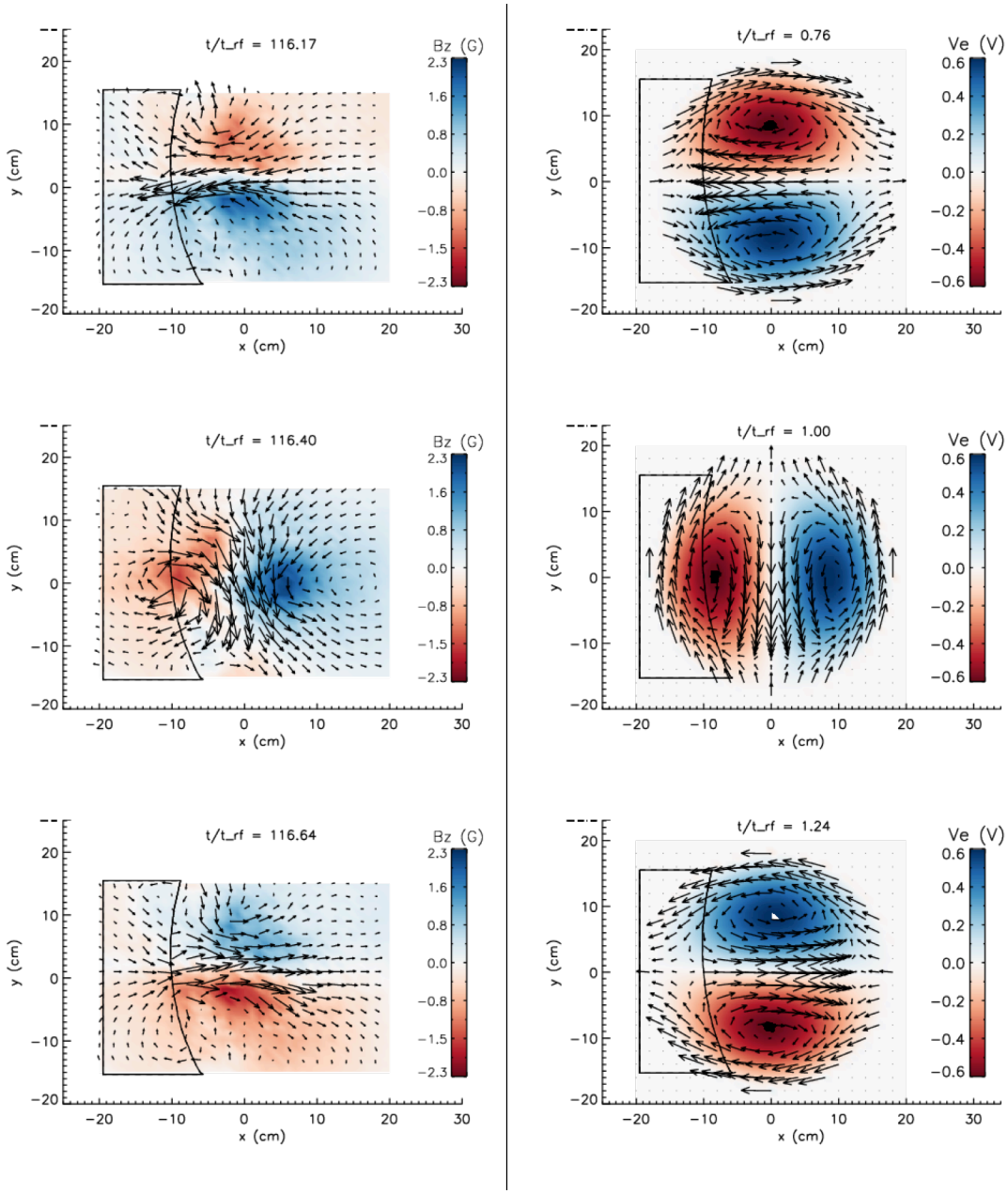

Figure A.4: Left column, measured wave **B**-field components for three separate phases of the RF cycle. Right column, theoretical wave **B**-field components for the same three phases. The color plot shows the $\boldsymbol{B_z}$ wave component, and the vectors show the $\boldsymbol{B_x}$ and $\boldsymbol{B_y}$ components. Time increases going down the column. Arrows at the center of the plane point in the same directions for both theory and measured profiles. Both columns evolve in time in a similar way, with the wave structure rotating counter-clockwise.

Finally, in another experiment, the wave dispersion was measured in the LAPD. The setup was similar to that shown in figure 3.6 but without the limiters and with only a low power (~ 10 kW) RF driver launching the fast wave. Values of $k_{\parallel}$ were measured by calculating the phase difference in $\boldsymbol{B_y}$ signal between two B-dot probes located at (x, y) = (0, 0) with an axial separation of 32.5 cm. Values of $k_{\perp}$ were measured by acquiring **B**-field data on a line at y = 0 and calculating the separation between two peaks in the $\boldsymbol{B_z}$ measurement as previously described. The measurements were performed several times during the LAPD discharge at times when only the BaO source was active and when both the BaO and LaB_6 plasma sources were active. Density measurements with Langmuir probes were also taken in order to compare the dispersion in equation A.6 to the measurements. Figure A.5 shows the wave dispersion curve for the densities measured in this experiment. The points with error bars indicate the actual measured wave dispersion. The measured wave dispersion in all cases but one is an error bar from the dispersion curves given by equation A.5. The measured $k_{\perp}$ values are similar for all measurements taken during the LaB_6 plasma discharge, indicating that the density profile strongly determines the launched mode. Though the agreement between the experiment and the theory is good, there are only five points for comparison. A more convincing set of measurements would involve several plasma density profiles (and thus several $k_{\perp}$ values) and several fast wave launch frequencies, thus fleshing out the sparsely populated parameter space in figure A.5.

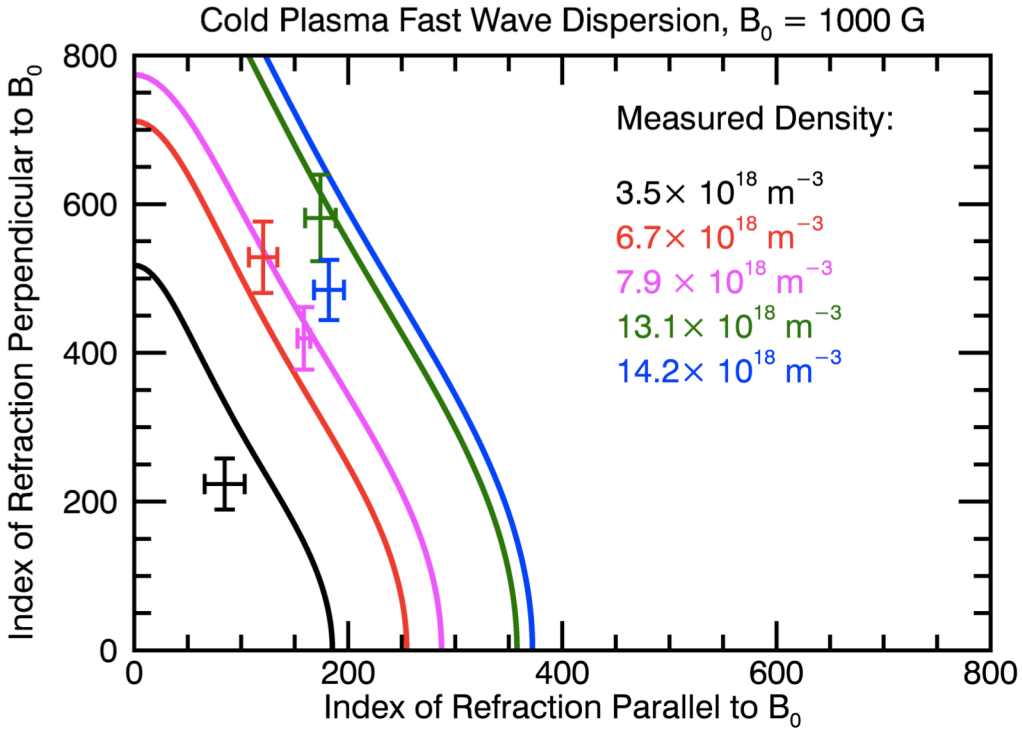

Figure A.5: Wave dispersion curves, theory vs. experiment. The lines are the theoretically calculated dispersion curves using equation A.6. The points are the measured wave propagation parameters.

References

[1] Harms, A.A., Schoepf, K.F., Miley, G.H., Kingdon, D.R., *Principles of Fusion Energy*. Hackensack: World Scientific Publishing Co. Pte. Ltd., 2005. Print.

[2] ITER Physics Expert Group on Energetic Particles, Heating and Current Drive, ITER Physics Basis Editors, and ITER EDA *Nucl. Fusion* **39**, 2495 (1999).

[3] Wilson, J.R. and Bonoli, P.T. *Phys. Plasmas* **22**, 021801 (2015).

[4] Zhang, X.J., Zhao, Y.P., Wan, B.N., Gong, X.Z., Mao, Y.Z., Yuan, S., Xue, D.Y., Wang, L., Qin, C.M., Ju, S.Q., Chen, Y., Qian, J.P., Hu, L., Li, J.G., Song, Y.T., Lin, Y., Wukitch, S., Noterdaeme, J.M., Kumazawa, R., Seki, T., Saito, K., and Kashahara, H., *Nucl. Fusion* **52**, 032002 (2012).

[5] Kim, K.M., Yang, H.L., Hong, S.H., Kim, S.T., Kim, H.T., Kim, K.P., Lee, K.S., Kim, H.K., Bak, J.S., and KSTAR Team *Fusion Engineering and Design* **84**, 1026 (2009).

[6] Bures, M., Jacquinot, J.J., Stamp, M.F., Summers, D.D.R., Start, D.F.H., Wate, T., D'Ippolito, D.A., and Myra, J.R. *Nucl. Fusion* **32**, 1139 (1992)

[7] Wukitch, S.J., Garrett, M.L, Ochoukov, R., Terry, J.L, Hubbard, A., Labombard, B., Lau, C., Lin, Y., Lipschultz, B., Miller, D., Reinke, M.L., Whyte, D., and Alcator C-Mod Team *Phys. of Plasmas* **20**, 056117 (2013).

[8] Jensen, R.V., Post, D.E., Jassby, D.L. *Nuclear Sci Eng.* **65**, 282 (1978).

[9] Perkins, F.W. *Nucl. Fusion* **29**, 583 (1989)

[10] Boschi, A. and Magistrelli, F. *Nuovo Cimento* **29**, 487 (1963).

[11] Perkins, R.J., Hosea, J.C., Jaworski, M.A., Ahn, J.-W., Diallo, A., Bell, R.E., Bertelli, N., Gerhardt, S., Gray, T.K., Kramer, G.J., LeBlanc, B.P., McLean, A., Phillips, C.K., Podesta, M., Roquemore, L., Sabbagh, S., Taylor G., and Wilson J.R., *Phys. of Plasmas* **22**, 042506 (2015).

[12] Myra, J.R., D'Ippolito, D.A., Bures, M., *Phys. of Plasmas* **1**, 2890 (1994).

[13] D'Ippolito, D.A. and Myra, J.R., *Phys. of Plasmas* **13**, 102508 (2006).

[14] D'Ippolito, D.A., Myra, J.R., Jaeger, E.F., Berry, L.A., *Phys. of Plasmas* **15**, 102501 (2008).

[15] D'Ippolito, D.A. and Myra, J.R., *Phys. of Plasmas* **19**, 034504 (2012).

[16] Ochoukov, R., Whyte, D.G., Brunner, D., D'Ippolito, D.A., LaBombard, B., Lipschultz, B., Myra, J.R., Terry, J.L., and Wukitch, S.J., *Plasma Phys. Control. Fusion* **56**, 015004 (2014).

[17] Colas, L., Ekedahl, A., Goniche, M., Gunn, J.P., Nold, B., Corre, Y., Bobkov, V., Dux, R., Braun, F., Noterdaeme, J.-M., Mayoral, M.-L., Kirov, K., Mailloux, J., Heuraux, S., Faudot, E., Ongena, J., and ASDEX Upgrade Team and JET0EFDA contributors, *Plasma Phys. Control. Fusion* **49**, B35 (2007)

[18] Colas, L., et al., *J. Nucl. Mater.* **438**, S330 (2013).

[19] Zhang, W., Feng, Y., Noterdame, J.-M., Bobkov, V., Colas, L., Coster, D., Lunt, T., Bilato, R., Jacquot, J., Ochoukov, R., Van Eester, D., Křivská, A., Jacquet, P., Guimarais, L., and the ASDEX Upgrade Team *Plasma Phys. Control. Fusion* **58**, 095005 (2016).

[20] Colas, L., Bobkov, V., Carralero, D., Kočan, M., Müller, H.W., Manz, P., Kubič, M., Gunn, J.P., Herrmann, A., Rohde, V., and ASDEX-Upgrade Team *AIP Converence Proceedings* **1580**, 259 (2014).

[21] Butler, H.S. and Kino, G.S., *Phys. Fluids* **6**, 1346 (1963).

[22] Lieberman, M.A. and Lichtenberg, A.J., in *Principles of Plasma Discharges and Materials Processing* (John Wiley & Sons, Hoboken, NJ, 2005).

[23] Lieberman, M.A. *IEEE Transactions on Plasma Science* **16**, 638 (1988).

[24] Kawamura, E., Vahedi, V., Lieberman, M.A., Birdsall, C.K. *Plasma Sources Sci. Technol.* **8**, R45 (1999).

[25] Zhang, Y., Kushner, M.J., Moore, N., Pribyl, P., Gekelman, W., *J. Vac. Sci. Technol. A* **31**, 061311 (2013).

[26] Jacobs, B., Gekelman, W., Pribyl, P., Barnes, M., *Phys. Rev. Lett.* **105**, 075001 (2010).

[27] Moore, N.B., Gekelman, W., Pribyl, P., Zhang, Y., Kushner, M., *Phys. Plasmas* **20**, 083506 (2013).

[28] Moore, N.B., Gekelman, W., Pribyl, P., *J. Vac. Sci. Technol. A* **34**, 021303 (2016).

[29] D'Ippolito, D.A., Myra, J.R., Jacquinot, J., Bures, M. *Phys. of Fluids B* **5**, 3603 (1993).

[30] Colas, L., Heuraux, S., Brémond, S., and Bosia, G., *Nucl. Fusion* **45**, 767 (2005).

[31] Colas, L., Gunn, J.P., Nanobashvili, I., Petrzilka, V., Goniche, M., Ekedahl, A., Heuraux, S., Joffrin, E., Saint-Laurent, F., Balorin, C., Lowry, C., Basiuk, V., *J. Nucl. Mater.* **363-365**, 555 (2007).

[32] Bécoulet, M., Colas, L., Pécoul, S., Gunn, J., Ghendrih, P.H., Bécoulet, A., and Heuraux, S., *Phys. of Plasmas* **9**, 2619 (2002).

[33] Bertelli, N., Jaeger, E.F., Hosea, J.C., Phillips, C.K., Berry, L., Gerhardt, S.P., Green, D., LeBlanc, B., Perkins, R.J., Ryan, P.M., Taylor, G., Valeo, E.J., and Wilson, J.R., *Nucl. Fusion* **54,** 083004 (2014).

[34] Milanesio, D. and Maggiora, R., *Plasma Phys. Control. Fusion* **55**, 045010 (2013.

[35] Corre, Y., Firdaouss, M., Colas, L., Argouarch, A., Guilhem, D., Gunn, J., Hamlyn-Harris, C., Jacquot, J., Kubic, M., Litaudon, X., Missirlian, M., Richou, M., Ritz, G., Serret, D., and Vulliez, K., *Nucl. Fusion* **52**, 103010 (2012).

[36] Van Eester, D., Crombé, K., Kyrytsya, V., *Plasma Phys. Control. Fusion* **55**, 055001 (2013).

[37] Van Eester, D., Crombé, K., Kyrytsya, V., *Plasma Phys. Control. Fusion* **55**, 025002 (2013).

[38] Jenkins, T. G., and Smithe, D. N. "High-performance finite-difference time-domain simulations of C-Mod and ITER RF antennas." *RADIO FREQUENCY POWER IN PLASMAS: Proceedings of the 21st Topical Conference*. Vol. 1689. AIP Publishing, 2015.

[39] Smithe, D. N., Jenkins, T. G., and King, J.R. *RADIO FREQUENCY POWER IN PLASMAS: Proceedings of the 21st Topical Conference*. **1689**, 050004 (2015).

[40] Crombé, K., Devaux, S., D'Inca, R., Faudot, E., Faugel, H., Fünfgelder, H., Heuraux, S., Jacquot, J., Louche, F., Moritz, J., Ochoukov, R., Tripsky, M., Van Eester, D., Wauters, T., and Noterdaeme, J.-M., *RFPPC: Proceedings of the 21st Topical Conference* **1689**, 030006 (2015).

[41] Martin, E.H., Zafar, A., Caughman ,J.B.O., Isler, R.C., and Bell, G.L., *Rev. Sci. Instrum.* **87**, 11E402 (2016).

[42] Research Needs for Magnetic Fusion Energy Sciences Final Report (https://www.burningplasma.org/web/ReNeW/ReNeW.report.press1.pdf) pg. 316

[43] *High Power Gain Triodes.* ML-8618/ML-8618V. The Machlett Laboratories, Inc. July, 1973.

[44] McClung, L.B., *Common Sense and Knowledge Approach to Electrical Safety*, IEEE-IAS/PES 2002-2003.

[45] Whitaker, J.C., "Vacuum Tube Principles," in *Power Vacuum Tubes Handbook, 3rd Edition*, (CRC Press, New York, 2012), pp 117 – 131.

[46] Dortwegt, R. and Maughan, E.V., in *Proceedings of the Particle Accelerator Conference*, p. 1456 (2001).

[47] Eastman, A. V., *Fundamentals of Vacuum Tubes, 3rd Edition*, McGraw-Hill Book Company, Inc., 1949.

[48] Wukitch, S.J., Boivin, R.L., Bonoli, P.T., Goetz, J.A., Irby, J., Hutchinson, I., Lin, Y., Parisot, A., Porkolab, M., Marmar, E., Schilling, G., and Wilson, J.R. *Plasma Physics and Controlled Fusion* **46**, 1479 (2004).

[49] Wukitch, S.J., Lipschultz, B., Marmar, E., Lin, Y., Parisot, A., Reinke, M., Rice, J., Terry, J., and the C-Mod Team *J. Nucl. Mater.* **363-365**, 491 (2007).

[50] Kaye, A., Brown, T., Bhatnagar, V., Crawley, P., Jacquinot, J., Lobel, R., Plancoulaine, J., Rhebu, P.-H., Wade, T., Walker, C., *Fusion Engineering and Design* **24**, 1 (1994).

[51] Gekelman, W., Pribyl, P., Lucky, Z., Drandell, M., Leneman, D., Maggs, J., Vincena, S., Van Compernolle, B., Tripathi, S. K. P., Morales, G., Carter, T. A., Wang, Y., and DeHaas, T., *Rev. Sci. Instrum.* **87**, 025105 (2016).

[52] Leneman, D., Gekelman, W., and Maggs, J., *Rev. Sci. Instrum.* **77**, 015108 (2006).

[53] Pribyl, P. and Gekelman, W., *Rev. Sci. Instrum.* **75**, 669 (2004).

[54] Goebel, M., Hirooka, Y., and Sketchley, T. A., Rev. Sci. Instrum. 56, 1717 (1985).

[55] Leneman, D. and Gekelman, W., *Rev. Sci. Instrum.* **72**, 3473 (2001).

[56] Chen, F.F., in *Plasma Diagnostic Techniques*, edited by R. H. Huddlestone and S.L. Leonard (Academic, New York, 1965), Chap. 4 pp. 113-200.

[57] Hershkowitz, N., in *Plasma Diagnostics* (Academic, New York, 1989), Vol. 1, Chap. 3 pp. 113-183

[58] Demidov, V.I., DeJoseph Jr., C.A., and Kudryavtsev, A.A. *Phys. Rev. Letters* **95**, 215002 (2005).

[59] Garscadden, A. and Emeleus, K.G. *Proc. Phys. Soc.* **79**, 535 (1962).

[60] Cooper, C. M. *Transport in a field aligned magnetized plasma/neutral gas boundary: the end of the plasma*. Diss. Univ. of Calif., Los Angeles, 2012.

[61] Everson, E. T., Pribyl, P., Constantin, C. G., Zylstra, A., Schaeffer, D, Kugland, N, and Niemann, C., *Rev. Sci. Instrum.* **80,** 113505 (2009).

[62] Langmuir, I., *J. Franklin Inst.* **196**, 6 (1923).

[63] Kemp, R.F. and Sellen Jr., J.M. *Rev Sci. Instrum.* **37**, 455 (1966).

[64] Sheehan, J.P., Raitses, Y., Hershkowitz, N., Kaganovich, I., and Fisch, N.J., *Phys. Plasmas* **18**, 073501 (2011).

[65] Hobbs, G.D. and Wesson, J.A. *Plasma Phys.* **9**, 85 (1967).

[66] Ye, M.Y. and Takamura, S. *Phys. Plasmas* **7**, 3457 (2000).

[67] Schwager, L.A. *Phys. Fluids B* **5**, 631 (1993).

[68] Sheehan, J.P., Hershkowitz, N., Kaganovich, I.D., Wang, H., Raitses, Y., Barnat, E.V., Weatherford, B.R., Sydorenko, D. *Phys. Rev. Lett.* **111**, 075002 (2013).

[69] Martin, M.J., Bonde, J., Gekelman, W., Pribyl, P., *Rev. Sci. Instrum.* **86**, 053507 (2015).

[70] Stangeby, P.C., *Phys. of Fluids* **27**, 2699 (1984).

[71] Hutchinson, I.H., *Phys. Rev. A* **37**, 4358 (1988).

[72] Hudis, M. and Lidsky, L.M., *J. Appl. Phys.* **41**, 5011 (1970).

[73] Hutchinson, I.H., *Plasma Phys. Control. Fusion* **44**, 1953 (2002).

[74] Oksuz, L. and Hershkowitz, N., *Plasma Sources Sci. Technol.* **13**, 263 (2004).

[75] Oksuz, L., Atta Khedr, M., and Hershkowitz, N., *Phys. Plasmas* **8**, 1729 (2001).

[76] Hutchinson, I.H., *Plasma Phys. Control Fusion* **45**, 1477 (2003).

[77] Ko, E. and Hershkowitz, N., *Plasma Phys. Control. Fusion* **48**, 621 (2006).

[78] Sheridan, T.E., *Phys. of Plasmas* **7**, 3084 (2000).

[79] Rosenberg, D. and Wehner, G.K., *Journal of Applied Physics* **33**, 1842 (1962).

[80] Jacobs, B., Gekelman, W., Pribyl, P., Barnes, M., Kilgore, M., *Appl. Phys. Lett.* **91**, 161505 (2007).

[81] Perkins, R.J., Hosea, J.C., Jaworski, M.A., Bell, R.E., Bertelli, N., Kramer, G.J., Roquemore, L., Taylor, G., and Wilson, J.R., *Nuclear Materials and Energy* (2017).

[82] Abramowitz, M. and Stegun, I.A., *Handbook of Mathematical Functions,* Dover Publications, Inc., 1972, New York (376)

[83] Chodura, R., *Physics of Fluids* **25**, 1628 (1982).

[84] Holland, D.L., Fried, B.D., and Morales, G.J., *Phys. Fluids B,* **5**, 1723 (1993).

[85] Garrett, M.L., Wukitch, S.J., *Fusion Engineering and Design* **87**, 1570 (2012).

[86] Mendes, A., Colas, L., Vulliez, K., Ekedahl, A., Argouarch, A., Milanesio, D., *Nucl. Fusion* **50**, 025021 (2010).

[87] Van Compernolle, B., *Technial Report: Introducing sheath effects into TOPICA* (2009).

[88] Colas, L., Lu, L-F., Krivska, A., Jacquot, J., Hillairet, J., Helou, W., Goniche, M., Heuraux, S., Faudot, E., *Plasma Phys. Control. Fusion* **59**, 025014 (2017).

[89] Bobkov, V. et al, *Plasma Phys. Conrol. Fusion* **59**, 014022 (2017).

[90] Lancellotti, V., Milanesio, D., Maggiora, R., Vecchi, G., Kyrytsya, V., *Nucl. Fusion* **46**, S476 (2006).

[91] Jacobs, B., Gekelman, W., Pribyl, P., Barnes, M., *Phys. of Plasmas* **18**, 053503 (2011).

[92] Swanson, D.G. *Plasma Waves* New York: Academic (1989).

[93] Lamb, B.M., Dimonte, G., and Morales, G.J., *Phys. Fluids* **27**, 1401 (1984).

[94] Drozdenko, T. and Morales, G.J., *Phys. Plasmas* **8**, 3265 (2001).

[95] Van Compernolle, B., Koch, R., Lamalle, P.U., Louche, F., Maggiora, R., Lancellotti, V., Milanesio, D., 34th *EPS Conf. on Plasma Phys.* **31F**, P-4.093 (2007).

[96] Morales, G.J. and Lee, Y.C, *Phys. Rev. Lett.* **33**, 1016 (1974).

[97] Faudot, E., et al, *Rev. Sci. Instrum.* **86**, 063502 (2015).

[98] Woods, L.C., *Plasma Physics* **4**, 165 (1969).

[99] Woods, L.C., *Physics of Fluids* **6**, 729 (1963).

[100] Swanson, D.G., Gould, R.W., Hertel, R.H., *Phys. Fluids* **7**, 269 (1964).

[101] Lehane, J.A. and Paoloni, F.J., *Plasma Physics* **14**, 701 (1972).

[102] Paoloni, F.J., *Plasma Physics* **15**, 475 (1973).

[103] Paoloni, F.J., *Physics of Fluids* **18**, 640 (1975).